CONTROLLED INTRACELLULAR DELIVERY OF MOLECULES USING NANOPARTICLE-MEDIATED PHOTOPORATION

A Dissertation
Presented to
The Academic Faculty

by

Simple Kumar

In Partial Fulfillment
of the Requirements for the Degree
Doctor of Philosophy in the
School of Chemical and Biomolecular Engineering

Georgia Institute of Technology
August 2020

CONTROLLED INTRACELLULAR DELIVERY OF MOLECULES USING NANOPARTICLE-MEDIATED PHOTOPORATION

Approved by:

Dr. Mark R. Prausnitz, Advisor
School of Chemical and Biomolecular Engineering
Georgia Institute of Technology

Dr. Naresh N. Thadhani
School of Materials Science and Engineering
Georgia Institute of Technology

Dr. Julie A. Champion
School of Chemical and Biomolecular Engineering
Georgia Institute of Technology

Dr. Sven H. Behrens
School of Chemical and Biomolecular Engineering
Georgia Institute of Technology

Dr. Stanislav Emelianov
Wallace H. Coulter Department of Biomedical Engineering
Georgia Institute of Technology

Date Approved: April 30, 2020

Dedicated to my parents

ACKNOWLEDGEMENTS

At first, I would like to acknowledge my parents, Rita Devi and Suresh Prasad Saw for the countless sacrifices they made in past and continue to make even now, to secure a future for their children. My father foresaw the value of education in the midst of his livelihood surrounded by poverty and infinite hardships. To my mother, who would sleep less than four hours per day, to make sure that I got all the help I ever needed, related to school or life, I am eternally indebted. I would like to thank my sister Varsha for taking the bigger responsibility of staying home and making sure my parents stay safe and healthy, while I went out in pursuit of my endeavors. I would like to thank my brother Ritik for being the little bundle of joy (although he is not so little anymore).

I would like to thank my research advisor Dr. Mark Prausnitz, first for providing me this privilege to work on such intellectually stimulating project, and secondly for his guidance in experiment design, execution and data interpretation. I thank him for providing his continuous support and feedback, which helped me grow as a researcher and develop my professional attributes. I would like to thank my thesis committee members – Dr. Naresh Thadhani, Dr. Julie Champion, Dr. Stansilav Emelianov and Dr. Sven Behrens for their vital feedback, which has helped me, improve my research quality and add new insights to this work. I am ever so grateful to Dr. Preeti Aghalayam, who first introduced me to the research world and then had continuously guided me through my undergraduate research and transition to graduate school.

I would also like to thank Dr. Stefany Holguin for introducing me to all the lab-life essentials, which kick started my graduate research work and for answering all my curiosity. I am sincerely grateful to you for being patient and supportive, while I slowly learnt and acquired all the experimental techniques. I would like to thank the quad crew Dr. Pradnya Samant, Monica, Josh and Veronica for being the most supportive lab mates. I deeply appreciate the bond we share that goes beyond research conversations (and our love for Priyanka). Pradnya – we share many common strings, although, I will most cherish the support I got during my initial years in grad school, be it the qualifier exam or proposal. Monica – I cannot emphasize enough the value you have added in my development as an individual. In addition, I owe my American pop culture knowledge to our ad hoc discussions. Josh – great minds think alike, but no research will move forward if everyone thought the same way. Thank you for indulging me with all the variety of ideas and discussions. I will for my entire life, treasure the labmates who became true friends. Josh, Rohan and Amir –I would sincerely like to thank you for not letting me do anything stupid – alone. It has been an honor to be a part of Laboratory for Drug Delivery and I would like to thank all the current and previous members (- Dr. Jaya Arya, Dr. Jae Hwan Jung, Dr. Andrew Tadros, Dr. Chandana Kolluru, Dr. Yasmine Gomaa, Dr. Jeong Woo Lee, Dr. Brandon Gerberich, Dr. Song Li, Dr. Jeremy Chae, Dr. Dengning Xia, Dr. Wei Li, Dr. Andrey Romanyuk, Richard Shafer, Richard Terry, Juan, Youngeun, Jonathan and many others) for being an inspiration and helping with numerous problem solving discussions.

I would like to thank Ms. Donna Bondy for her constant support and immeasurable help with every administrative and operational requirements. You have been a pleasure to work with and I sincerely admire your dedication and professionalism. I would like to thank Travis Voorhees and Dr. Greg Kennedy for providing constant support with laser experiments, and extending their generous help with troubleshooting and facilitating my research progress through my several years at Georgia Tech. I would like to thank Eunice Lazau, Carter Kim, Cameroon Chong, Andrew Li and Diana Toro for assisting me with experiments and for always constantly smiling through the adversities we faced (-hopefully no more contaminations). You have been quick learners and have contributed to significantly advance my own research. I wish you all the best for your future endeavors. I would like to thank the core facility managers of Georgia Tech's Cellular Analysis and Cytometry Core**,** who helped me navigate numerous instrument issues, which allowed me to continue my research in a rather smooth manner.

Even though I came to Atlanta for graduate school, my time here has only gotten more colorful and memorable because of the people I have met. For that, I would like to thank the "fabulous five" – Dr. Akshay Korde, Dr. Trisha Sen, Dr. Qandeel Almas and Dr. Gamze Eris (guess who the fifth is?). It is said that our livelihood is molded by the people we surround ourselves with. I have only grown to respect you as my colleagues, and cherish you as my friends, for you give me the inspiration and motivation to enjoy life to the fullest. We all came from such diverse cultures and upbringings, set foot on the same boat, and continued on a journey filled with gratification and delight. Special thanks to Akshay and Trisha for being with me at every step of grad school – the fun part filled with adventurous trips and delicious meals, and the not so fun part – filled with heartbreaks and rejections. I would also like to acknowledge and thank the Indian group of Chemical Engineers for their guidance (including but not limited to Dr. Lalit Darunte, Dr. Rohan Awati, Dr. Shweta Karwa, Dr. Sireesha Alluri, Dr. Mayank Agarwal, Dr. Shilpa Mahamulkar, Dr. Anshuman Sinha, Dr. Souryadeep Bhattacharyya, Dr. Dharam Kumar, Shivesh, Nikhil and Karthick). Finally, I would like to extend my gratitude to the many friends – Kavita, Ushasi, Sai, Aditya, Andres, Dr. Diego Dumani, Jung, Luc, Karthik and, Sayan for being part of this incredible journey.

TABLE OF CONTENTS

LIST OF TABLES

LIST OF FIGURES

LIST OF ABBREVIATIONS

ANOVA	Analysis of variance
ATP	Adenosine triphosphate
BSA	Bovine serum albumin
Ca^{2+}	Calcium ion
CB	Carbon black
CMC	Carboxyl methylcellulose
CNT	Carbon nanotube
CO_2	Carbon dioxide
Cu	Copper
DI	Deionized
DLS	Dynamic light scattering
DNA	Deoxyribonucleic acid
EDTA	Ethylenediaminetetraacetic acid
FBS	Fetal bovine serum
FITC	Fluorescein isothiocyanate
GFP	Green fluorescent protein
H_2O	Water
K^+	Potassium ion
MWCNT	Multi-walled carbon nanotube
NIR	Near infrared
LSPR	Localized surface plasmon resonance
Nd: YAG	Neodymium-doped yttrium aluminium garnet

PBS	Phosphate buffered saline
PDT	Photodynamic therapy
PEG	Poly ethylene glycol
PEOX	Poly(2-ethyl-2-oxazoline)
PFC	Perfluorocarbon
PHPMA	Poly(N-(2-hydroxypropyl)methacrylamide)
PI	Propidium iodide
PVP	Poly vinyl pyrrolidone
RNA	Ribonucleic acid
RPMI	Roswell Park Memorial Institute Medium
SEM	Scanning electron microscope
SiC	Silicon carbide
SiO_2	Silicon dioxide
siRNA	Small interfering ribonucleic acid
SWCNT	Single-walled carbon nanotube
ZnO	Zinc Oxide

SUMMARY

The delivery of exogenous material inside cells has a variety of applications including cellular studies, therapies and diagnostics. A significant resistance to intracellular delivery comes from the plasma membrane, which is made of phospholipidic bilayer that is amphipathic. This bilayer acts as a barrier to counter the passive transport of molecules. There are active transport mechanisms e.g. endocytosis which moves molecules across the cell membrane but these pathways often lead to degradation of original molecule, due to pH change, thereby discounting and/or completely preventing the interaction with target molecule in desired form.

Numerous technologies employing biological, chemical and physical routes have been explored to facilitate this transport. Of these methods, physical route allows for fast, cell type independent and often, less immunogenic intracellular delivery, than biological and chemical routes. However, several physical methods suffer from poor balance between delivery and cell viability loss. Nanoparticle-mediated photoporation allows us to create transient cell membrane pores and deliver exogenous molecules into cellular cytosol, by irradiating cells suspended with Carbon Black (CB) nanoparticles and delivery molecules, with pulsed laser beam. This method leverages thermal and acoustic waves generated by laser-nanoparticle interaction to apply external stress on cell membrane, transiently permeabilizing them for intracellular delivery. To achieve greater control over delivery, we conducted experimental and theoretical studies to understand the role of cellular microenvironment on cellular response, caused by nanoparticle-mediated photoporation.

We investigated the relationship between nanoparticle composition, associated transient energy transduction parameters and bio-effects. Efficiency of nanoparticles to cause photoporation was found to be linked to their energy transduction capacity, specifically; the ability to absorb energy delivered by laser and subsequently dissipate that energy into surrounding fluid in thermal and mechanical form. In addition, we demonstrated that the power law correlation of energy transduction parameters with bio-effects, which would further allow us to predict photoporation efficiency of any given nanoparticles with known physical, thermal and optical properties. Next, we studied the effects of serum addition in cell suspension media on bio-effects and discovered cell viability protection during laser irradiation, caused by macromolecules present in serum. We demonstrated that the biological activity of proteins is not required for viability protection and further showed that certain synthetic polymers perform similar. Finally, we studied the dependence of macromolecular delivery on molecular weight and found diffusion to be the limiting factor. Consequently, we showed improvement of macromolecular delivery by applying low laser fluence for longer exposure duration, thereby; bypassing the limitation set by lower diffusivity of high molecular weight molecules.

Therefore, through this work, we showed dependence of cellular response on nanoparticles, cell suspension media and delivery molecules, which comprise the cellular microenvironment during nanoparticle-mediated photoporation.

CHAPTER 1. INTRODUCTION

With the advancement of biotechnology, numerous new drugs have been engineered to work on intracellular targets, which offer the promise of greater drug efficacy and specificity. Either these drug molecules can be used for therapeutic purposes such as for protein and gene therapy or for diagnostic purposes, such has subcellular interaction studies. For example, diseases like neurodegenerative diseases, chronic conditions and cancer can be potentially treated through siRNA-mediated gene knockdown [1–3]. For these molecules to work, they have to reach their intracellular targets that can be cytosol, nucleus, mitochondria, etc. Most of these molecules work by either downregulating or upregulating the functionality of their target site. However, intracellular delivery of molecules is restricted by cell membrane. This highly selective phospholipid bilayer forms a fluidic barrier between intracellular and extracellular entities, that regulates the flow of smaller molecules such as water, oxygen, Ca^{2+}, etc. but does not allow transport of larger molecules such peptides, proteins and nucleic acids in and out of cells. There exists a natural transport mechanism in eukaryotic cells called endocytosis, which can carry these molecules inside the cell membrane. Majority of the intracellular delivery approaches rely on this natural transport mechanism, but this pathway often leads to molecular degradation due to pH changes and endosomal enzymatic degradation.

Several techniques involving biological and chemical routes have been explored in the literature however; they often come with issues related to low efficacy, cytotoxicity, immunogenicity etc. [4,5]. However, physical methods do not rely on endocytosis, which adds a big advantage but with a trade-off between delivery efficiency and cellular viability.

They work by creating transient membrane pores that are short lived but allow passive diffusion of molecules until they reseal. Therefore, in cases where these pores cannot be appropriately resealed, higher cell viability loss would occur. Physical delivery methods cause cell death by inducing apoptosis, necrosis or cell lysis.

Recently, Chakravarty [6] used the photoacoustic emission/output ability of CB nanoparticles (~200 nm), to deliver small molecule marker compounds (Calcein and FITC-Dextran). When a system comprising of cells, CB nanoparticles and delivery molecules is irradiated with laser beam, the nanoparticles absorb the energy delivered through laser and further dissipate the same by heating up the surrounding fluid, creating vapor bubbles. The sudden volume change due to this process produces acoustic output and fluid mechanical forces, which then interact with the nearby cell membrane exerting external stresses. This is believed to lead to the formation of transient membrane pores that allow the delivery molecules to diffuse through, to access the cytosol. This whole process of creating membrane pores using laser-activated nanoparticle is termed as nanoparticle-mediated photoporation. Certain components of the mechanism are still unclear, for example, whether the pores are created by the interaction between cell membrane and acoustic waves, fluid mechanical forces or thermal output generated by the nanoparticles. Sengupta [7,8] and Holguin [9,10] further elucidated the underlying mechanism and studied the effects of changing experimental parameters on cellular response. Majority of their work was focused on delivering small molecules compounds such as calcein (0.6 kDa) or siRNA (13 kDa) [11].

Previous work had optimized this platform technology to deliver low-molecular weight marker compounds (calcein, 0.6 kDa), which resulted in >90% of cells exhibiting intracellular uptake without significant cell viability loss *in vitro* [12]. Further, Sengupta delivered siRNA (13 kDa) to 54% of ovarian cancer cells, which resulted in knockdown of targeted EGFR mRNA in ~90% of those cells, verifying the efficacy of this technology [11]. Holguin investigated the effects of manipulating cell membrane and cytoskeleton [10], and performed studies exploring cellular responses in a wide parametric space [9,13]. However, there is a lack of knowledge in understanding the role of cellular microenvironment (nanoparticles, cell suspension media and the delivery molecules) on nanoparticle-mediated photoporation and a need to introduce the ability to deliver larger molecular weight substances inside cells. Therefore, the overarching goal of this thesis is to determine the relationship between the components of cellular microenvironment and subsequent cellular responses (termed as bio-effects) as well as to optimize this platform technology for intracellular macromolecular delivery with high cell viability.

At first, we examine the effects of changing cellular microenvironment by either altering the initial experimental conditions or adding new components in the system. We sought to develop a correlation between initial physical parameters (such as nanoparticle composition), energy parameters (such as total energy delivered to the system, energy per particle and energy per mass), transient photoporation parameters and final bio-effects (such as percentage of cells with molecular uptake, nonviable cells and fragmented cells). This should enable us to predict the ability of a nanoparticle to act as an efficient energy transducer and the transient parameters that eventually cause photoporation. As mentioned previously, physical methods suffer from the trade-off between delivery efficiency and cell viability. Thus, we have explored the effects of adding serum in our system, which is known to provide viability protections to cells under external stress application [14]. Serum simulated internal bodily fluids that are ubiquitously present inside human body and thus its effect on nanoparticle-mediated photoporation becomes important.

Finally, we investigated the reasons behind poor delivery efficiency of nanoparticle-mediated photoporation to deliver macromolecules and conducted parametric study showing ways to improve such low performance. To do so, we varied the size of macromolecules ranging from 0.6 kDa to 2000 kDa, and provided operating conditions to deliver this wide size range of macromolecules using nanoparticle-mediated photoporation combined with lower viability loss trade-off.

CHAPTER 2. BACKGROUND

Before 20th century, the average life expectancy of a person was well below 50 years. Majority of the deaths were caused by illness or infectious diseases[15]. With the advancement of science and medicine, the average life expectancy saw an increase, largely due to improvements in public health caused by disease prevention and cure[15]. In addition to drug discovery, design and development, which contributed towards the life expectancy increment, drug delivery very recently has started to gain attention, in part to increase drug efficiency as well as to reach targets within human body that were not explored or not well understood.

Drug delivery has evolved from focusing on macroscopic targets in human body using mainly oral, topical, nasal and intravenous routes in the early 20th century to microscopic targets such as cells in most recent scenarios. This has hugely profited from vast increase in knowledge of drug-target interactions and subsequent responses. With this advancement, intracellular delivery has garnered tremendous attention since, significant number of the drug targets are essentially within cellular or sub-cellular locations. Recent biotechnological research has thus focused on developing drug molecules, which can act intracellularly, such as RNA interference, cell therapy, protein- and gene-therapy. Some of these applications include –

- Imaging and tracking – Tracking biomolecules is crucial for understanding interactions and functions of sub-cellular moieties[16]. For example, cellular and subcellular proteins can now be imaged through fluorescent tags[17] whereas, transfer ribonucleic acids (tRNAs) can be used to track real time protein synthesis inside cells[18]. In addition, intracellular movement of molecules such as siRNAs can be tracked using fluorescently labeled molecules[19] and even help develop sub-cellular biosensors[20].

- Cellular engineering and therapy – It has been shown that there are more than 3000 genomic mutations that can lead to health complications however, those can be mitigated using therapy[4]. Most advanced therapeutic approaches include nucleic acid modification within diseased cells. Some of these therapeutic advances have been made using zinc-finger nucleases (ZFNs), transcription activator-like effector nucleases (TALENs) and clustered regularly interspaced short palindromic repeats (CRISPRs) for cancer treatment, genetic disorders and acquired diseases[21]. Additionally, genomic modifications and enhancements have provided with opportunities to further understand the disease propagation as well develop strategies for therapy. For example, induced pluripotent stem cells (iPSCs) have been produced by expressing a combination of transcription factors to induce a pluripotency state in somatic cells. iPSCs have applications in drug molecule screening as well as gene- and cell-based therapies. These iPSCs can be produced through intracellular delivery of mRNA[22], miRNA[23] and proteins[24].

2.1 Challenges of intracellular delivery

Utilizing traditional delivery methods make drug molecules face several challenges such as acidic stomach environment, first-pass effect of liver and poor absorbance by intestine. Direct intracellular targeting using other delivery methods such as use of viral vectors; liposomes have thus gained traction. However, arguably the biggest challenge for intracellular delivery is the presence of the cell membrane, majorly comprised of phospholipidic bilayer that controls the transport of substances in and out of cells.

Cellular membrane is an exclusive feature found in eukaryotic cells that enclose the cell volume and regulate the transport of materials in and out of cells. The widely accepted fluid-mosaic model[25] (introduced in 1972) proposes that the membrane consists of phospholipids, cholesterol, carbohydrates and proteins (Figure 2.1). The amphipathic phospholipids, arranged in bilayer, encircle the cell volume with the hydrophobic non-polar chain of the lipids embedded together in the inside and the hydrophilic polar head at the interior and exterior surfaces. This arrangement is thermodynamically favorable because it minimizes interaction between the non-polar chains and the surrounding fluid. In between, lie integral membrane proteins that have a hydrophobic region anchored to the hydrophobic core of the lipid bilayer. The other portion of these proteins are exposed to the intra and/or extracellular region. These proteins regulate the flow of ions and small molecules. There are peripheral proteins that do not have any part attached to the hydrophobic core of lipid bilayer but are rather attached to external surface of either integral proteins or phospholipids. Cholesterol is also present among the phospholipid bilayer and are used to maintain fluidity of the membrane packing[26].

There are embedded proteins (called glycoproteins) and lipids (called glycolipids) with carbohydrate attached, exposed to the extracellular region. These carbohydrates help in cell-to-cell communication as well as attract water to the cell surface. There have been proposed advancement of this model but the basic premise remains the same[26].

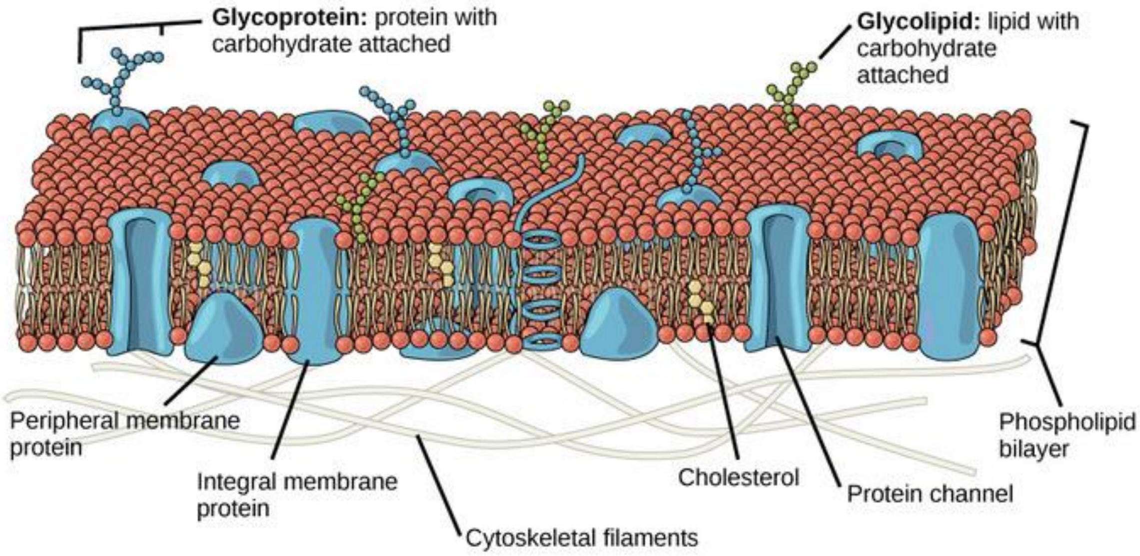

Figure 2.1: Components of cell membrane[27]. Small essential molecules are delivered across cell membrane through active transport channels while natural transport of larger foreign molecules is only possible through endocytosis.

Molecules such as water, carbon dioxide and oxygen are transported through passive diffusion caused by concentration gradient. Polar molecules such as chloride require facilitated diffusion with the help of channel or carrier proteins. The movement still happens in the direction of concentration gradient. Further, certain molecules (such as Na^+ and K^+) move against the concentration gradient through active transport mechanisms that require energy consumption. Transport happens through carrier proteins and the required energy is supplied by the hydrolysis of ATP. A typical example is the active sodium-potassium pump that maintains higher concentration of Na^+ in the extracellular region and higher concentration of K^+ in the intracellular region.

There are two mechanisms by which cells import and export larger molecules and particles, since these are too big to be transported through the above-mentioned mechanisms. While endocytosis helps move substances (sometimes even a whole cell) into a cell, exocytosis moves waste material and other macromolecules out of the cell. Endocytosis is further categorized into two different types – Phagocytosis and Pinocytosis. Phagocytosis is the process through which cells engulf particles such as macromolecules, bacteria or even whole cells. It starts with the formation of pseudopodia (an extension of plasma membrane) around the particle, which eventually surrounds it and then fuse together to form phagosome. Next, the phagosome merges with a lysosome that enables breakdown of the enclosed substance. After the useful nutrients are extracted, the debris is released extracellularly through endosomal escape. Pinocytosis, on the other hand, is the process through which cells engulf molecules as well as surrounding fluid. The subsequent vesicle may not merge with lysosome.

Additionally, there also exists receptor-mediated endocytosis that results from a receptor-ligand interaction. There are receptors present on the exterior surface of plasma membrane that have affinity towards certain specific ligands. These ligands could be present in macromolecules and help them bind to the receptors after which, a vesicle surrounding the macromolecules is formed. These vesicles then fuse with endosomes, which allows the substance to get transported to lysosomes and then released to extracellular region.

2.2 Current intracellular delivery methods -

The efficacy of molecules targeting intracellular moieties is dependent on their delivery efficiency. Crossing cell membrane to reach the target location has always been challenging since this fluidic membrane only allows passage to small molecules. Researchers have investigated different biological, chemical and physical routes to overcome this barrier. While biological and chemical methods still utilize endocytosis, physical methods depend on transient pore formation on the cell membrane surface. Some of these methods are described below.

2.2.1 Biological methods –

2.2.1.1 Viral vectors –

Viral vectors have been the most commonly used biological method for plasmid and gene delivery. Viruses work by attacking and introducing their genetic materials into the host cell. These cells can then reproduce copies of the delivered genetic material. Researchers have used this virus property to deliver materials that can correct the genetic encoding of a diseased cell. Viral vectors can be categorized into two types – integrating viral vectors, that can integrate into host genome and non-integrating viral vectors, that do not into the DNA and thus expression is lost during cell division. The process of introducing therapeutic genetic material into a host cell is called transduction[28]. Several different types of viral vectors such as retroviruses[29], lentiviruses[30], and adenoviruses[31] have been used to infect cells with target DNA and RNA, following which, cells replicate the desired genome through gene expression[32].

Although there are a few FDA approved products in market[33,34], immunogenic responses have placed the greatest hurdles in the accelerated advancement of viral vectors[35]. Unwanted gene mutation and over expression have been causes for concern related to viral vectors’ use as gene delivery vehicles (GDV). They also rely on endocytic pathway to enter cells, which can lower the therapeutic efficacy.

2.2.1.2 Bactofection –

Bacteria strains, such as Listeria monocytogenes[36], certain Salmonella strains[37], Bifidobacterium longum[38], and modified Escherichia coli[39] have also been developed for transgene delivery. These have been delivered inside body either orally[40] or intravenously[41]. Once near the target cells, they utilize the endocytic route to enter the cell and then depend on endosomal escape to reach the cytoplasm. Subsequently they can either utilize the host-cell mediated gene expression or produce and secrete the transgene product themselves[42]. Ease of production of such bacteria makes this route cost efficient and long-term stability of bacterial expression has been shown to be attainable.

However, bacterial toxicity is a cause of concern. Bacterial GDVs also become unsafe and ineffective due to the presence of neutralizing antibodies present inside mammalian bodies[43]. Several studies have investigated bacterial GDVs for cancer gene therapy[44], DNA vaccination[36] and genetic disorders[45]. However, the transgene expression have been generally low compared to other delivery methods[46].

2.2.2 Chemical methods –

Due to the immunogenic responses caused by biological carriers, alternate delivery routes[47] have been investigated recently. These are based on either encapsulating the drug inside polymeric nano-carriers and liposomes or adsorbing/conjugating them on the surfaces of these particles. Due to the anionic nature of cell membrane, cationic polyplexes[48] and lipoplexes[49] have been commonly used which can lead to favorable interaction between the both. Once close/bound to the proteoglycans on cell surface, these nano-carriers get internalized through endocytic route, which does present its own challenges.

However, the degradation of these nanoparticles during the endocytic pathway can work in favor by releasing the desired drug molecules inside cells. It has been shown that the delivery efficiency is also affected by the size of these nano-carriers[50]. The enhanced permeability and retention (EPR) effect of tumors due to leaky vasculature, has also been exploited to design nanoparticles for targeted cancer treatment[51]. Several other properties such as nanoparticle shape[52], stiffness[53], charge[54], surface functionalization[55] can also alter the delivery efficiency and have been investigated in literature[56]. These non-biological GDVs offer lower immunogenicity, can deliver larger payloads and are easier to synthesize[57]. However, poor *in vivo* efficiency and lower long-term expression of target genes have been restricted their use in clinical studies[58].

2.2.3 Physical methods –

2.2.3.1 <u>Electroporation –</u>

Under the application of high voltage electric pulse, the phospholipidic bilayer of cell membrane opens temporarily, allowing the extracellular molecules to travel through and access the cytosol[59]. This method is significantly popular for delivering charged macromolecules and offers advantage in terms of ease of use, fast and high transfection rate, pore size control, smaller drug concentration and bypassing the endocytic pathway completely. Operating conditions including electric field strength, pulse length, number of pulses, time between two pulses, etc. can be optimized to deliver wide size range of molecules[60]. Electroporation has been shown to be useful to deliver drugs, antibodies, oligonucleotides, proteins, RNA, DNA and plasmids *in vivo* for clinical, biotechnological and biomedical applications[60,61]. Permanent cell damage and non-specific transport are major challenges for this method. Researchers are currently working on developing microscale electroporation as an alternative to overcome those challenges. It offers single cell electroporation with more symmetrical and uniform electric field[62].

2.2.3.2 Ultrasound –

Ultrasound has been used commonly for cancer diagnostic purposes in recent years. They make use of the Ultrasound Contrast Agents (UCAs) that are micron sized encapsulated gas bubbles[63]. These UCAs can selectively adhere/relocate near tumor site exploiting the leaky nature of blood vessels surrounding the tumor tissue, after being injected into the blood stream. Under the application of ultrasound waves, the UCAs contract and expand due the changes in applied pressure[64]. This feature can be detected by while imaging the tumor tissue, which will produce a different acoustic output due to the presence of UCAs, hence providing a clear contrast between a normal and a tumor tissue[65]. However, gas bubbles can be designed to collapse or oscillate causing acoustic-cavitation or acoustic-induced bubble activity that subsequently generate acoustic energy with compressive and tensile strength. The acoustic output can transiently disrupt the cell membrane, allowing delivery of nearby drug molecules.

This method is termed as “sonoporation” and has been extensively investigated to deliver wide variety of small molecule, macromolecule and genetic materials diseased cells[66,67]. Ultrasound-mediated poration offers non-invasive, fast and ability to deliver to heterogeneous categories of cell types[68]. However, ultrasound mediated poration also compares lower to electroporation in terms of reporter gene expression[69]. Similar to electroporation, trade-off between cell viability and delivery efficiency is the biggest concern, which has prohibited an extensive use of this method for drug delivery purposes.

2.2.3.3 Microinjection –

Microinjection involves use of glass pipette to manually inject molecules into cytoplasm or nucleus[70]. Though this approach proposes high transfection rate, it has to be done on a cell-by-cell basis by trained professional, which limits its usage in drug delivery applications[71]. Several advancements in terms of using automated[72], micro-capillary and computer-aided systems have enabled to increase the transfection efficiency to upto 1500 cells per hour[73]. However, this approach has been used to successfully deliver DNA[74] and RNA inside living cells and study single cell responses to complicated stimulations as well to show efficacy[72,75].

2.2.3.4 Microfluidics –

Several cell biology studies have been done using microfluidic devices for cell sorting and separation based on size, shape density, deformability, Magnetic susceptibility, polarization, charge density, fluorescent label, etc[76]. A common example would be separation of T lymphocytes (CD4+) from whole blood for diagnosis and treatment of HIV. Researchers have further modified this device to cause transient cell deformation by making the cells flow rapidly through microfluidic constrictions with abrupt, stepwise compression profiles[77]. Subsequently, transient cell deformation takes place, allowing cells to uptake fluid from the surrounding environment[78]. This transient behavior has been utilized to deliver wide size range of macromolecules with cells showing successful expression of EGFP after EGFP mRNA and Plasmid delivery[79,80]. Though this approach gave high delivery efficiency, it is still in early stages of development and limits the drug delivery ability to *in vitro* only

2.2.3.5 Magnetofection -

Magnetofection involves using external magnetic field to concentrate and localize magnetic nanoparticles, such as iron oxide coated with cationic polymers and nucleic acids attached to the surface, near target cells and tissues[81]. Subsequently these nanoparticles get internalized by cells through endocytosis, delivering the payload inside cellular cytosol. Parameters such as contact time, nanoparticle concentration, surface properties as well as magnetic field strength have been varied to increase the delivery efficiency[82,83]. However, the nanoparticle size, blood flow rate and magnetic force field required, place restriction on the potential applications.

2.2.3.6 Gene gun –

Gene gun (or biolistic or particle bombardment method) works by shooting high-velocity nanoparticles, coated with DNA or other genetic materials, into cells or tissues. It was first developed in 1980s for plant gene transformation[84] using gold nanoparticles. It was further used for in vivo transformation in mammalian cells[85]. It promises fast, easy-to-use and flexible method avoiding endocytic pathway for delivering desired molecules in small amount, and has shown good transfection efficiency[86]. Particle size, density, bombardment force, DNA concentration are some of the parameters which govern gene gun transfection efficiency[87]. Pre-clinical and clinical studies on human subjects for DNA vaccination using gene gun revealed potent cell mediated responses. Subsequently numerous DNA vaccination studies are underway for diseases such as influenza, HBV, HIV and Cancer[88,89]. Limited transfection efficiency for larger and deeper area, high humoral immune response[90] as well as cost of operation and pure gold nanoparticles have been major challenges[91], which are needed to be addressed before utilizing gene gun for future applications.

2.2.3.7 Impalefection (nanoneedles, nanofibers and nanowires) –

Nanometer scale structures such as nanotubes, nanofibers and nanowires can be coated with desired molecule and used to puncture the cell membrane by aligning them perpendicularly to the cell surface. This method of intracellular delivery is commonly referred as “Impalefection” and has been explored in literature to deliver genetic materials inside live cells[92]. Small hairpin RNA[93] (shRNA) and DNA[94] molecules have been delivered inside cell nucleus using carbon nanofiber arrays bypassing the extracellular and cytosolic degradation. Due to the complexity of scale (which has also restricted the progress of this method as a therapeutic platform), several fabrication methods have been investigated[95].

2.2.3.8 Nanoparticle-mediated membrane disruption -

Membrane disruption using nanoparticles have often been explored to analyze the associated cytotoxicity of nanoparticles[96]. In particular, carbon nanotubes have been shown to cause cell damage through membrane disruption upon direct contact due to their cylindrical shape and high aspect ratio[97,98]. Recently CNTs were shown to assist in nucleic acid delivery into plant cells by creating transient openings on the cell wall and membrane[99]. Additionally, negatively charged oxidized carbon nanoparticles have also been shown to penetrate mammalian cell membrane and enable direct delivery of nucleic acid and antibody cargo[100,101]. However, all these methods involve direct contact with the cell membrane and thus raise toxicity and clearance issues.

2.2.3.9 Laser-assisted membrane disruption –

Recently, laser beam has been utilized for intracellular drug delivery applications. Generation of transient cell membrane pore to facilitate intracellular delivery of molecules using laser exposure is often termed as photoporation[102]. Pores can be formed either through direct interaction with laser beam[103], called "direct laser-induced photoporation" or through energy dissipated by laser-nanoparticle interaction[104], called "nanoparticle-mediated photoporation". Direct laser-induced photoporation involves a focused laser beam on cell membrane causing pore formation through following three routes[102] a) photothermal route – local temperature increase because of photon absorption by water or membrane molecules b) photomechanical route – pore formation through thermoelastic stress or cavitation bubble formation due to pulsed laser exposure and c) photochemical route – pore formation due to local photodissociation or ROS generation through laser exposure.

Trade-off between delivery efficiency and cell viability is the biggest concern of creating cell membrane pores using external physical forces and thus there still exists a need to develop a platform technology that can help deliver molecules inside cells while preserving cell viability. For this purpose, we are exploring nanoparticle-mediated photoporation as an alternative platform for intracellular delivery of molecules and is described in detail, in the next section.

2.3 Nanoparticle-mediated photoporation –

Nanoparticle-mediated photoporation refers to the use of nanoparticles to create localized pores on cell membrane through laser irradiation. The nanoparticles act as energy transducers by absorbing energy delivered through laser and further dissipating the energy to create membrane pores[105]. This process can be optimized to generate short-lived pores allowing the uptake nearby molecules before the membrane reseals back again. This method bypasses the endocytic pathway and thus offer a viable alternative for efficacious drug delivery.

LASER stands for light amplification by stimulated emission of radiation. A laser beam is created by exciting a gain medium through an electrical or a light source. When the number of atoms in excited state (in the gain medium) becomes greater than number of atoms in ground state, the medium gets activated because of this population inversion, releasing coherent (same wavelength) excited photons. At this point, the rate of emission becomes greater than absorption and thus the light gets amplified. The emitted coherent beam is reflected back and forth between two reflecting mirrors. One of the mirrors however, has a partial transparent cavity in the middle and allows the centerline coherent beam to be transmitted through.

A laser light can differ based on the type of gain medium and energy source used as well as its output characteristics. The laser output can be either continuous or pulsed. The continuous beam has constant output amplitude that requires continuous population inversion. This can be achieved by continuous high input power supply, which can severely limit their usage due to heat generation and associated internal damages to gain media. On the other hand, output of the pulsed laser light varies with time, alternating between ON and OFF periods. It can be used to deposit high energy in a very short time duration. The pulse duration can vary depending on the material used. For example, Ti:Sapphire laser can produce femtosecond pulses while an Nd:YAG laser can produce nanosecond pulses.

The first functioning laser was assembled and operated in Hughes Research Laboratory, California by Theodore H. Maiman on May 16, 1960[106]. Two years later, Leo Goldman used laser beam to remove tattoo in his dermatology profession[106]. In subsequent years, use of laser for surgical purposes grew because of the ability to focus a laser beam at a small spot with precision. Most of the surgical procedures utilized dependent on thermal effects of laser and tissue interaction. Lasers have then been frequently used in (but not limited to) ophthalmology[107], lithotripsy[108,109], gynaecology[110], gastroenterology[111], otolaryngology[112], dentistry[113] and dermatology[114]. Laser has also had applications in photodynamic therapy (PTD) for cancer tumor ablation[115]. Laser wavelength, laser energy, output mode, and laser exposure duration are chosen based on the application.

2.3.1 Laser – nanoparticle interaction –

Nanoparticles, when irradiated with a fixed wavelength laser beam, can act as energy transducers by absorbing the energy delivered through laser beam and dissipating energy into surroundings in the form of heat. The ability to act as an energy transducer is dependent on the nanoparticle’s physical, thermal and optical properties. This laser – nanoparticle interaction feature has been used in various forms to either kill the target cells or deliver molecules inside them by creating cell membrane pores.

2.3.2 Introduction to thermal ablation –

Nanoparticles such as gold can absorb near-infrared laser and act as local heat source for thermal ablation, when placed in contact or near cancer cells. This method of cancer therapy is often termed as “photothermal therapy (PTT)” and has been exploited to ablate tumoral cells[116]. For example, researchers have shown its effectiveness in murine colon carcinoma subcutaneous tumor model, where complete destruction of malignant tumors was achieved[117].

They delivered nanoparticles intravenously and relied on leaky tumor vasculature and EPR effect to deposit the nanoparticles near or within tumor site. PTT has also been used in conjunction with other therapies to increase efficacy[118]. However, not all mammalian cancer cells are equally sensitive to hyperthermia due to the role of heat shock proteins (HSPs)[119]. Due to mutations, some cells can have under-expressed HSPs and thus become more sensitive to heat. However, increased expression of HSPs can provide protection against thermal sensitivity and reduce cell death, which makes PTT unreliable.

2.3.3 Introduction to photoacoustics –

Photoacoustic (also referred to as optoacoustic) effect was first discovered by Alexander Graham Bell in 1880, when he found that acoustic waves were generated through light absorption by selenium[120]. He proposed using this feature in making a photophone, which would use light energy to transmit sound. Biggest application of this phenomenon has been in photoacoustic imaging, which uses laser light as an excitation source, and ultrasound imaging to detect acoustic waves generated from excited targets such as nanoparticles[121]. The mechanism of photoacoustic imaging generation involves light irradiation of suitable particles to deposit heat and subsequent dissipation of heat in liquid media. This results in pressure wave generation, which can propagate through the medium and be detected by ultrasound receiver. Researchers have exploited this feature to offer high spatial resolution while imaging internal organs[122], even at cellular level[123].

Various nanoparticles have been used as energy transducers to generate photoacoustic effect. Gold nanoparticles and its conjugations have been most commonly used for studies related to imaging, therapy and drug delivery, due to their ability to absorb NIR laser beam. Recently CB nanoparticle suspension was shown to generate photoacoustic shock, when irradiated with short laser pulse[124]. Researchers attributed this photoacoustic effect on high temperature chemical reaction between surface carbon and surrounding water.

When irradiated with pulsed laser light, the suspended CB particles absorb the energy delivered and heat up, raising the surface temperature. Subsequently, the energy gets dissipated to the surrounding fluid, causing vapor generation. Earlier, researchers claimed that this vapor reacted with surface carbon to initiate endothermic carbon-steam reaction. The combination of both vapor generation and carbon-steam reaction contributed to rapid volume expansion of gas bubble causing cavitation bubble dynamics and subsequent acoustic wave output[124,125].

2.3.4 Introduction to photoporation –

The generation of pressure (acoustic) waves and associated cavitation dynamics through laser irradiation of CB suspension was seen to be analogous to ultrasound-mediated cavitation where ultrasonic energy is used to implode suspended gas bubbles.

This process releases huge energy in short timeframe, resulting in high velocity fluid flow locally as well as shock wave generation. This feature has been used in ultrasound-mediated drug delivery. Their fundamental similarity with CB mediated photoacoustic effects motivated researchers to explore the possibility of drug delivery using laser activated CB nanoparticles.

Chakravarty et. al. first demonstrated the use of CB to efficiently deliver fluorescent molecules inside multiple cell types[126]. Using Ti:Sapphire femtosecond laser, her work focused on optimizing delivery conditions, which resulted in uptake of smaller calcein molecules by 90% cells while maintaining greater than 90% viability[6]. Chakravarty also delivered BSA and DNA molecules but at a much lower efficiency[6]. She proposed transient permeabilization of cell membrane due to interaction between photoacoustic forces and cell membrane. Her experiments concluded that long-lived end products generated by carbon-steam reaction were not responsible for molecular uptake by cells[126] as opposed to the earlier findings[6]. She also showed that gold nanoparticles were not able to provide efficient molecular delivery at similar experimental conditions[6]. Further studies demonstrated that the delivery efficiency depended on molecular size, CB nanoparticle shape, size and concentration as well as laser energy[127].

CB dispersion is inert and relatively non-toxic to human body[128]. Traditionally, carbon has been used since ancient times, namely India Ink and charcoal for ornamental and official tattoos. Colloidal carbon is well tolerated by human body[129] and has been used extensively for biological experimentation[130]. Carbon particles are deposited in lymph nodes, which further drain into vascular circulation. They usually get cleared from bloodstream by macrophages[131] and platelets. This unique feature of CB in combination with being broad-spectrum absorber of laser light made it an ideal candidate for further research. Therefore, subsequent work by Sengupta focused on using CB nanoparticles and optimizing the experimental parameters around it to maximize molecular delivery and develop an understanding of the process. The femtosecond laser was also replaced by nanosecond laser due to cost benefits and ease of manipulation.

Sengupta looked into the underlying mechanism of CB nanoparticle-mediated photoacoustic wave generation and cell membrane poration and concluded that neither thermal expansion of CB nanoparticles nor carbon-steam chemical reaction play significant role on cellular pore formation[7]. Transfer of momentum and/or heat from the vapor bubbles to the cells were proposed to be the dominant mechanisms of energy transfer that lead to cell membrane poration and intracellular delivery of molecules[7]. They also studied the delivery efficiency of calcein and FITC-Dextran in two different cells lines (DU145 and H9c2)[12] and optimized the laser fluence, CB nanoparticle concentration and number of laser pulses to deliver calcein molecules to more than 90% of cells while maintaining almost 100% cell viability. To mitigate cell viability loss at high laser fluence during photoporation, Sengupta added poloxamers (Pluronic F68 and F127) to cell suspension media that caused enhanced cell membrane resealing after pore formation[132]. This resulted in cell viability increase leading to higher percentage of cells with molecular uptake. Additionally, to demonstrate the efficacy of this methodology, they delivered anti-EGFR siRNA to ovarian cancer cells (Hey A8-F8) and showed 49% knockdown of EGFR expression compared to negative control[11].

To understand the role of cellular mechanics on nanoparticle-mediated photoporation, subsequent studies were performed by Holguin, who altered the cell membrane fluidity (using methyl-b-cyclodextrin and water-soluble cholesterol) and cytoskeleton stability (using latrunculin A and jasplakinolide). Experimental results revealed that destabilization of cytoskeletal actin filaments increased cellular viability and molecular uptake[10]. However, stabilizing actin filaments did not significantly affect molecular delivery efficiency. Changes in cell membrane fluidity also did not significantly affect photoporation and molecular delivery efficiency[10].

Holguin also studied the effect of energy delivered into the system by varying number of laser pulses, laser fluence and CB nanoparticle concentration. One crucial outcome of this study was that the total bio-effects (combination of cells with molecular uptake, non-viable cells and fragmented cells) were found to increase with increase in energy delivered[9]. However, she presented the bio-effects caused by nanoparticle-mediated photoporation in three different zones. At low number of laser pulses, laser fluence and CB nanoparticle concentration (i.e. low energy delivered), bio-effects mainly comprised of viable cells with significant molecular uptake and very low to low viability loss due to cell death and fragmentation. This was the first bio-effects zone. At higher energy delivered conditions, viability loss due to cell death increased and viable cells with molecular uptake decreased. This was second bio-effects zone. At even higher conditions, most of the cells became fragmented and viable cells with molecular uptake became low. This was the third bio-effects zone.

These results were concurrent with previous studies[12,127] and provided a baseline behavior for intracellular delivery using CB nanoparticle-mediated photoporation. Holguin also compared the effects of CB nanoparticles, single-walled carbon nanotubes (SWCNT) and multi-walled carbon nanotube (MWCNT) on photoporation and intracellular delivery of molecules[13]. With increase in laser fluence, CB nanoparticles showed initial rise in molecular uptake that peaks at a certain laser fluence and then decreases. The observed bio-effects is then dominated by non-viable cells and eventually by fragmented cells. However, this trend was not found with SWCNTs and MWCNTs. SWCNTs had very little bio-effects at lower fluences and significant non-viable and fragmented cells at high fluence, but not cells with molecular uptake. MWCNTs showed increasing cellular uptake with increase in laser fluence (though over a broader fluence range compared to CB nanoparticles) which then transitioned into fragmented cells. Very few cells became non-viable over this fluence range contrary to the stepwise change observed in suspensions containing CB nanoparticles.

Thus overall, Chakravarty first demonstrated the use of CB nanoparticles and pulsed laser interaction to cause cell membrane poration and intracellular molecular delivery. Sengupta then further optimized the laser fluence, CB nanoparticle concentration and number of pulses to deliver 0.66 kDa calcein molecules to more than 90% of cells. He also studied the underlying mechanism and proposed that nanoparticles act as energy transducers, absorbing energy from laser beam and dissipating heat to surrounding fluid media, which causes vapor bubble formation leading to thermal, acoustic and fluid mechanical force output. These forces interact with nearby cell membrane and create pores, which can be used as a passage to deliver molecule inside cells. Sengupta demonstrated that poloxamers can be used to increase cell viability during photoporation and showed the efficacy of this intracellular delivery method by delivering anti-EGFR siRNA that caused subsequent gene knockdown in 49% of ovarian cancer cells. Recently, Holguin investigated the relevance of cellular mechanics as well as different carbon material shape on photoporation and molecular delivery. She also studied the correlation between total energy delivered by varying initial operating parameters and concluded that bio-effects increased with increasing energy delivered.

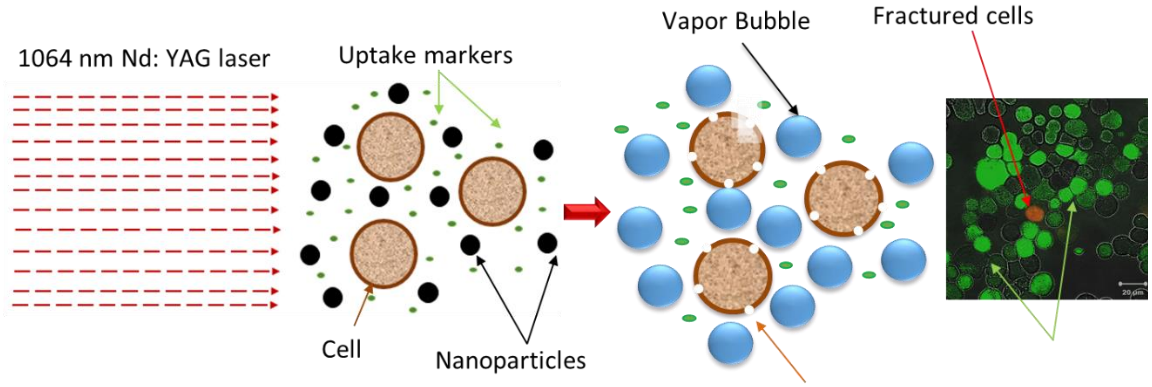

Figure 2.2: A schematic representation of intracellular delivery using nanoparticle-mediated photoporation (not to scale).

However, there still exists a need to explore how the cellular microenvironment affects photoporation and associated bio-effects. Therefore, this thesis is aimed at elucidating the effects of changing nanoparticle composition, cell suspension media and molecular weight of the target delivery molecule.

i) Nanoparticles made of several different materials as well as varying in structure and size were chosen to study the effects of physical, thermal and optical properties. Subsequent studies were done to extend the understanding of transient properties directly associated with cell membrane pore formation.

ii) Cell suspension media was altered by adding varying percentages of serum (since they are known to assist in intracellular drug delivery) and subsequent studies were performed to understand their effects on nanoparticle-mediated photoporation.

iii) Lastly, the effect of changing the size of delivery molecules was analyzed and subsequent studies were done to increase the delivery efficiency of high molecular weight molecules.

CHAPTER 3. RELATIONSHIP BETWEEN BIO-EFFECTS OF NANOPARTICLE-MEDIATED PHOTOPORATION AND ENERGY TRANSDUCTION PARAMETERS

3.1 Introduction

Many targets for therapeutic and diagnostic medical purposes, as well as basic research investigations, are located inside cells. As a consequence, intracellular delivery systems have been widely researched to reach these intracellular targets. Majority of intracellular delivery systems have relied on viral vectors to transfect cells with nucleic acids[133]. Although, there are a few FDA approved products in market[33,34], immunogenic responses and other safety concerns have placed hurdles in the more widespread use of viral vectors[35,133]. Researchers explored alternative methods by using polymers[134], peptides[135], cationic lipids[136] and dendrimers[137] for intracellular delivery, which resulted in an expansion of delivery molecules from nucleic acids to variety of proteins, synthetic nucleases and molecular probes[138]. However, these delivery methods relied on endocytic pathway to cross the cell membrane that often leads to molecular degradation[139].

Thus, different routes of intracellular delivery have garnered attention, which include application of external stress on cell membrane causing direct poration of cell membrane, thus avoiding endocytosis. Electroporation[140] has been the most common method, which destabilizes the cell membrane due to build-up of charge on the cell surface generated by a pulsed electric field to create transient membrane pores. Additionally, researchers have used sonoporation[141], magnetofection[81], microfluidics[17] among other methods to further explore the use of external stress application for intracellular delivery. However, physical delivery methods often encounter trade-off between cell viability and molecular uptake[91,142].

Recently, nanoparticle-mediated photoporation was presented as a novel method to create transient membrane pores, which enabled delivery of molecules to up to ~90% of cells with insignificant viability loss[12]. Using this approach, a suspension of cells is mixed with CB nanoparticles and desired delivery molecules, and then irradiated with nanosecond (or faster) pulsed near infrared (NIR) laser beam of 1064 nm wavelength. The CB nanoparticles absorb laser energy and then dissipate the energy in form of thermal and acoustic outputs as well as fluid flow. This energy concentration and subsequent transduction generates short-lived vapor bubbles around each nanoparticle as long as the temperature is sufficiently high to vaporize surrounding water[6,12]. The resulting energy interactions can create external stress on cell membrane, leading to membrane disruption that allows desired molecules to diffuse through the transient pores. At optimal conditions, the cell survives this process, but sub-optimal conditions can lead to loss of cell viability. Thus, the whole process involves several energy transfer steps from laser to nanoparticle, nanoparticle to surrounding media and then from media to cell membrane, as shown in Figure 3.1

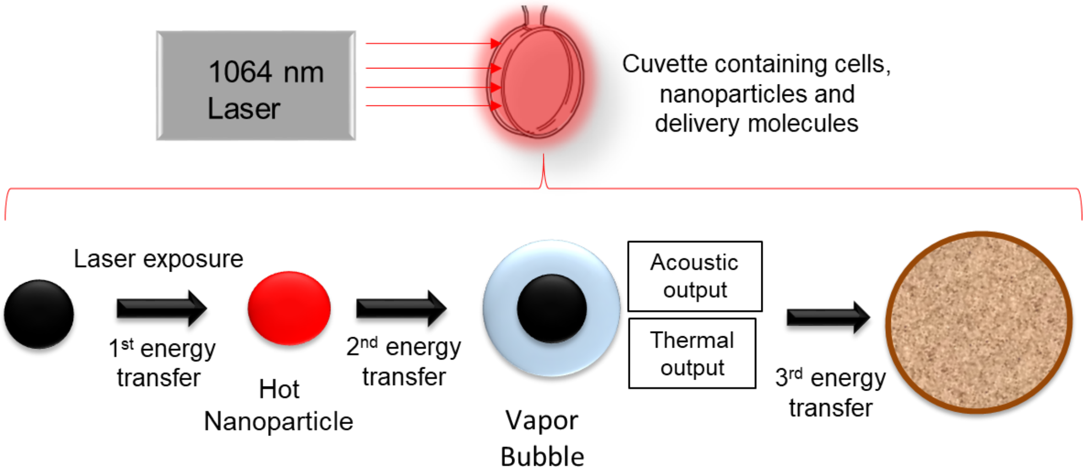

Figure 3.1: Schematic representation of energy transfer steps involved in nanoparticle-mediated photoporation. During laser irradiation, first energy transfer happens from laser to nanoparticles that causes nanoparticle temperature to rise. Second energy transfer happens from hot nanoparticle to surrounding fluid media. If temperature of nanoparticle becomes greater than 100°C, surrounding fluid starts to vaporize and causes rapid volume expansion. Third energy transfer happens from cell suspension media to cell membrane, where the acoustic and thermal energies emitted by nanoparticle, in combination with fluid flow interact with cell membrane and cause pore formation

We can break this process down into a series of steps (Figure 3.2). First, energy is emitted from the laser, which is controlled by parameters such as laser fluence, wavelength, pulse length and number of pulses (i.e., laser operating parameters). Next, energy is absorbed by CB nanoparticles (making them hot), which is controlled by parameters such as nanoparticle optical, thermal and physical properties like material, size and shape, as well as nanoparticle concentration (i.e., nanoparticle parameters). At 1064 nm wavelength, very little laser energy is absorbed by water, cells or anything other than the CB nanoparticles.

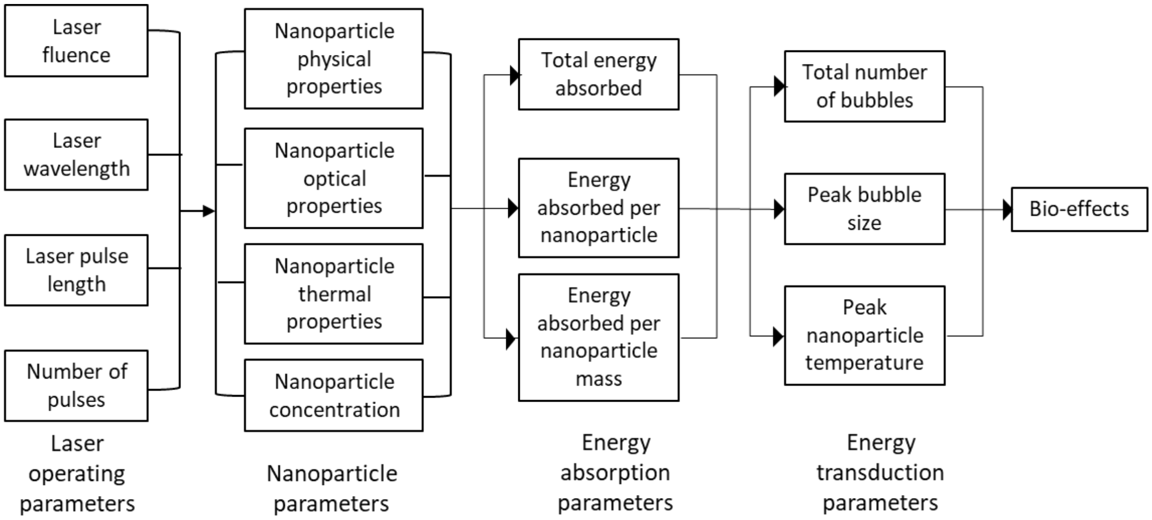

Figure 3.2: A schematic representation of the relationship of factors influencing the energy transfer process from laser to nanoparticle to fluid medium and cells that lead to bio-effects.

The amount of energy absorbed by the nanoparticles can be characterized in multiple ways, such as the total energy absorbed, energy absorbed per nanoparticle and energy absorbed per nanoparticle mass (i.e., energy absorption parameters). Finally, energy absorbed by the CB nanoparticles is then emitted to the surrounding water, which can be vaporized, and transferred to nearby cells to cause bio-effects, which is controlled by vapor bubble size, temperature and number of bubbles, among other parameters (i.e., energy transduction parameters).

In this study, we consider how these various parameters influence cellular bio-effects such as intracellular delivery, loss of cell viability and cell fragmentation, which are believed to be the result of progressively stronger forms of energy transduction to the cells. Prior work has considered relationships between bio-effects and laser operating parameters, which has shown correlation [9]. In this study, we seek to examine relationships between bio-effects and parameters that are closer in the energy transfer process to the cellular impact, namely the nanoparticle absorption parameters, energy parameters and energy transduction parameters. We hypothesize that the energy transduction parameters will correlate best with bio-effects as they are likely more closely related to the mechanism of action since they characterize the energy transduced to the cells, rather than further upstream processes.

3.2 Materials and methods

3.2.1 Cell culture

DU145 human prostate carcinoma cells (American Type Culture Collection, Manassas, VA) were cultured in adherent tissue culture flasks. Roswell Park Memorial Institute (RPMI) 1640 Medium (Cellgro, Herndon, VA) with 10% Fetal Bovine Serum, FBS (Corning, Palo Alto, CA) and 1% Penicillin-streptomycin (P/S) (Cellgro) were used as media for cell growth during incubation period. Culture flasks containing cells were incubated at 37^oC, 5% CO_2 and 98% relative humidity levels for growth. After 85% surface confluency was reached, cells were harvested using 0.25% Trypsin/EDTA (Cellgro). Subsequently, these cells were suspended in RPMI at a concentration of 10^6 cells/mL for experiments.

3.2.2 Nanoparticle dispersion preparation

Various nanoparticle dispersions were prepared using powdered nanoparticles and de-ionized (DI) water. CB nanoparticles (primary particle size of 25 nm, Black Pearls 470, Cabot, Boston, MA), CB nanoparticles (primary particle size of 90 nm, Asbury Carbon, Asbury, NJ), CB nanoparticles (average primary particle size of 367 nm, Continental

Carbon Company, Houston, TX), Copper nanoparticles (Cu, primary particle size of 25 nm, Sigma-Aldrich, St. Louis, MO), Silica nanoparticles (primary particle size of 10-20 nm, Sigma-Aldrich), Silicon Carbide nanoparticles (SiC, primary particle size of 40 nm, SkySpring Nanomaterials Inc. Houston, TX), Zinc Oxide nanoparticles (ZnO, primary particle size of 10-30 nm, SkySpring Nanomaterials Inc.), Graphite nanoparticles (primary particle size of 3-4 nm, SkySpring Nanomaterials Inc. Houston), Diamond nanoparticles (primary particle size of 3-4 nm, SkySpring Nanomaterials Inc.), Multi-Walled Carbon Nanotube (MWCNT1020, outer diameter 10-20 nm, SkySpring Nanomaterials Inc.), Multi-Walled Carbon Nanotube (MWCNT2030, outer diameter 20-30 nm, SkySpring Nanomaterials Inc.) and Single-Walled Carbon Nanotube (SWCNT1020, diameter 1-2 nm, SkySpring Nanomaterials Inc.) were all procured in powdered form.

Nanoparticles dispersion was prepared at a concentration of 400 mg/L (unless otherwise mentioned) in DI water containing 0.013% (v/v) Tween-80 (Sigma-Aldrich, St. Louis, MO), which was used to prevent particle aggregation. The dispersion was then homogenized through 35 min sonication in an ultrasonic water bath (FS3OH, Fisher Scientific, Pittsburg, PA) and then 1 min sonication with an ultrasonic needle (Sonics Ultracell, Sonics & Materials, Newton, CT). Dynamic light scattering (DLS) measurements (ZetaSizer Nano, Malvern Instruments, Malvern, UK) provided aggregate size Table 3.1. Zeta potential (measured using Zetasizer) in Table 3.1 values suggest that not every nanoparticle dispersion was stable. Therefore, fresh dispersions were prepared for each nanoparticle before conducting laser exposure experiments. In addition, prior to actual laser irradiation, samples were vortexed to ensure homogeneous distribution of cells and nanoparticles.

Table 3.1: Average diameter and zeta potential of nanoparticles dispersed in DI water at 26.3 mg/L concentration

Nanoparticle	Average diameter of nanoparticle aggregates in dispersion (DLS) (nm)	Zeta Potential (mV)
Silica	340	-25.1
ZnO	263	24.5
SiC	546	-7
Cu	307	12.5
Diamond	223	24.3
Graphite	323	31.3
MWCNT 2030*	233	-23
MWCNT 1020#	227	-17.1
SWCNT¥	256	-16.6
CB$	195	-23.5

*MWCNT2030 – multi-walled carbon nanotube, outer diameter 20-30 nm

#MWCNT1020 – multi-walled carbon nanotube, outer diameter 10-20 nm

¥SWCNT – single-walled carbon nanotube

$CB – spherical carbon nanoparticle

3.2.3 Laser exposure sample preparation

Exposure samples were prepared with 520 µL of DU145 cells (10^6/mL) suspended in RPMI, 37 µL of given nanoparticle dispersion and 5.5 µL of calcein (Molecular Probes, Eugene, OR) solution (at a final concentration of 10 µM) in a 1.5 mL Eppendorf tube. To minimize cellular functionality during storage, samples were kept in ice bath before and after laser exposure.

3.2.4 Laser exposure and sample wash

Cells were exposed to laser beam in a 2 mm wide and 21 mm diameter cylindrical Pyrex glass cuvette (37-PX-2, Starna Cells, Atascadero, CA) with an Nd:YAG solid-state laser (Continuum Powerlite II Plus, Continuum, San Jose, CA) that generate 5-9 ns pulses of 1064 nm wavelength at a frequency of 10 Hz. Laser beam was manipulated to irradiate the whole cuvette surface area (21 mm diameter), with homogeneous energy profile. Immediately after exposure, samples were transferred back to the Eppendorf tubes and stored in ice. “Sham” samples with cell suspended in RPMI, nanoparticles and calcein experienced similar procedures except laser irradiation and were used as negative controls.

Propidium Iodide (PI) (Invitrogen, Grand Island, NY) added at a concentration of 13.4 μM, was used to label non-viable cells after laser irradiation. Excess calcein and CB nanoparticles were removed from cell suspension through centrifugation at 500 g and subsequent washing (repeated 3 times) with phosphate buffer saline (PBS) before analysis.

3.2.5 Data collection

Flow cytometer – Cellular bio-effects were quantified using a bench-top flow cytometer (BD Accuri, BD Biosciences, San Jose, CA) and were categorized as viable cells with intracellular uptake and non-viable cells (i.e. intact cells with PI staining). Fluorescence of cells with calcein uptake was measured using 530/28 nm bandpass filter with excitation at 488 nm and fluorescence of cells with PI stain was measured using a 670 nm longpass filter with an excitation at 535 nm. Cell samples were run at constant flow rate of 35 μL/min for 1 min. “Cells only” negative control in RPMI was used to gate intact cells in the forward-scattered (FSC) and side-scattered (SSC) analysis. Fragmented cells were calculated as the difference between the number of viable cells counted in a laser exposed sample and the number of viable cells counted in sham.

Absorbance measurements - 1064 nm wavelength light absorbance of nanoparticles were measured using spectrophotometer (Evolution 220, Thermo Scientific, MA). After nanoparticle dispersion was prepared, they were mixed with RPMI at a given concentration and transferred to a cuvette provided as sample holder. A baseline measurement was done with only RPMI and all the absorbance values reported here have baseline value subtracted to provide the true absorbance of each nanoparticle dispersion. It is important to note that the values given by spectrophotometer includes both absorbance and scattering.

Bulk temperature-rise measurements - For bulk temperature rise measurements, a suspension of 560 µL nanoparticle dispersion in RPMI at a concentration of 26.3 mg/L was irradiated with 1064 nm wavelength laser pulses for 1 min at 88mJ/cm^2 laser fluence. Temperature measurements were taken using a standard J-type thermocouple immediately before and after the laser exposure. A baseline temperature rise measurement was taken for RPMI only and all the temperature values reported here have baseline value subtracted, to provide the true rise because of the presence of each nanoparticle.

3.2.6 Data analysis

A minimum of 3 replicates were used for each experimental condition. Mean and standard error of the mean were calculated using the 3 replicates. One-way analysis of variance (ANOVA, $\alpha = 0.05$) was performed to compare 3 or more experimental conditions using Graphpad Prism 8 (GraphPad Software, La Jolla, CA) followed by post-hoc Tukey’s pairwise comparison. A value of $p < 0.05$ was considered statistically significant

3.3 Results

3.3.1 Relationship between type of nanoparticle and bio-effects

Our initial studies sought to understand the relationship between nanoparticle absorption parameters and bio-effects by examining by changing nanoparticle composition and geometry. Cell suspensions mixed with different nanoparticle materials were irradiated with pulsed NIR laser. Subsequently, through flow cytometer analysis, cells were found to fall into one of four categories: viable cells with little or no intracellular uptake of calcein that appeared to be unaffected by the treatment (i.e., no fluorescent staining); viable cells containing calcein, (i.e., green fluorescence of the uptake marker, but no red fluorescence of the marker of non-viable cells, i.e., PI), hereafter termed as uptake cells; non-viable cells (i.e., red fluorescence of PI) and fragmented cells (i.e., cells identified as "lost" based on reduced cell concentration). We categorized the cells in the latter three groups as having bio-effects from the laser exposure and these are the categories plotted in the stacked bars shown in the subsequent figures. We interpret these bio-effects to follow a continuum, where cells with uptake had milder bio-effects, non-viable cells experienced stronger bio-effects and fragmented cells felt the strongest bio-effects.

When cells were irradiated in the presence Silica, ZnO, SiC, Cu and diamond nanoparticles (all at the same concentration on a mass basis), less than 20% cells had bio-effects and less than 11% cells showing calcein uptake (Figure 3.3).

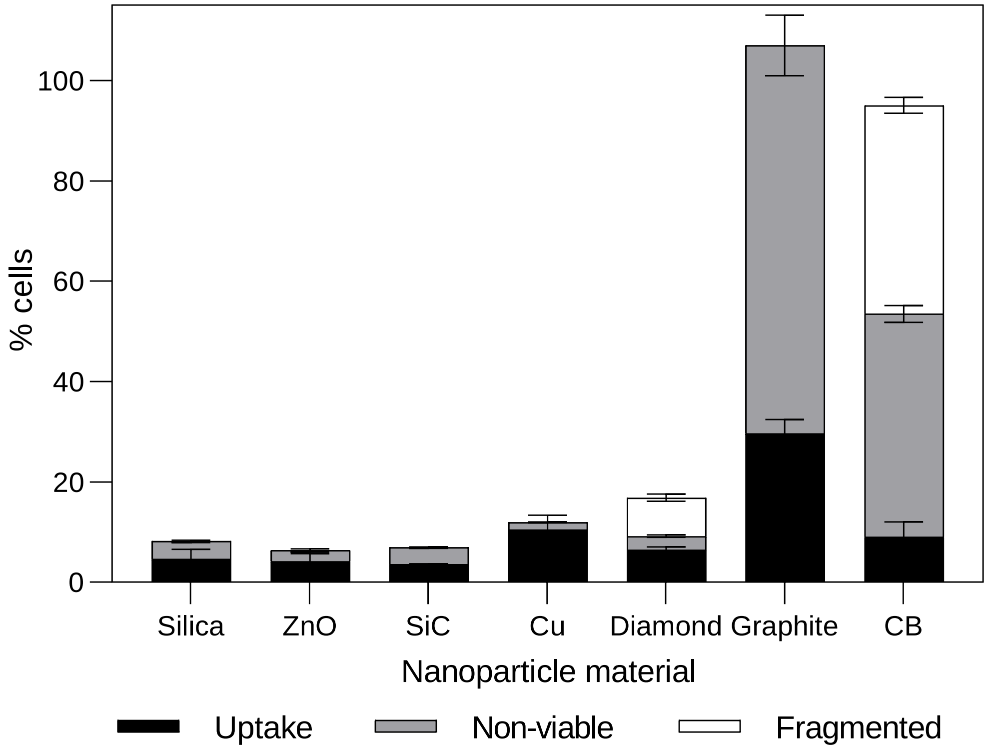

Figure 3.3: Bio-effects of cells suspended with different types of nanoparticles after laser exposure of DU145 cells at a fluence of 88 mJ/cm^2 for 1 min. All samples contained 26.3 mg/L nanoparticles and 10 µM calcein. Nanoparticle properties are provided in Table 3.1. Data are expressed as mean ± SEM based on 3 replicates each

In comparison, cells suspended with graphite and CB nanoparticles (at the same mass concentration) had significantly higher bio-effects, with more than 90% of cells showing some effect (one-way ANOVA, $p < 0.0001$ for uptake, non-viable and fragmented cells). We interpret the bio-effects in presence of CB nanoparticles as the strongest since more percentage of cells had fragmented and thus faced stronger bio-effects. Overall, CB nanoparticles can be comparatively seen as most efficient transducer of energy leading to bio-effects. For the next study, carbon nanoparticles of different shapes were suspended with cells and exposed to photoporation. Figure 3.4 shows that spherical CB nanoparticles were most efficient in causing photoporation followed by SWCNT (one-way ANOVA, $p < 0.0001$ for uptake, non-viable and fragmented cells). More than 85 ± 2% of cells lost viability due to cell death or fragmentation, when exposed to laser pulses in presence of CB nanoparticles.

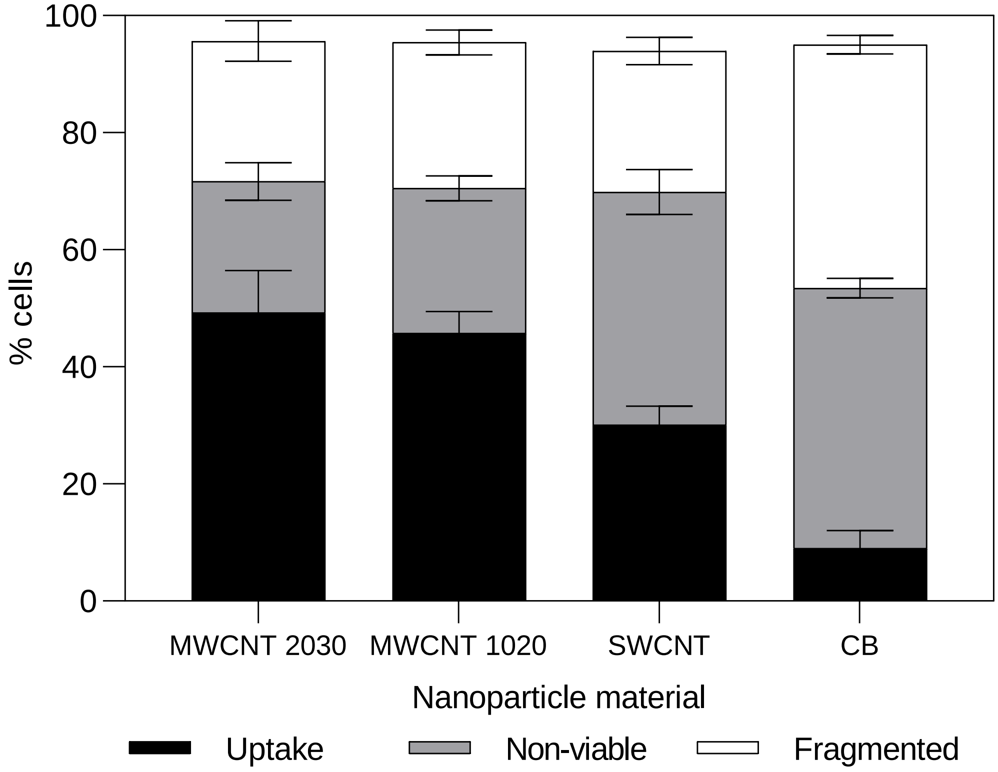

Figure 3.4: Bio-effects of cells suspended with carbon nanotubes and CB nanoparticles after laser exposure of DU145 cells at a fluence of 88 mJ/cm^2 for 1 min. All samples contained 26.3 mg/L nanoparticles and 10 µM calcein. Nanoparticle properties are provided in Table 3.1. Data are expressed as mean ± SEM based on 3 replicates each.

In comparison, ~ 64 ± 4% cells lost viability when suspended with SWCNT and < 50% of cells lost viability when suspended with MWCNTs. Both the MWCNTs performed similarly, with no statistically significant differences in bio-effects (Tukey's multiple comparison tests, $p > 0.05$).

3.3.2 Relationship between nanoparticle energy absorbance properties and bio-effects

The first energy transfer in nanoparticle-mediated photoporation takes place from laser beam to nanoparticles. Therefore, we expect that nanoparticles with high absorbance of 1064 nm wavelength laser light would show higher bio-effects. Figure 3.5 shows the 1064 nm wavelength laser light absorbance (+scattering) measurements for different nanoparticles at the same mass concentration. Silica, ZnO, SiC, Cu and Diamond nanoparticles had insignificant differences in their measured absorbance values (Tukey's multiple comparisons test, $p > 0.05$), which were close to 0. On the other hand, SWCNT and CB nanoparticles had similar absorbance values ($p > 0.05$), higher than the rest of the nanoparticles.

Viewing Figure 3.3, Figure 3.4 and Figure 3.5 together indicates that the nanoparticles with greater laser energy absorption were also causing greater bioeffects. However, absorbance (+scattering) measurements only assess the nanoparticles' ability to absorb laser energy and does not provide information about energy transfer from nanoparticle to surrounding water and cells. Additionally, what we report as nanoparticle absorbance in face includes both absorbed and scattered light. It is important to note that scattered light would not be expected to play a role in energy transfer steps of nanoparticle-mediated photoporation.

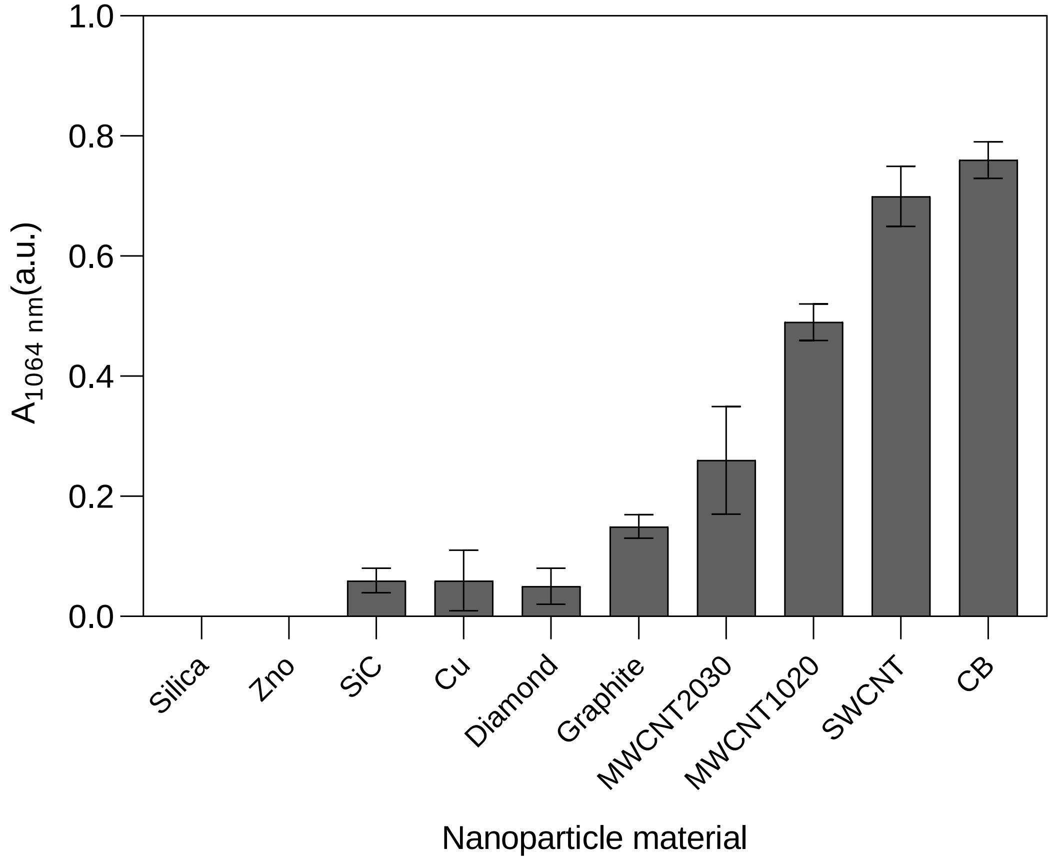

Figure 3.5: Absorbance (and scattering) of 1064 nm wavelength laser irradiation for different nanoparticles at 26.3 mg/L in DI water. Nanoparticle properties are provided in Table 3.1. Data are expressed as mean ± SEM based on 3 replicates each

To address this issue, we took bulk temperature rise measurements of the various nanoparticle suspensions after to laser irradiation, which should correlate with the nanoparticles' ability to absorb and dissipate energy, heating up the surrounding fluid, and not include energy associated with scattered light. No significant differences (Tukey's multiple comparisons test, $p > 0.05$) were observed in bulk temperature-rise values of nanoparticle suspensions made of Silica, ZnO, SiC, Cu, Diamond or Graphite (Figure 3.6), which were measured to be < 2^{o}C. In comparison, bulk temperature rise was measured to be significantly higher for MWCNTs, SWCNT and CB nanoparticles (Tukey's multiple comparisons test, $p < 0.05$) reaching 6°C or higher but, no significant differences were seen in measured temperature-rise values among these four carbon-based nanoparticles (Tukey's multiple comparisons test, $p > 0.05$).

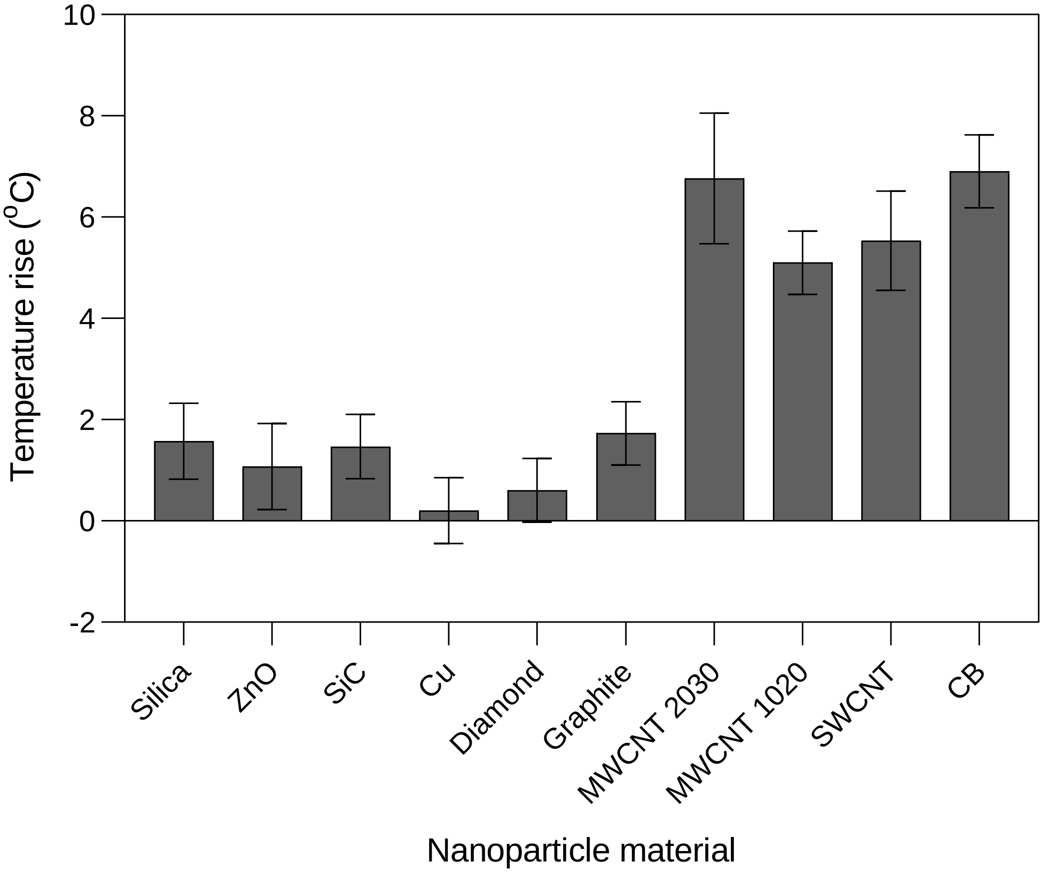

Figure 3.6: Bulk temperature rise of RPMI solution containing different nanoparticles at 26.3 mg/L exposed to laser pulses at 88 mJ/cm^2 fluence for 1 min. Nanoparticle properties are provided in Table 3.1. Data are expressed as mean ± SEM based on 3 replicates each.

When data from Figure 3.5 and Figure 3.6 were replotted as temperature-rise vs absorbance in Figure 3.7a, it can be seen that low absorbance values correspond to lower bulk temperature-rise and high absorbance values correspond to higher bulk temperature-rise. However, there is no direct dependence of temperature-rise on absorbance, but instead we see an apparently binary behavior, indicating that the CB and CNTs all absorb the laser light similarly (Figure 3.6) but scatter it differently (Figure 3.5). It can be assumed that

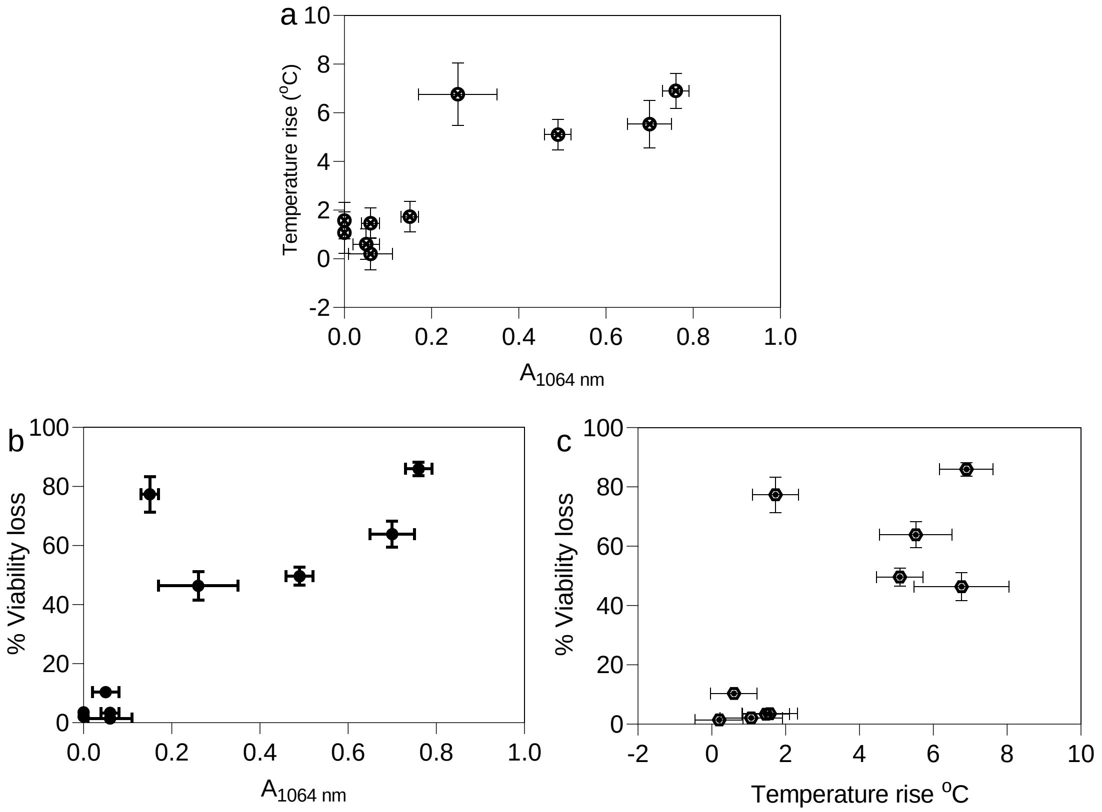

Figure 3.7: a) Bio-effects of cells suspended with different types of nanoparticles as a function of nanoparticle absorbance and bulk temperature rise. (a) Temperature rise as a function of nanoparticle absorbance. Data are from Figure 3.5 and Figure 3.6. (b) Cell viability loss (non-viable + fragmented cells combined) as a function of nanoparticle absorbance. Data are from Figure 3.3 - Figure 3.5. (c) Cell viability loss as a function of bulk temperature rise. Data are from Figure 3.3, Figure 3.4 and Figure 3.6. DU145 cells were exposed to laser at a fluence of 88 mJ/cm^2 for 1 min. All samples contained 26.3 mg/L nanoparticles and 10 µM calcein. Data are expressed as mean ± SEM based on 3 replicates each.

higher absorbance can lead to greater bio-effects when energy transferred in all the subsequent energy transfer steps are equal.

Based on these considerations, we plotted bio-effects as a function of nanoparticle energy absorbance (+ scattering) and as a function of temperature rise, which is a better measure of energy absorbance, in Figure 3.7b and c, respectively. While the bio-effects did depend on these two factors (one-way ANOVA, $p < 0.0001$), there was considerable scatter in the data, which did not show a clear trend or dependence. This may be because different nanoparticles absorb and release the same amount of energy, but way in which they release the energy (e.g., kinetics) may be different due to their different properties such as nanoparticle size, shape, heat capacity, thermal conductivity, etc.

3.3.3 Relationship between nanoparticle energy absorption parameters and bio-effects

So far, we have considered changes to nanoparticle parameters by changing nanoparticle material, size and shape to influence the process of converting laser energy into bio-effects. To better understand this process, we can account for the combination of laser operating parameters and nanoparticle parameters that lead to energy absorption parameters. Our goal was to vary laser and nanoparticle parameters to test three hypotheses to identify the dominant nanoparticle energy absorption parameter associated with bio-effects.

The first hypothesis is that the total energy absorbed is the dominant and correlates with bio-effects. This assumes that it does not matter how the energy is distributed among different numbers and sizes of nanoparticles; it is just the total energy that is absorbed, and then released, by those nanoparticles.

The second hypothesis is that the energy absorbed per nanoparticle is the critical parameter. This takes a more localized view that each individual nanoparticle has the opportunity to interact with a nearby cell, and it is the amount of energy absorbed and then released by each individual nanoparticle that determines bio-effects.

The third hypothesis is that energy absorbed per nanoparticle mass is most closely associated with bio-effects. This, in effect, means that each nanoparticle is heated to the same temperature (assuming all nanoparticles have the same heat capacity), and that may be the critical parameter driving bio-effects.

To identify the dominant parameter, each of the three nanoparticle energy absorption parameters was analyzed individually by keeping that parameter constant and varying other parameters by changing experimental conditions, including nanoparticle size, total number of nanoparticles, total mass of nanoparticles and laser fluence using CB nanoparticles.

The first nanoparticle energy absorption parameter analyzed was total energy absorbed with the hypothesis that total absorbed energy by the whole system is the dominant energy parameter. For this study, the number/concentration of CB nanoparticles and the laser fluence were varied to maintain constant total energy absorbed, which caused the energy per nanoparticle and energy absorbed per nanoparticle mass to vary as a result.

Figure 3.8 reveals that total bio-effects spanned from 18 ± 1% to ~95 ± 3% of cells while keeping total absorbed energy constant (one-way ANOVA, $p < 0.0001$). Additionally, cellular uptake percentage varied from ~16 ± 1% to ~71 ± 3%, non-viable cell percentage from ~3 ± 1% to ~18 ± 1% and fragmented cell percentage from ~0% to 6

± 1% (one-way ANOVA, p < 0.0001 for uptake, non-viable and fragmented cells). The data suggest that the total absorbed energy was not the dominant parameter.

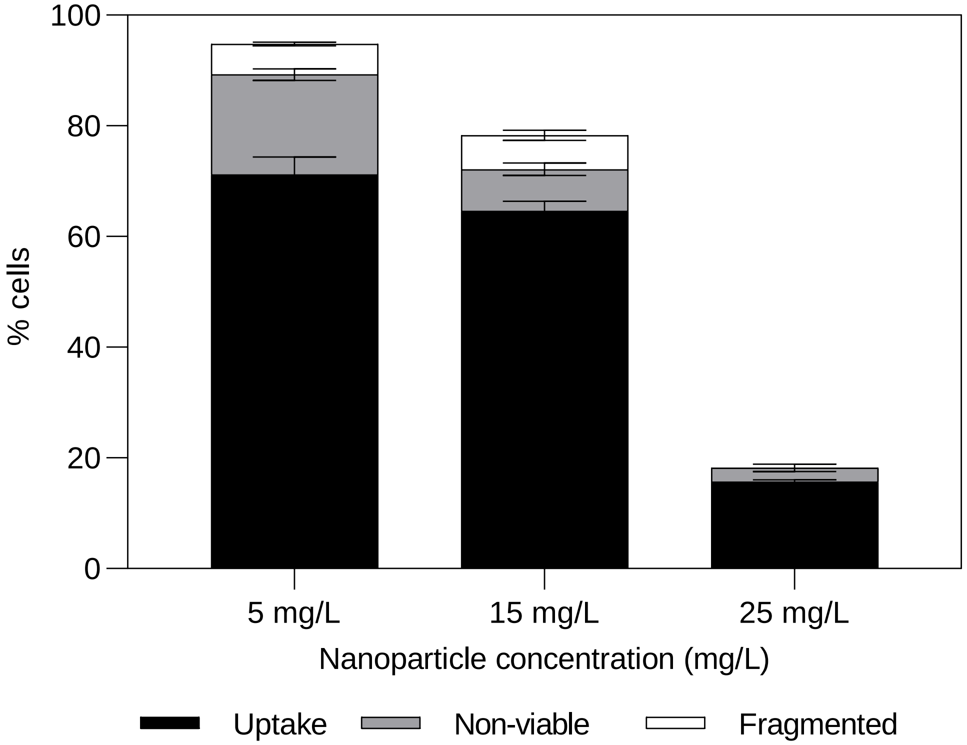

Figure 3.8: Bio-effects of cells exposed to three different experimental conditions with the same "total absorbed energy" of 3.7 mJ. Laser exposure was with 195 nm CB nanoparticles while varying total number of nanoparticles (1.7E+09, 5.1E+09 and 8.5E+09), nanoparticle concentration (5, 15 and 25 mg/L) and laser fluence (88, 29.33 and 17.6 mJ/cm^2). All samples contained 10 µM calcein. Data are expressed as mean ± SEM based on 3 replicates each.

Theoretical calculations at the conditions used in Figure 3.8 show that while total energy absorbed was kept constant at 3.7 mJ, the number of nanoparticles/bubbles varied from 1.7 x 10^9 to 8.5 x 10^9. An increase in number of bubbles suggests more opportunities for interaction with cells that should increase bio-effects. However, as number of nanoparticles/bubbles increased, bio-effects decreased (Figure 3.8). This might be explained by the decrease in calculated peak nanoparticle temperature (from 1810 ^{o}C to 380 ^{o}C) and vapor bubble radius (from 670 nm to 370 nm) with increasing nanoparticle concentration, because the constant total energy absorbed was distributed among more nanoparticles.

Next, we considered our second hypothesis, that energy absorbed per nanoparticle is the dominant nanoparticle energy absorption parameter. For this study, CB nanoparticle size and number, and laser fluence were varied to maintain constant energy absorbed per nanoparticle, which caused the total energy absorbed and energy absorbed per nanoparticle mass to vary as a result.

Figure 3.9 shows that total bio-effects varied from 7 ± 1% to ~97 ± 4% while keeping energy absorbed per nanoparticle constant (one-way ANOVA, $p < 0.0001$). Additionally, cellular uptake percentage varied from ~4 ± 1% to ~14 ± 2%, non-viable cell percentage from ~3 ± 1% to ~37 ± 3% and fragmented cell percentage from ~0% to 46 ± 3% (one-way ANOVA, $p < 0.0001$ for uptake, non-viable and fragmented cells). These data indicate that energy absorbed per nanoparticle was not the dominant parameter.

Theoretical calculations show that when energy absorbed per nanoparticle was kept constant at 2×10^{-09} mJ, the number of nanoparticles/bubbles varied from 2.1×10^{-08} to 8.5×10^{-09}, peak nanoparticle temperature varied from 65 ^{o}C to 1810 ^{o}C and vapor bubble radius ranged from 0 to 673 nm at the conditions used in Figure 3.9. The conditions with higher number of nanoparticle/bubbles, nanoparticle peak temperature and bubble radius corresponded to the conditions with the greatest bio-effects, which can explain the data.

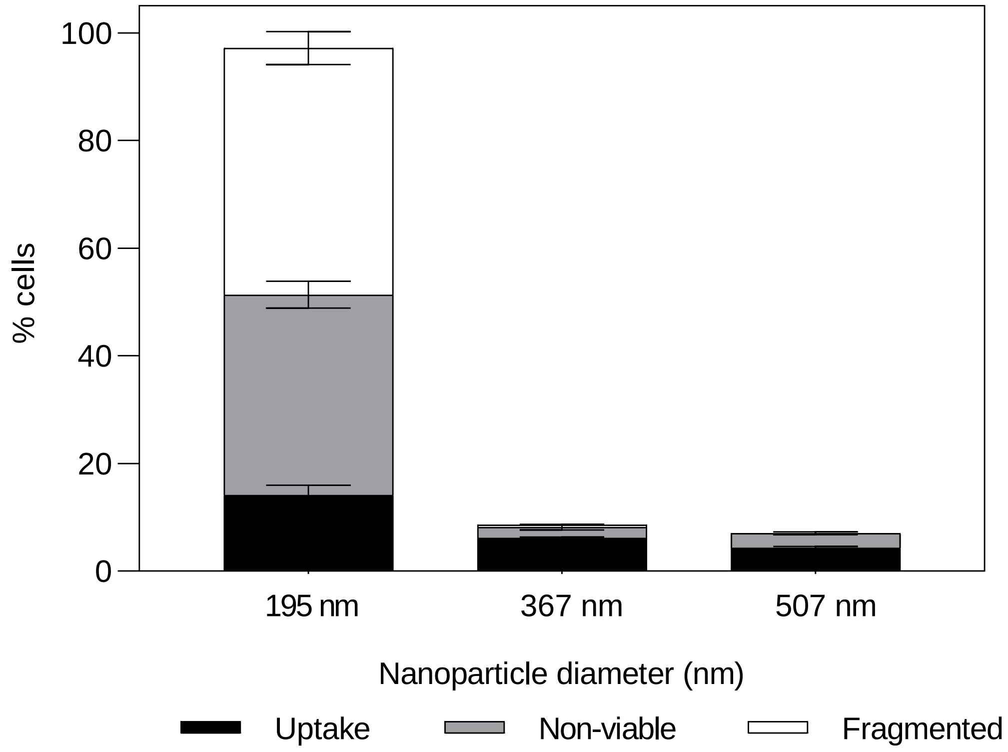

Figure 3.9: Bio-effects of cells exposed to three different experimental conditions with the same "energy absorbed per nanoparticle" of 2.06E-09 mJ per nanoparticle. Laser exposure was with 25 mg/L nanoparticles, while varying total number of nanoparticles (8.5E+09, 1.0E+09 and 2.1E+08), nanoparticle diameter (195, 367 and 507 nm) and laser fluence (88, 10.6 and 2 mJ/cm^2). All samples contained 10 µM calcein. Data are expressed as mean ± SEM based on 3 replicates each.

Finally, we examined our third hypothesis, that energy absorbed per nanoparticle mass is the dominant energy parameter. For this study, CB nanoparticle size and number, and laser fluence were varied to maintain constant energy absorbed per nanoparticle mass, which caused the total energy absorbed and energy per nanoparticle to vary as a result.

The data in Figure 3.10 show that total bio-effects varied between 33 ± 1% to ~84 ± 2%, while keeping energy absorbed per nanoparticle mass constant (one-way ANOVA, $p < 0.0001$). Additionally, cellular uptake percentage ranged from 22 ± 1% to ~51 ± 2% and non-viable cell percentage spanned 5 ± 1% to ~28 ± 1% (one-way ANOVA, $p < 0.0001$ for both uptake and non-viable cells), but fragmented cell percentage did not significantly vary (Tukey's multiple comparisons test, $p > 0.05$).

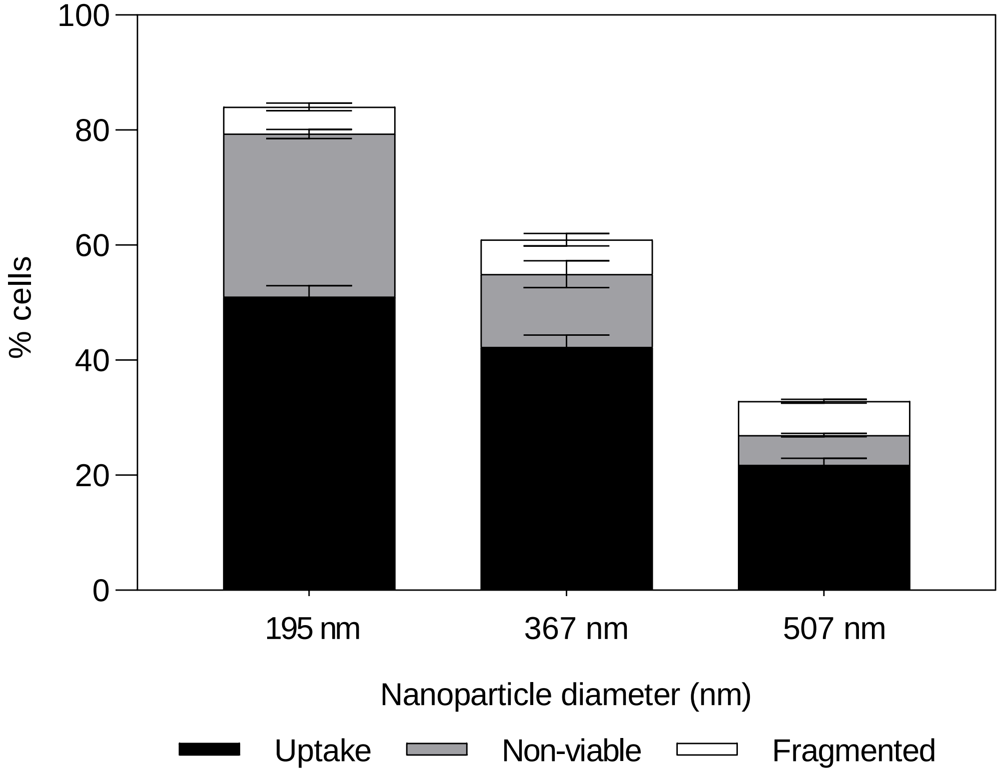

Figure 3.10: Bio-effects of cells exposed to three different experimental conditions with the same "energy absorbed per nanoparticle mass" of 355 mJ/mg. Laser exposure was with 25 mg/L nanoparticles, while varying total number of nanoparticles (8.5E+09, 1.0E+09 and 2.1E+08), nanoparticle diameter (195, 367 and 507 nm) and laser fluence (56.5, 57.9 and 51.3 mJ/cm^2). All samples contained 10 µM calcein. Data are expressed as mean ± SEM based on 3 replicates each.

Theoretical calculations reveal that when energy absorbed per nanoparticle mass was kept constant at 8 x 10^{+02} mJ/mg, the number of nanoparticles/bubbles varied from 2.1 x 10^{+08} to 8.5 x 10^{+09}. In Figure 3.10, bio-effects increased with increasing number of bubbles, which may explain the data. However, calculated peak nanoparticle temperature remained constant (at 1170 ^{o}C) and vapor bubble radius increased from 580 nm to 1970 nm as bio-effects decreased, which appears inconsistent with the expectations that larger bubbles should have greater bio-effects. It appears that the number of bubbles is more important than bubble size to cause bio-effects.

Overall, the data from Figure 3.8 to Figure 3.10 suggest that all three of our hypotheses are incorrect and that there is no single nanoparticle energy absorption parameter that dominates nanoparticle-mediated photoporation. Theoretical analysis of the data suggested that energy transduction parameters like number of bubbles, bubble size and bubble.

3.3.4 Relationship between energy transduction parameters and bio-effects

This analysis led us to design experiments to look for relationships between bio-effects and energy transduction parameters associated with bubbles created during photoporation. The hypothesis for this study is that increasing total number of bubbles, bubble radius and peak nanoparticle temperature all increase bio-effects. For the first case, total number of bubbles was varied (from 1.7E+09 to 8.5E+09), while keeping peak nanoparticle temperature (1810 ^{o}C) and peak bubble radius (670 nm) constant. We assumed that each nanoparticle generated a bubble and thus the number of bubbles was equal to the number of nanoparticles. To aid this assumption, laser fluence was chosen such that peak nanoparticle temperature was always well above 100 °C and hence, the heat dissipation would be expected to cause bubble formation from each nanoparticle.

Results in Figure 3.11 show that bio-effects increased with increasing total number of bubbles as shown by increases in non-viable and fragmented cell percentage from ~24 ± 2% to ~90 ± 3% (one-way ANOVA, $p < 0.0001$). As cells were killed, percentage of uptake cells decreased from 71 ± 8% to 7 ± 1% (one-way ANOVA, $p < 0.0001$). These data are consistent with total number of bubbles positively correlating with bio-effects.

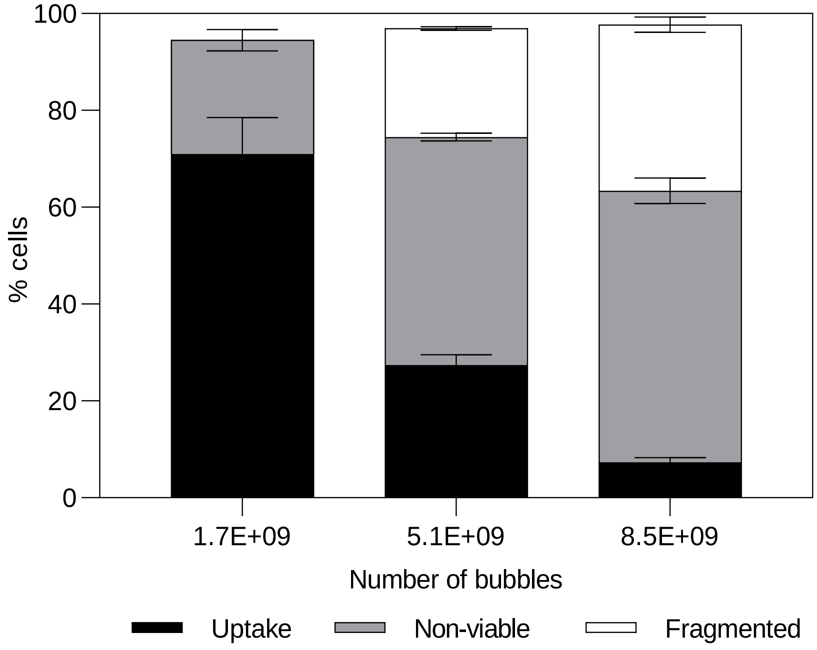

Figure 3.11: Bio-effects of cells exposed to three different experimental conditions with the same bubble radius (670 nm) and peak nanoparticle temperature (~1800 °C); and increasing total number of nanoparticles/bubbles (1.7E+09, 5.1E+09 and 8.5E+09), achieved by varying nanoparticle mass concentration (5, 15, 25 mg/L). Laser exposure was at a fluence of 88 mJ/cm^2 with 195 nm diameter CB nanoparticles. All samples contained 10 µM calcein. Data are expressed as mean ± SEM based on 3 replicates each.

Next, peak bubble radius was varied between 670 nm and 2300 nm, while keeping peak nanoparticle temperature (1800 °C) and total number of bubbles (5.5E+08) constant. Corresponding results in Figure 3.12 show that total bio-effects increased with increasing peak bubble radius, as shown by increases in non-viable and fragmented cell percentage from ~24 ± 1% to ~90 ± 5% with increasing of peak bubble size (one-way ANOVA, $p < 0.0001$). Percentage of uptake cells correspondingly decreased from 66 ± 4% to 6 ± 1% (one-way ANOVA, $p < 0.0001$). These data indicate that larger bubbles cause greater bio-effects.

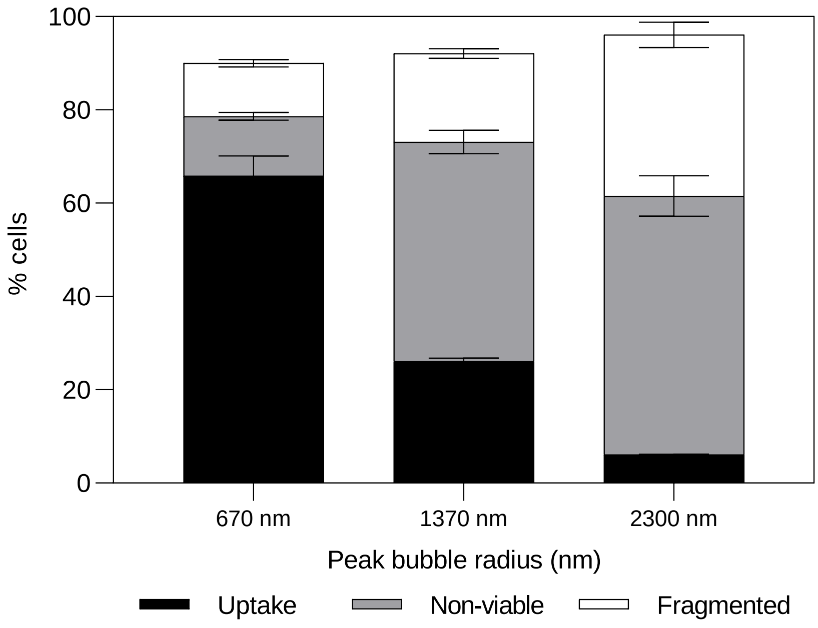

Figure 3.12: Bio-effects of cells exposed to three different experimental conditions with the same number of nanoparticles/bubbles (5.5E+08) and peak nanoparticle temperature (~1800 °C); and increasing peak bubble radius (670, 1370 and 2300 nm) using 195, 367 and 507 nm diameter CB nanoparticles, while varying nanoparticle mass concentration (1.6, 13.6, 63.9 mg/L) and laser fluence (88, 86.5 and 80.2 mJ/cm^2). All samples contained 10 µM calcein. Data are expressed as mean ± SEM based on 3 replicates each

Finally, peak nanoparticle temperature was varied from 140 ^oC to 1800 ^oC, while keeping total number of bubbles (5.5E+08) and peak bubble radius (670 nm) constant. Corresponding results in Figure 3.13 show that total bio-effects increased from ~7 ± 1% to ~89 ± 4% (one-way ANOVA, $p < 0.0001$). Additionally, uptake cell percentage increased from ~4 ± 1% to ~70 ± 4%, non-viable cell percentage increased from ~3 ± 1% to ~15 ± 1% and fragmented cell percentage increased from ~0.5 ± 0% to ~3 ± 0% with increasing peak nanoparticle temperature (one-way ANOVA, $p < 0.0001$ for uptake, non-viable and fragmented cells). These data show that nanoparticles heated to higher temperature caused greater bio-effects.

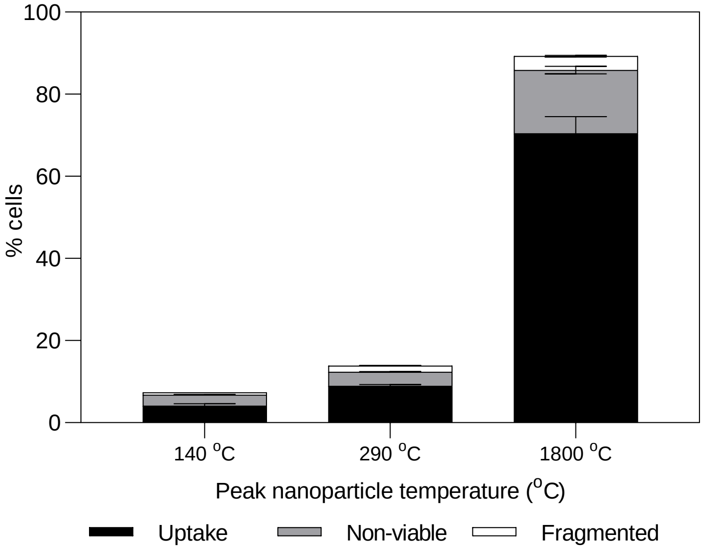

Figure 3.13: Bio-effects of cells exposed to three different experimental conditions with the same number of nanoparticles/bubbles (5.5E+08) and peak bubble radius (670 nm); and increasing peak nanoparticle temperature (140, 290 and 1800 ^oC) using 195, 367 and 507 nm diameter CB nanoparticles, while varying nanoparticle mass concentration (1.6, 13.6, 63.9 mg/L), and laser fluence (88, 13.3 and 5.3 mJ/cm^2). All samples contained 10 µM calcein. Data are expressed as mean ± SEM based on 3 replicates each.

3.3.5 Overall correlation between energy transduction parameters and bio-effects

We showed that three energy transduction parameters associated with bubbles correlated with bio-effects when the other parameters were held constant. Our next step was to determine how these parameters correlate with bio-effects when they are all allowed to vary. For this analysis, we used data from more than 100 different experimental conditions, and looked for correlation with total bio-effects, defined as the sum of uptake cells, non-viable cells and fragmented cells.

This analysis shows that there was a poor correlation between bio-effects and the individual energy transduction parameters: peak nanoparticle temperature (Figure 3.14a), total number of bubbles (Figure 3.14b) and peak bubble radius (Figure 3.14c) However, when we combined the values of all three parameters, a reasonable correlation emerges (Figure 3.14d). The combined parameter, P, accounts for (i) the total number of bubbles, which relates to the total number of bubble-cell interactions, (ii) the nanoparticle temperature, which is related to the bubble temperature that may drive the bio-effect interaction, and (iii) the bubble radius, which influences the lifetime of the bubble-cell interaction, since larger bubbles contain more energy with a smaller surface-to-volume ratio and therefore dissipate their energy over a longer period of time.

It is notable, however, that P does not weight the three energy transduction parameters equally. Correlation of bioeffects with the direct product of the three parameters was only fair ($R^2 = 0.75$). A much better correlation ($R^2 = 0.93$) was found when peak nanoparticle temperature (T) was raised to the power 2, number of bubbles (N) to the power 0.5 and peak bubble radius (R) to the power 0.25,

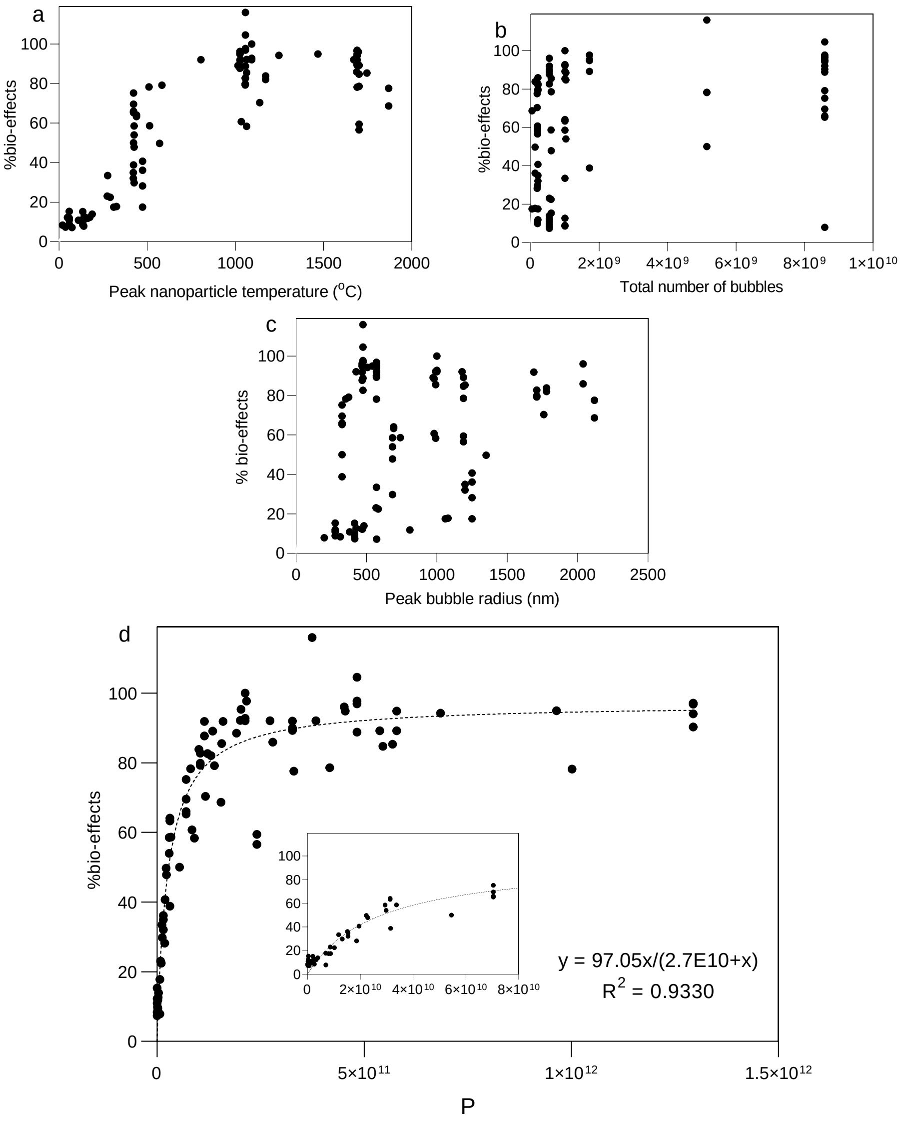

Figure 3.14: Changes in bio-effects as a function of energy transduction parameters after laser exposure of DU145 cell suspension over a range of experimental conditions. Total bio-effects (i.e., uptake, non-viable and fragmented cells) are shown as a function of (a) peak nanoparticle temperature, (b) total number of bubbles, (c) peak bubble radius and (d) the product P, which represents the product of (peak nanoparticle temperature)^2, (total number of bubbles)$^{0.5}$ and (peak bubble radius)$^{0.25}$. See Appendix D for correlations with uptake cells, viability loss and fragmentation. Data come from Figure 3.8 to Figure 3.13 and additional experiments. All samples contained 10 µM of calcein. Data are expressed as mean ± SEM based on 3 replicates each.

$$P = T^2 N^{0.5} R^{0.25} \tag{1}$$

While we should not try to read too much mechanistic information into this equation, it does suggest that temperature is the most important parameter that correlates with bioeffects, where number of bubble and bubble radius have progressively less significant impact.

3.4 Discussion

Nanoparticle-mediated photoporation has been explored as a novel molecular delivery platform in past either to investigate the underlying mechanism[6,7,102] or to study the effects of varying the operating conditions to attain optimum delivery conditions[9,12,127,143]. While these studies have varied laser operating parameters, previous work has not focused on nanoparticles' role as energy transducers by looking for relationships between nanoparticle, energy absorption and energy transduction parameters and the resulting bio-effects. This study was motivated by the need to understand the role of the energy transduction process from laser to nanoparticle to medium and cell.

Nanoparticle-mediated photoporation can be categorized to involve three crucial energy transfer steps - i) from laser to nanoparticle, ii) from nanoparticle to surrounding fluid and, iii) from fluid to cell membrane. Nanoparticles are directly involved in first two of those energy transfer steps since they absorb laser energy and transduce that into thermal form, that is dissipated in thermal and mechanical form from nanoparticle to surrounding fluid. By using a variety of nanoparticle material and shape, we learnt that bio-effects caused by nanoparticle-mediated photoporation are dependent on their absorbance values.

In general, a lower laser light absorbance corresponded to smaller bio-effects and a higher laser light absorbance corresponded to greater bio-effects.

Because our initial analysis of light absorbance also included scattered light, we performed a second analysis that accounted for just the energy absorbed by the nanoparticles by measuring system temperature change. In general, higher temperatures were associated with greater bio-effects, but a clear trend was not evident.

We next considered three hypotheses to explain the relationship between photoporation parameters and bio-effects. These hypotheses proposed that bio-effects would correlate with (i) total energy absorbed, (ii) energy absorbed per nanoparticle, or (iii) energy absorbed per nanoparticle mass. Total energy absorbed corresponds to the cumulative energy absorbed by all the nanoparticles and is available to be transferred into the surrounding fluid to cause photoporation. Energy absorbed per nanoparticle corresponds to the localized absorption and release of energy and thus controls the bubble formation. Energy absorbed per nanoparticle mass corresponds to the energy absorbed per unit mass of CB nanoparticles and thus controls the temperature increase of the nanoparticles.

This study was designed to investigate if any one of these energy parameters is dominant and correlates strongly, by itself, with photoporation. These energy parameters are directly related to operating conditions that include both nanoparticle composition and laser fluence, and are hypothesized to be mechanistically closer to the photoporation phenomenon. However, our study found that none of the three nanoparticle energy absorption parameters alone correlated with bio-effects, which rejected our three hypotheses regarding the existence of a single, dominant energy parameter.

Our final analysis addressed phenomena after the transduction of energy from laser light to heat to bubble formation by focusing on the energy transduction parameters that may be mechanistically closes to causing bio-effects. We found that total number of bubbles, bubble size and peak nanoparticle temperature each correlated with bio-effects when the other parameters were held constant.

Generation of more bubbles formed imply more sources of thermal, acoustic and fluid mechanical outputs that can effectively transfer energy to cell membrane to cause poration. Thermal output comes from the bubbles being hot (i.e., many hundreds and even thousands of degrees Celsius). Acoustic and fluid mechanical outputs from the rapidly expanding bubble generated by heat transfer from the nanoparticle to the surround fluid. It is not surprising that more sources of energy output can increase the changes of a close encounter between a nanoparticle and a cell that results in bio-effects. A similar dependence of cellular uptake and viability loss on cavitation bubble nucleation site concentration was observed for ultrasound-mediated intracellular delivery[144].

Increasing bubble size increased bio-effects. Bigger bubbles may bring bubbles closer to neighboring cells and may also generate greater acoustic and fluid mechanical effects. Bigger bubbles (at the same temperature) also have more energy that can impact cells and is released over a longer time due to reduced surface-to-volume ratio. Bubble size dependence has been previously investigated in cavitation based intracellular delivery methods that showed greater bio-effects for *in-vitro* applications[145,146] and better penetration depths for *in vivo* applications[147].

Finally, higher peak nanoparticle temperature, which related to peak bubble temperature, caused greater bio-effects. Higher peak nanoparticle temperature may impact cells by (i) increasing the rate of heat transfer from nanoparticle to surrounding fluid, thus affecting acoustic wave production, and ii) increasing the chances of direct heat transfer to cell membrane that could melt the lipids or otherwise disruption lipid bilayer structure, since nanoparticle with higher peak temperature can lead to more pores being formed for intracellular delivery[148].

A plausible way to understand the role of transient photoporation parameters on bio-effects is depicted in Figure 3.15. Essentially, bio-effects would be least for the case I, when no bubbles are formed during laser exposure due to nanoparticle heating below 100 °C. Even in this case, there could be bio-effects due to direct thermal energy transfer from nanoparticle to cell membrane. Next, when the bubbles do form (case II), bio-effects can be increased by increasing the number of bubbles (case III), increasing bubble size (case IV) and increasing peak nanoparticle (bubble) temperature (case V).

Guided by these findings, we combined data from more than 100 different experimental conditions and found a correlation between bio-effects and the product of the three energy transduction parameters, P. It is notable that the best correlation involved a power-law relationship with bio-effects scaling with peak nanoparticle temperature squared, and the total number of bubbles and peak bubble radius being raised to powers less than one. This correlation showed a Langmuir isotherm fit with bio-effects initially

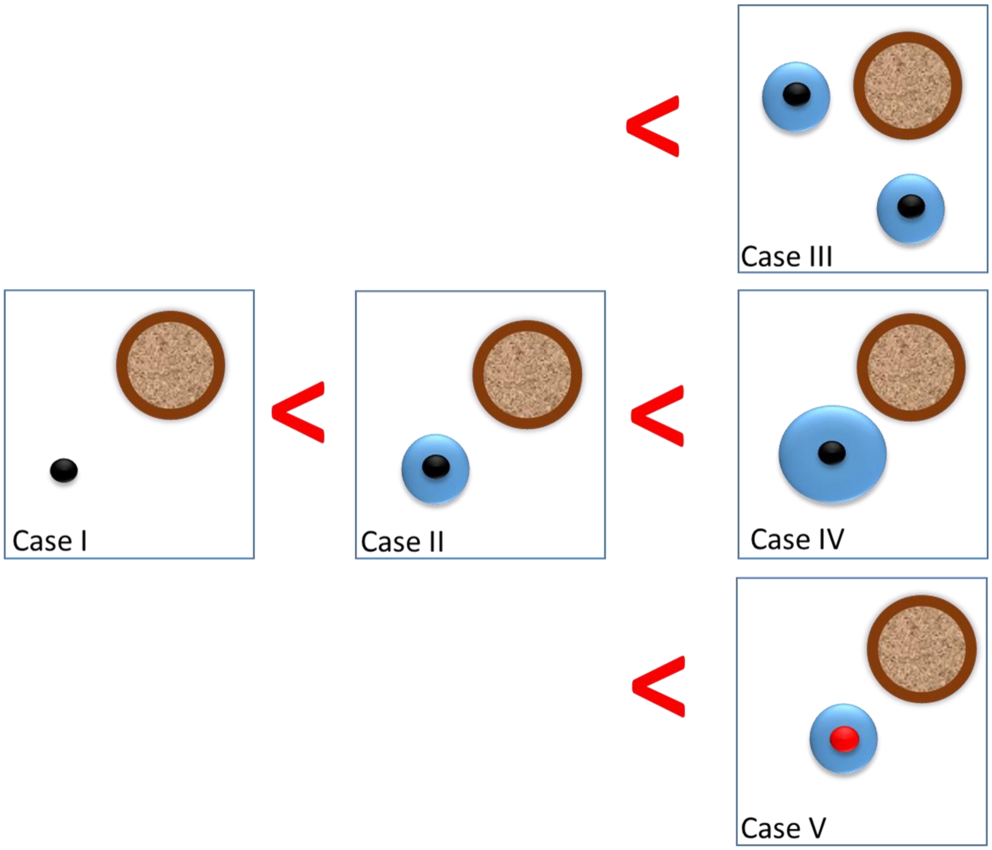

Figure 3.15: A schematic representation of the effects of number of bubbles, bubble size and peak nanoparticle temperature on nanoparticle-mediated photoporation and its subsequent bio-effects

increasing with increasing P value and then saturating around 100%. A higher power for peak nanoparticle temperature suggests that this parameter is a more important determinant of bio-effects. This correlation can be used for determining operating conditions in order to obtain a desired bio-effect (which indicates that different combination of the three parameters can have similar cellular response).

Note that this correlation does not account for the internal variations in bio-effects such as the ratios of uptake cells, non-viable cells and fragmented cells, which places limitations in its ability to provide delivery efficiency (*see Appendix D.2*). Additionally, only data on calcein delivery (at a fixed concentration) were used to generate this correlation and the exposure time was kept constant at 1 min (i.e. 600 pulses). Therefore, the correlation may not be applicable to estimate bio-effects under conditions not included in this study.

3.5 Conclusion

In this work, we examined the dependence of cellular bio-effects caused by nanoparticle-mediated photoporation on a variety of parameters expected to influence outcomes. We first found that nanoparticle composition strongly affects bioeffects, where CB and CNTs were much more effective than graphite, diamond and other non-carbon materials. These differences were partially explained by different laser absorption properties. Energy absorption by nanoparticles was characterized as total energy absorbed, energy absorbed per nanoparticle and energy absorbed per nanoparticle mass, but none of these parameters was found to dominate the energy transduction process leading to bio-effects.

We finally looked at energy transduction parameters more closely related to the energy form transferred to cells in terms of the temperature, size and number of vapor bubbles generated by the nanoparticles heated by the laser. These three parameters each individually correlated with bio-effects when the other two were held constant. An overall correlation with data from more than 100 different experimental conditions was obtained by multiplying the number of bubbles, size of bubbles and peak nanoparticle temperature, with the best correlation coming from a power law relationship that indicated that peak nanoparticle temperature was the strongest determinant of bio-effects among the three energy transduction parameters.

This study provides a better understanding of the physical parameters at play during nanoparticle-mediated photoporation, how they influence bio-effect outcomes and which ones are most important. This understanding also facilitates design of photoporation parameters that achieve a desired bio-effect.

CHAPTER 4. EFFECT OF SERUM ON CELLS DURING NANOPARTICLE-MEDIATED PHOTOPORATION

4.1 Introduction

Intracellular delivery of molecules has been of interest in recent years after the augmentation of several bio-molecules targeting intracellular components[149]. Delivery of exogenous material inside the cells have a variety of applications including cellular studies, therapies and bio-imaging[150]. A significant resistance to intracellular delivery comes from the plasma membrane, which is made of phospholipids that are amphipathic[151] and block the movement of foreign materials. There are bulk transport mechanisms e.g. endocytosis[152] which move particles across the cell membrane but these pathways often lead to degradation of original molecule, due to pH change and enzymatic degradation in endosomes, thereby discounting and/or completely preventing the interaction with target molecule in desired form[153,154].

Numerous technologies have been developed to facilitate this transport into cells. Researchers have explored biological[4] (e.g. viral vectors), chemical[155] (e.g. polymeric and particulate vectors) and physical[91] (e.g. microinjection, gene gun, sonoporation, electroporation) methods to design efficient intracellular delivery processes. Although these methods can be effective, there are still concerns of immunogenicity, toxicity, limited efficiency, low cell viability and restricted application.[4,5].

Nanoparticle-mediated photoporation provides an alternative to the current delivery methods. When a suspension of nanoparticles (such as CB) with cells and drug molecules, gets irradiated to laser beam, the nanoparticles absorb energy delivered by laser and dissipate the energy in form of heat and photoacoustic waves as well as fluid flow. This concentrated release of energy from the nanoparticles is believed to create transient pores on cell membrane allowing molecules to pass through into the cytosol without killing the cell.[6–8].

Previously, researchers performed studies to elaborate the mechanism involved during photoporation and also optimized the process for efficient intracellular delivery [7,9,11,156]. However, high percentage of cells become non-viable at higher laser fluence due to irreversible cell damage[9]. Increased viability loss is a common occurrence for physical delivery methods that involve external stress application on cell membrane to create transient pores[157,158]. Irreversible cell damage can have applications in targeted ablation of undesirable tissues such as cancer tumors[159]. However, cell viability loss becomes disadvantageous for intracellular delivery applications meant for research, diagnostic or therapeutic purposes. Majority of mitigation strategies revolve around using lower energy intensities or lowering the external stress exposure duration, which can limit the percentage of cells with molecular uptake.

Cellular viability loss has also been a common issue for large-scale suspension cell culture in sparged and agitated bioreactors[160] since 1960s. Observed cell damages were attributed to increased local shear near the cell membrane, caused by bubble breakup at the free surface of these bioreactors and draining foams[160]. To overcome this issue, FBS and certain polymers were introduced as viability protective agents against the shear damage seen in suspension cell culture. Specially, FBS has been used to protect cell viability against fluid mechanical damages in bioreactors [14,161] and to increase drug delivery efficiency[162,163].

Therefore, in order to increase percentage of cells with molecular uptake at high laser fluence in nanoparticle-mediated photoporation, we propose using FBS as cell viability protection additive. This is relevant not only to in vitro scenarios were FBS can be added, but also to in vivo setting where the extracellular fluid may resemble serum. We hypothesize that the presence of serum in cell suspension media during photoporation will increase percentage of viable cells resulting in higher cellular calcein uptake. Hence, this study was designed to investigate the effect of serum addition in cell suspension media during photoporation and further explore the physical and bio-chemical interactions brought about by serum introduction

4.2 Materials and methods

4.2.1 Cell preparation

DU145 human prostate carcinoma cells (American Type Culture Collection, Manassas, VA) were grown in tissue culture flasks with cell media containing RPMI 1640 Medium (Cellgro, Herndon, VA), with 10% FBS (Corning, Palo Alto, CA) and 10 mL P/S (Cellgro). Human Dermal Fibroblast (HDF) cells were grown in tissue culture flasks containing Dulbecco's Modified Eagle's Medium (DMEM) (Gibco, Dublin, Ireland), supplemented with 10% FBS and 1% P/S. Each cell type was incubated at 37^{o}C, 5% CO_2 and 98% relative humidity levels during growth period. Cells were cultured at 85% confluency using 0.25% Trypsin/EDTA (Cellgro). After harvesting, DU145 cells were suspended in RPMI and HDF cells were suspended in DMEM (unless otherwise mentioned) at a concentration of 10^6 cells/ml.

4.2.2 Nanoparticle dispersion preparation

CB nanoparticle dispersion preparation was done using 25 nm diameter CB nanoparticles (Black Pearls 470, Cabot, Boston, MA) and DI water. CB nanoparticles were added at a concentration of 400 mg/L to DI water containing 0.013% (v/v) Tween-80 (Sigma-Aldrich, St. Louis, MO) to enhance solution stability (prevent particle aggregation for a homogeneous dispersion). The solution was first sonicated for 35 min in an ultrasonic water bath (FS3OH, Fisher Scientific, Pittsburg, PA) and then with an ultrasonic needle for 1 min (Sonics Ultracell, Sonics & Materials, Newton, CT). CB nanoparticles tend to aggregate in aqueous dispersions and thus the final aggregate diameter was measured to be 195 nm using dynamic light scattering (DLS) measurements (ZetaSizer Nano, Malvern Instruments, Malvern, UK).

4.2.3 Cell suspension media preparation

Cell suspension media was prepared by adding FBS, bovine serum albumin (BSA), Hemoglobin (HG), Polyethylene glycol (PEG), Poly(N-(2-hydroxypropyl) methacrylamide) (PHPMA), Polyvinylpyrrolidone (PVP), Poly(2-ethyl-2-oxazoline) (PEOX) or Pluronic F127 (Sigma Aldrich) in RPMI. The polymer suspensions were sonicated in water bath for 5 min before use to dissolve and homogenize the suspension media. After this, cells were added in suspension media immediately after harvesting, at a concentration of 10^6 cells/ml.

4.2.4 FBS protein denaturization

Denatured protein suspensions were prepared in two ways. Thermal denaturization – FBS solution was heated in a water bath at temperature of 100 ^oC for 60 min[164]. Mechanical denaturization – FBS solution was sonicated for 40 rounds of sonication with 5 pulses (of 1 sec) in each round followed by 1 min of incubation period[165]. Both were then added in RPMI to prepare appropriate concentrations of FBS solution.

4.2.5 Exposure Sample preparation and laser exposure

Exposure samples were prepared by mixing 520 µL of DU145 cells (10^6/mL) suspended in RPMI or other cell suspension media mentioned above, 37 µL of 400 mg/L CB dispersion and 5.5 µL of 1 mM calcein (Molecular Probes, Eugene, OR) solution in a 1.5 mL Eppendorf tube. The final CB nanoparticle concentration became 26.3 mg/L and calcein concentration became 10 µM. Samples were stored in ice bath to reduce endocytosis/cellular activity before and after-laser exposure.

Cell samples were transferred to a 2 mm wide and 21 mm diameter cylindrical Pyrex glass cuvette (37-PX-2, Starna Cells, Atascadero, CA) for laser exposure. An Nd:YAG solid-state laser (Continuum Powerlite II Plus, Continuum, San Jose, CA) was used as laser source to apply 5-9 ns pulses of 1064 nm wavelength at a frequency of 10 Hz for 1 min. Laser fluence was varied between 25 and 88 mJ/cm^2, Samples were exposed to laser beam (21 mm diameter), which irradiated the whole surface with flat top (uniform) energy profile. Immediately after exposure, samples were transferred back to the Eppendorf tubes and stored in ice. Negative controls in the form of 'sham' exposures were samples containing cells, CB nanoparticles, and calcein that experienced the same handling and procedures except the laser exposure. To label non-viable cells post laser-irradiation, propidium iodide (PI) (Invitrogen, Grand Island, NY) was added at a final concentration of 13.4 μM and incubated for 10 min on ice. Cell samples were then centrifuged at 500 g for 6 min and washed with phosphate buffer saline (PBS) for 3 times to remove excess calcein from the bulk solution before analysis.

4.2.6 Data collection

Cells were analyzed using a bench-top flow cytometer (BD Accuri, BD Biosciences, San Jose, CA) to quantify bio-effects in terms of cell viability (based on red PI fluorescence) and intracellular uptake (based on green calcein fluorescence). Calcein fluorescence was measured using 530/28 nm bandpass filter with excitation at 488 nm and PI fluorescence was measured using a 670 nm longpass filter with a excitation at 535 nm. Cell samples were run at constant flow rate of 35 μL/min for 1 min. Cells with calcein fluorescence greater than in sham cells incubated in calcein and PI but not exposed to laser irradiation were considered to have intracellular uptake. Cells with PI fluorescence greater than in sham cells were considered to be non-viable.

A negative control containing only cells in RPMI was used to construct a cell population gate in the forward-scattered (FSC) and side-scattered (SSC) analysis. Cells within this gate were considered to be intact cells. To account for possible cell loss due to cell fragmentation (appearing as low forward scatter and low side scatter events on the flow cytometer), the difference between the number of viable cells detected in a given sample and the number of viable cells detected in sham samples was taken as the number of cells lost to fragmentation.

For bulk temperature rise measurements, a suspension of 560 μL nanoparticle dispersion in RPMI at a concentration of 26.3 mg/L was irradiated with 1064 nm wavelength laser pulses for 1 min at 88 mJ/cm^2 laser fluence. Temperature measurements were taken using a standard J-type thermocouple immediately before and after the laser exposure. A baseline temperature rise measurement was done using RPMI only and all the temperature values reported here have baseline value subtracted, to provide the true rise because of the presence of the nanoparticle dispersion.

4.2.7 Data analysis

A minimum of 3 replicates were used for each experimental condition. Mean and standard error of the mean were calculated using the 3 replicates. One-way analysis of variance (ANOVA, $\alpha = 0.05$) was performed to compare 3 or more experimental conditions using Graphpad Prism 8 (GraphPad Software, La Jolla, CA) followed by post-hoc Tukey's pairwise comparison. A value of $p < 0.05$ was considered statistically significant

4.3 Results

4.3.1 Effects of serum addition on cellular bio-effects during photoporation

To evaluate the effect of serum on nanoparticle-mediated photoporation, cells were suspended in RPMI alone or containing up to 15% v/v FBS in the presence of CB nanoparticles and calcein, and then exposed to nanosecond, pulsed laser. Using flow cytometry, cells were found to fall into one of four categories: viable cells with little or no intracellular uptake of the uptake marker (i.e., no fluorescent staining); viable cells containing uptake marker (i.e., green fluorescence of calcein, but no red fluorescence of

PI) hereafter referred to as uptake cells; non-viable cells (i.e., red fluorescence of PI); and fragmented cells (i.e., cells identified as "lost" based on reduced cell concentration). We interpret all cells in the latter three groups as having bio-effects from the laser exposure. We can further think of bio-effects following a continuum, where uptake cells had milder bio-effects, non-viable cells experienced stronger bio-effects and fragmented cells felt the strongest bio-effects.

For cells suspended in RPMI without serum, exposure at the lowest laser fluence (25 mJ/cm^2) led to ~30 ± 3% of cells with uptake of calcein and ~10 ± 2% of cells non-viable or fragmented (Figure 4.1a). At the next higher laser fluence (33 mJ/cm^2), bio-effects increased, with ~58 ± 6% of cells showing calcein uptake and ~20 ± 3% of cells non-viable or fragmented (Tukey's multiple comparisons test, $p < 0.0001$ for uptake, $p > 0.05$ for non-viable and $p > 0.05$ for fragmented). At still higher laser fluence, bio-effects continued to increase, but the percentage of cells with calcein uptake decreased, while non-viable and fragmented cells increased (one-way ANOVA, $p < 0.0001$ for uptake, non-viable and fragmented cells). These findings indicate that the maximum percentage of cells with calcein uptake was limited by loss of cell viability as laser-mediated bio-effects increased.

In comparison, cells suspended with FBS were able to maintain high viability even with increased laser fluence, and thereby achieved high levels of uptake (Figure 4.1a). Although laser exposure at the lowest fluence (25 mJ/cm^2) produced a lower percentage of cells with calcein uptake compared to cells in RPMI alone (one-way ANOVA, $p < 0.0001$), the population of cells with uptake continued to grow with increasing fluence until 55 mJ/cm^2 (two-way ANOVA, $p < 0.0001$), after which, the uptake appeared to saturate at as

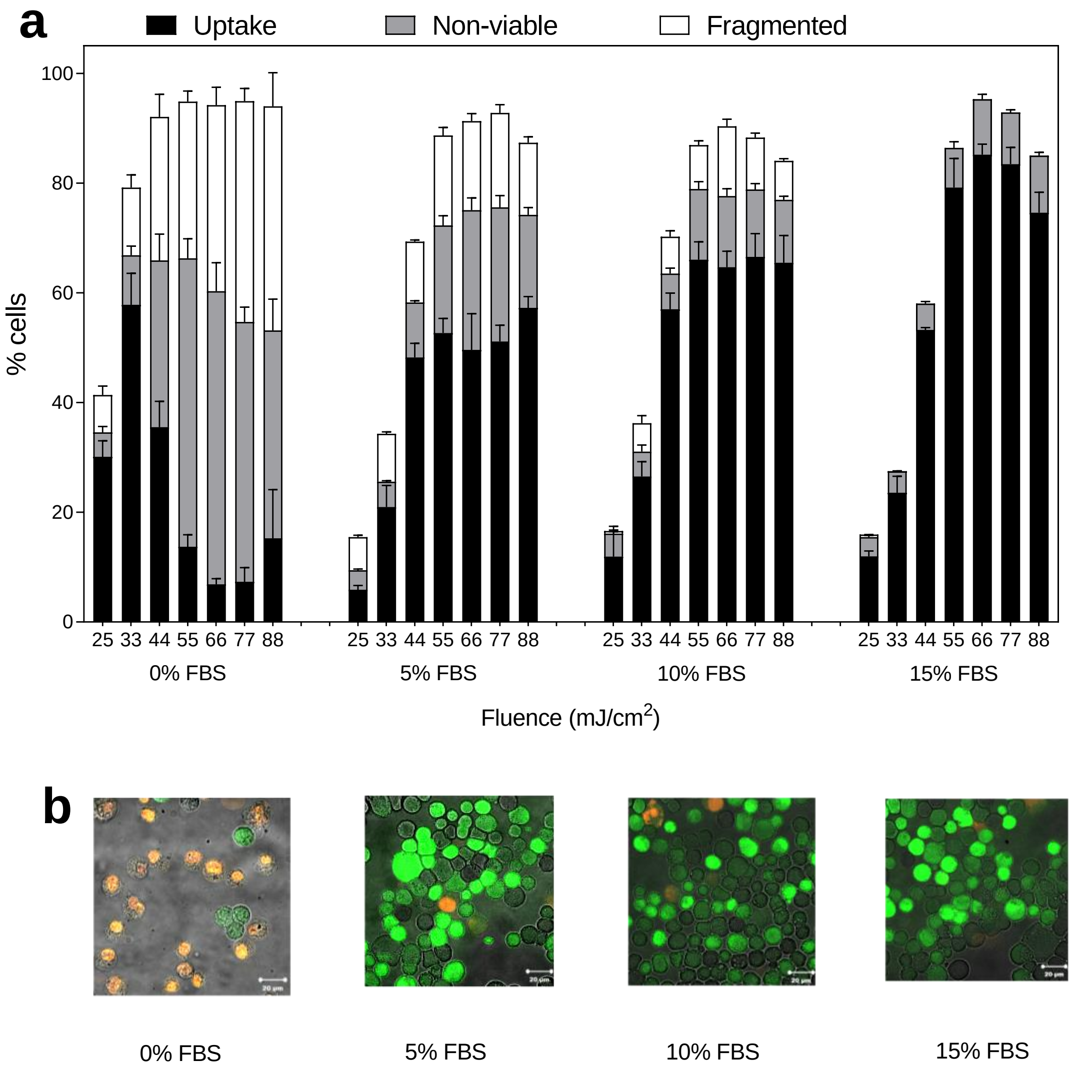

Figure 4.1: Changes in bio-effects due to presence of serum (FBS) in DU145 cell suspension media during laser exposure. (a) Distribution of uptake cells, non-viable cells and fragmented cells at various FBS concentrations, expressed as a volume percent of cell suspension media. The fluence in each case was varied from 25 mJ/cm^2 to 88 mJ/cm^2. All samples contained 26.3 mg/L CB nanoparticles and 10 µM calcein, and were exposed to laser pulses for 1 min. Data are expressed as mean ± SEM based on 3 replicates each. (b) Representative fluorescence microscopy images of DU145 cells exposed to laser at 55 mJ/cm^2 fluence, that were suspended in media containing varying FBS concentrations. Viable cells with molecular uptake are marked by the green fluorescence of calcein. Non-viable cells were stained by PI and exhibit orange (red and green combined) fluorescence. Images are each representative of 3 independent samples.

much as ~80% of cells with high cell viability.

For a given fluence above 25 mJ/cm^2, percentage of viable cells increased with increasing FBS concentration (one-way ANOVA, $p < 0.05$) and percentage of non-viable and fragmented cells decreased with increased FBS concentration to as little as ~10% non-viable cells with essentially no fragmented cells seen at the highest FBS concentration (two-way ANOVA, $p < 0.0001$ for both non-viable and fragmented cells) (Figure 4.1a). Additionally, for 15% FBS containing media, no significant differences are observed in percentage of viable cells across all fluence values tested (one-way ANOVA, $p > 0.05$). Therefore, it is notable that with increasing FBS concentrations, the distribution of cells among the possible cellular outcomes shifted, so that increasing FBS concentration resulted in more viable cells with uptake and fewer non-viable or fragmented cells. Thus, the higher percentage of cells showing calcein uptake appears to be caused by the reduction of cell viability loss due to the presence of FBS during laser exposure, i.e., cells that would have become non-viable without FBS, maintained their viability and were instead cells with uptake due to the protective effects of FBS.

We further found that the presence of serum in cell suspension media lowered the total bio-effects caused by photoporation (two-way ANOVA, $p < 0.05$ for each fluence) (Figure 4.1a). At lower fluence, this resulted in lower percentage of uptake, non-viable and fragmented cells in the presence of serum (two-way ANOVA, $p < 0.05$). However, when laser fluence was increased, viability loss due to photoporation decreased and percentage of cells with calcein uptake increased in presence of serum (two-way ANOVA, $p < 0.05$). At the highest fluence values (i.e., 55 – 88 mJ/cm^2), total bio-effects saturated at ~100% and there was no effect of serum concentration (one-way ANOVA, $p > 0.05$).

These findings come from flow cytometry analysis and can be qualitatively corroborated with fluorescence imaging of laser irradiated cells suspended in varying FBS concentrations, as shown in Figure 4.1b. With the increase in FBS concentration, two things become noticeable in laser irradiated samples: the number of non-viable cells (stained with PI, seen as orange in color) decreased and the number of viable cells with calcein uptake (seen as green in color) increased with increase in FBS concentration. These trends are similar to the results generated by flow cytometry analysis in Figure 4.1a.

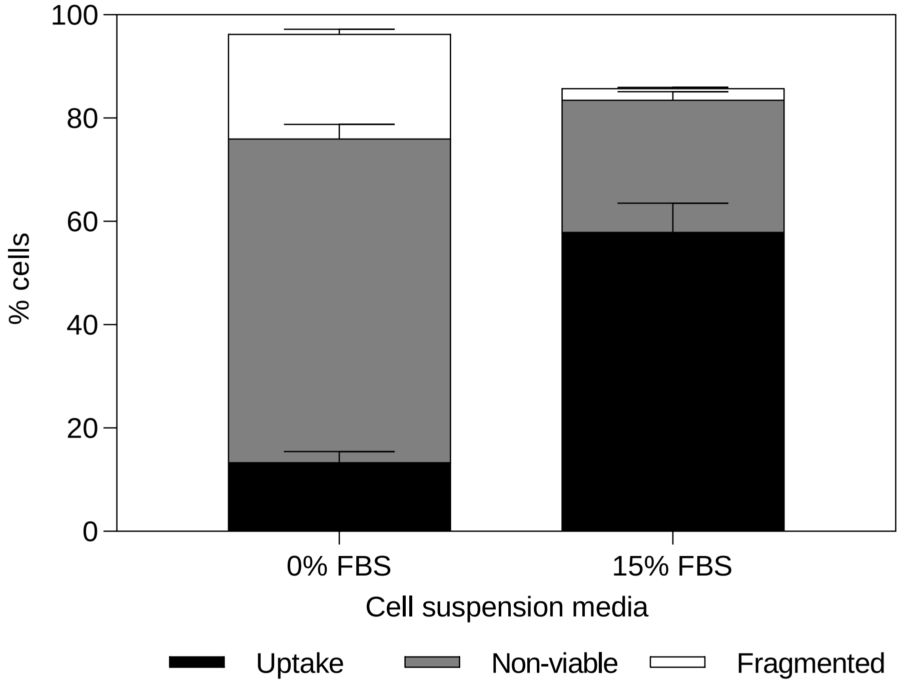

Figure 4.2: Changes in bio-effects due to presence of serum (FBS) in HDF cell suspension media during laser exposure. Distribution of uptake cells, non-viable cells and fragmented cells at 0% and 15% v/v FBS concentration. Laser exposure was carried out at a fluence of 88 mJ/cm^2 for 1 min. All samples contained 26.3 mg/L CB nanoparticles and 10 µM calcein. Data are expressed as mean ± SEM based on 3 replicates each.

To test the generality of these findings, we also checked whether the cell viability protection offered by FBS can be seen on a different cell type. HDF cells, suspended either in media containing no FBS or containing 15% v/v FBS, were exposed to laser at a fluence of 88 mJ/cm^2 in presence of CB nanoparticles and calcein. As shown in Figure 4.2, HDF cells suspended in FBS containing media had significantly higher percentage of viable cells with calcein uptake compared to HDF cells suspended in RPMI only ($p < 0.05$). This suggested that serum's ability to provide cell viability protection during photoporation was seen in this additional cell type.

4.3.2 Need for FBS presence during laser exposure for viability protection

To investigate whether presence of FBS was necessary during laser exposure to provide cell viability protection, 10% v/v FBS was added to the cell suspension at different times before or after laser exposure (Figure 4.3). We found that time of FBS addition significantly affected bio-effects (one-way ANOVA, $p < 0.0001$ for uptake, non-viable and fragmented). Almost 62 ± 1% of cells were viable and had calcein uptake when FBS was added immediately before laser exposure while only 20 ± 1% cells remained viable and had calcein uptake when FBS was added immediately after laser exposure (Tukey's multiple comparison tests, $p < 0.0001$). Similarly, 23 ± 4% cells were non-viable and 3 ± 1% cells were fragmented when FBS was added immediately before laser exposure while 57 ± 2% of cells were non-viable and 19 ± 1% of cells were fragmented (Tukey's multiple comparison tests, $p < 0.0001$) when FBS was added immediately after laser exposure. These data indicate that presence of FBS during laser exposure (i.e., during photoporation) was important for viability protection.

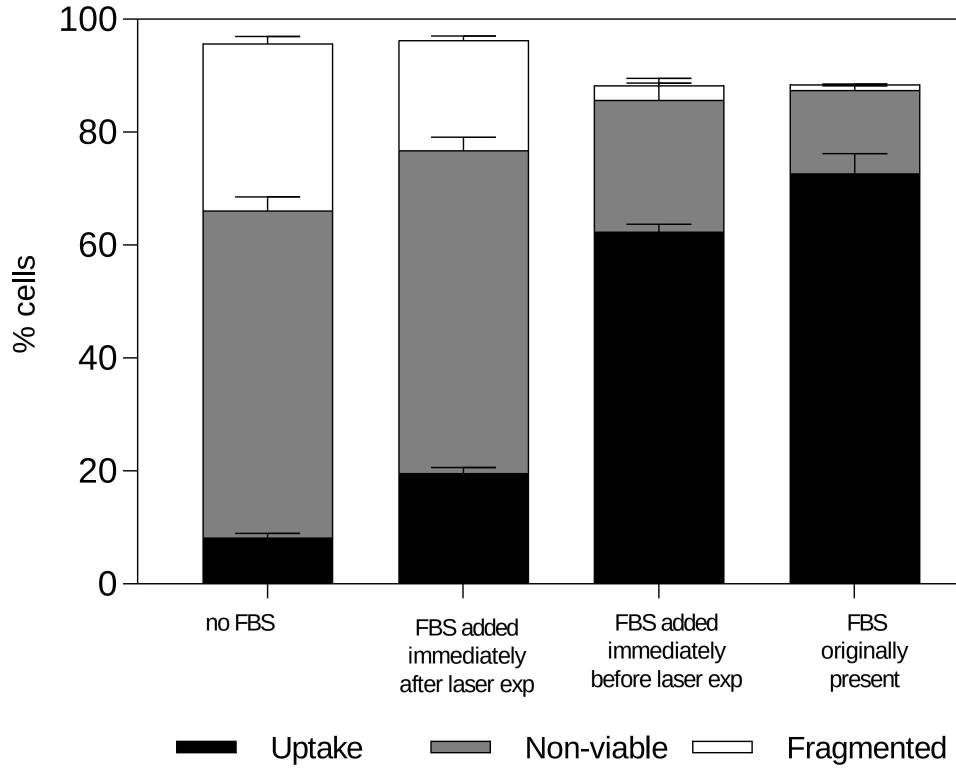

Figure 4.3: Changes in bio-effects due to addition of serum (FBS) to DU145 cell suspension media at different times before and after laser exposure. Distribution of uptake cells, non-viable cells and fragmented cells with 10% v/v FBS added at the beginning of the experiment > 60 min before laser, immediately before (<10 s) laser exposure or immediately after (<10 s) laser exposure. Laser exposure was carried out at a fluence of 88 mJ/cm^2 for 1 min. All samples contained 26.3 mg/L CB nanoparticles and 10 µM calcein. Data are expressed as mean ± SEM based on 3 replicates each.

The extent of viability protection offered by FBS when added immediately before laser exposure was not significantly different from the case where FBS was originally present in cell suspension media well before laser exposures (Tukey's multiple comparison test, $p > 0.05$ for both non-viable and fragmented cells). However, it is notable that FBS addition immediately after laser exposure offered some viability protection compared to the laser exposure protocol without FBS at all, since a higher percentage of cells had uptake

(Tukey's multiple comparison tests, $p < 0.0001$) and a lower percentage of cells were fragmented (Tukey's multiple comparison tests, $p < 0.0001$) compared to no FBS case.

4.3.3 FBS components responsible for viability protection

To identify the FBS components responsible for protecting cell viability during photoporation, FBS was size filtered using membranes with 5 kDa or 30 kDa molecular weight cutoffs. Figure 4.4 shows that bio-effects depended on molecular weight of the FBS components in cell suspension media (one-way ANOVA, $p < 0.0001$ for uptake, non-viable and fragmented cells). However, we see no significant differences between cells suspended in unaltered FBS (without the molecular size cutoff), FBS containing only compounds above a 5 kDa cut-off and FBS containing only compounds above a 30 kDa cut-off (Tukey's multiple comparisons test, $p > 0.05$). Additionally, no significant differences were seen between cells suspended without FBS, FBS containing only compounds below a 5 kDa cut-off and FBS containing only compounds below a 30 kDa cut-off (Tukey's multiple comparisons test, $p > 0.05$), and bio-effects from these conditions were all significantly different from bio-effects seen in three conditions with the high-molecular weight FBS components (Tukey's multiple comparisons test, $p < 0.05$).

Because only components of FBS greater than 30 kDa were needed to enable high uptake with high cell viability, we hypothesized that laser irradiation in the presence of albumin, which is the most abundant protein in serum and has a molecular weight of 66 kDa, would be as effective as full FBS. Because 10% v/v FBS contains 0.2% w/v albumin and 0.6% w/v total protein, we exposed cells to laser irradiation in the presence of 0.2%w/v and 0.6% w/v BSA, as well as 1% w/v BSA to further assess concentration dependence.

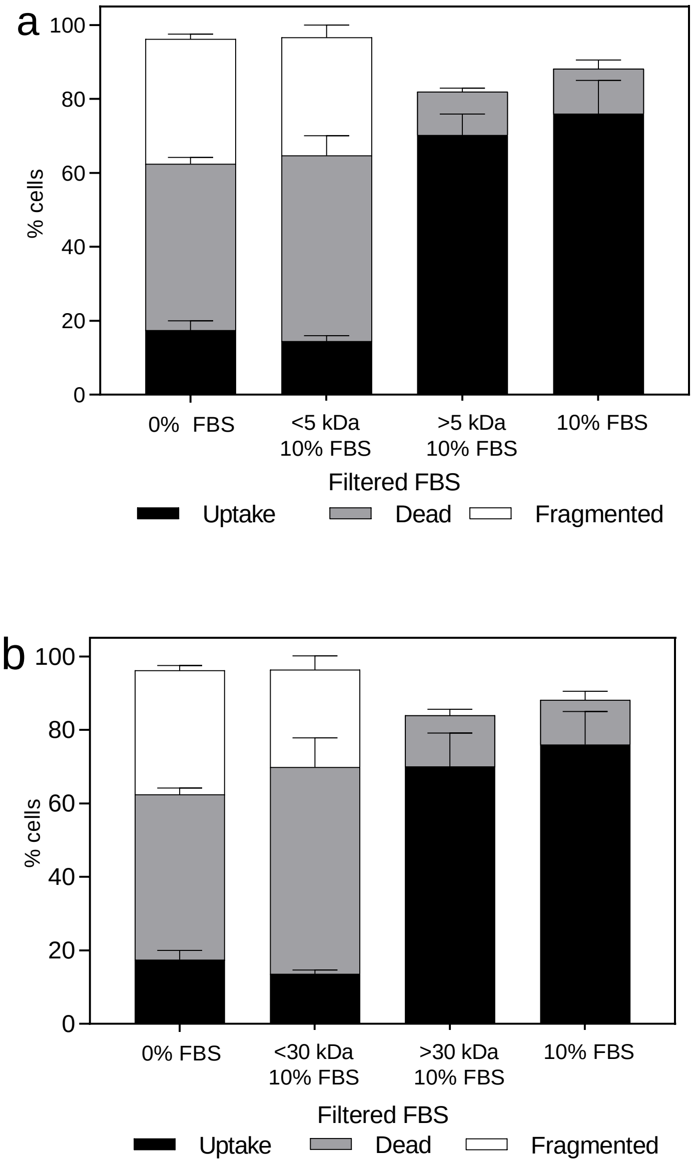

Figure 4.4: Changes in bio-effects due to addition of filtered serum (FBS) with different molecular weight cut-offs to DU145 cell suspension media during laser exposure. Distribution of uptake cells, non-viable cells and fragmented cells with 10% v/v FBS without alteration with fractions above or below a (a) 5 kDa or (b) 30 kDa molecular weight cut off. Laser exposure was carried out at a fluence of 55 mJ/cm^2 for 1 min. All samples contained 26.3 mg/L CB nanoparticles and 10 µM calcein. Data are expressed as mean ± SEM based on 3 replicates each.

We found that increasing BSA concentration led to an increase in percentage of cells with calcein uptake (one-way ANOVA, $p < 0.0001$) and caused decrease in non-viable and fragmented cells (one-way ANOVA, $p < 0.0001$), as seen in Figure 4.5a. While ~81 ± 4% of cells lost viability (non-viable and fragmented combined) when cells were exposed to laser without added protein, only ~53 ± 2% of cells lost viability when they were suspended in 0.2% BSA ($p < 0.0001$), ~39 ± 4% of cells lost viability when suspended in 0.6% BSA ($p < 0.0001$) and ~31 ± 1% of cells lost viability when suspended in 1% BSA ($p < 0.0001$). Although dependent on concentration, these data show that serum albumin alone was able to offer viability protection similar to full FBS.

To evaluate whether BSA is specifically needed or if other proteins can also offer similar protection, we exposed cells to laser irradiation on the presence of varying concentrations of HG. As shown in Figure 4.5b, adding HG during laser exposure resulted in significantly higher percentage of cells with calcein uptake compared to cells suspended in RPMI only (one-way ANOVA, $p < 0.0001$).The uptake and non-viable cell percentage did not appear to vary with increasing HG concentrations (one-way ANOVA, $p > 0.05$ for both uptake and non-viable cells). However, there was a significant difference in fragmented cells wherein, percentage of fragmented cells decreased with increasing HG concentrations (one-way ANOVA, $p < 0.001$). Altogether, these data suggest that the viability protection caused by FBS may be generally associated with proteins in FBS, and that other proteins including BSA and HG can be similarly protective.

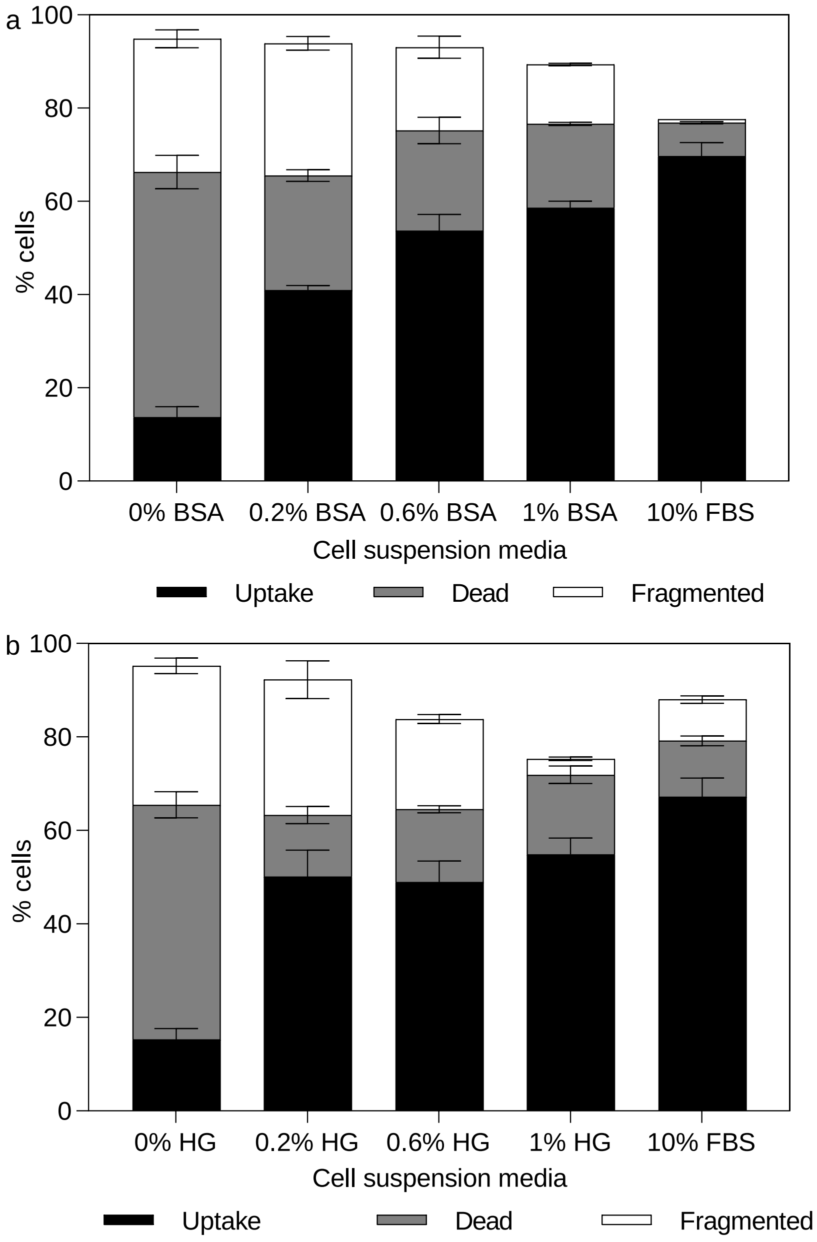

Figure 4.5: Changes in bio-effects due to addition of protein to DU145 cell suspension media during laser exposure. Distribution of uptake cells, non-viable cells and fragmented cells with 0.2% w/v, 0.6% w/v or 1% w/v (a) BSA or (b) HG. Laser exposure was carried out at a fluence of 55 mJ/cm^2 for 1 min. All samples contained 26.3 mg/L CB nanoparticles and 10 µM calcein. Data are expressed as mean ± SEM based on 3 replicates each.

4.3.4 Need for serum protein biological activity

To investigate whether the protective effects of serum are associated with protein biological activity, we conducted photoporation experiments with FBS proteins denatured through either heat or sonication. Bio-effects plotted in Figure 4.6 suggest that addition of denatured FBS proteins was able to significantly protect cells compared to RPMI only case (one-way ANOVA, $p < 0.0001$ for uptake, non-viable and fragmented cells). Additionally, no significant differences in bio-effects were seen among the two denatured FBS suspensions or compared to full FBS suspension (one-way ANOVA, $p > 0.05$ for uptake, non-viable and fragmented cells). These results show that serum protein biological activity was not needed to provide similar viability protection as full, biologically active FBS.

If protein biological activity is not needed, perhaps the increased viscosity of FBS could play a role. To check this, we added 0.1% carboxyl methylcellulose (CMC) in RPMI to match the viscosity of 10% FBS media (i.e., 1.28 ± 0.14 cP). However, bio-effects after laser exposure in the viscous RPMI were not significantly different compared to RPMI with 1 cP viscosity (Tukey’s multiple comparison tests, $p > 0.05$ for uptake, non-viable and fragmented cells) and resulted in significantly less uptake (Tukey’s multiple comparison tests, $p < 0.0001$) and more viability loss (Tukey’s multiple comparison tests, $p < 0.0001$) compared to laser exposure in FBS (Figure E.1 in Appendix). We also measured bulk temperature rise due to laser exposure during nanoparticle-mediated photoporation when different additives were mixed with cell suspension media to check if these additives affect the absorbance or energy dissipation properties of either nanoparticles or suspension media itself (Figure E.2 in Appendix). Although, one-way ANOVA gave a p value < 0.001, subsequent Tukey's multiple comparisons tests found no significant difference between any pair of additives or compared to RPMI only media ($p > 0.05$).

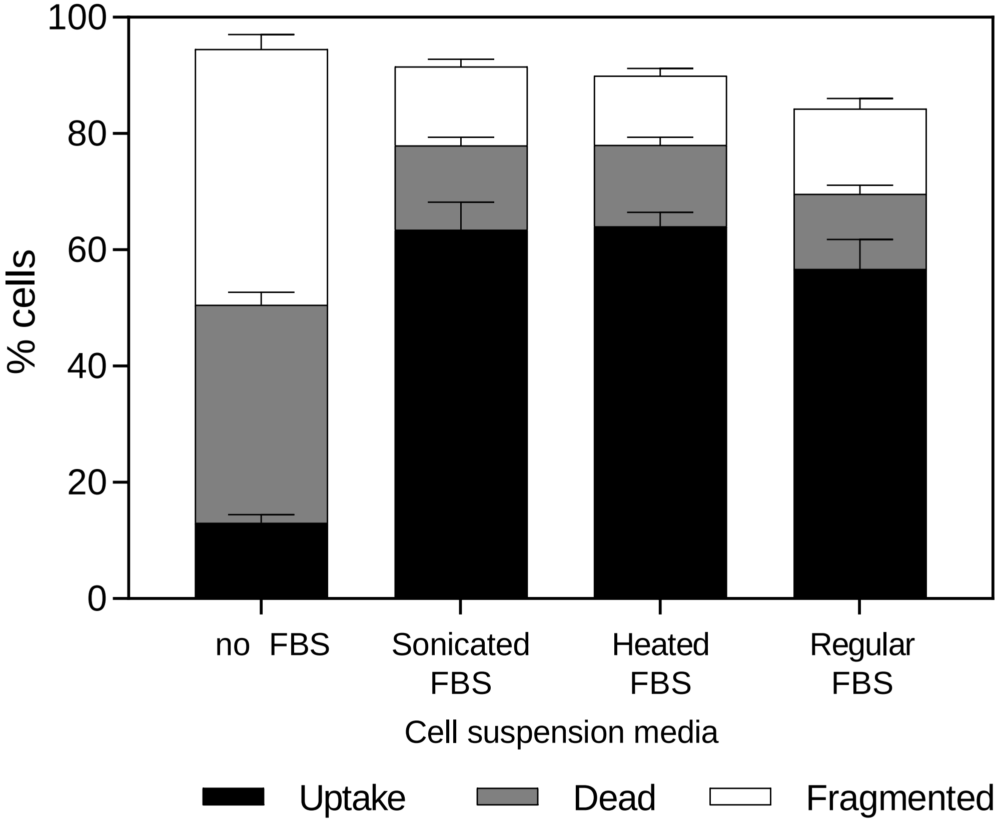

Figure 4.6: Changes in bio-effects due to addition of denatured BSA to DU145 cell suspension media during laser exposure. Distribution of uptake cells, non-viable cells and fragmented cells with BSA denatured by sonication or heat. Laser exposure was carried out at a fluence of 88 mJ/cm^2 for 1 min. All samples contained 26.3 mg/L CB nanoparticles and 10 µM calcein. Data are expressed as mean ± SEM based on 3 replicates each.

4.3.5 Viability protection offered by polymers

In prior studies, serum and serum proteins have been shown to protect cell viability against physical damage in agitated and/or aerated cell culture bioreactors[14,166]. The literature also suggests that polymers can provide similar viability protection[167].

Although stresses caused by photoporation are different from cell culture bioreactors fluid mechanics, we tested whether polymers seen in the bioreactor literature might provide protection in our studies.

To evaluate the effects of synthetic polymers on photoporation, cells were suspended in media containing up to 1% concentrations of polymers in RPMI,. Data in Figure 4.7 show that for PHPMA addition, percentage of uptake cells, nonviable cells and fragmented cells was not significantly different compared to samples with only RPMI (one-way ANOVA, $p > 0.05$). Addition of PEG increased percentage of uptake cells (one-way ANOVA, $p < 0.01$) and decreased percentage of non-viable cells (one-way ANOVA, $p < 0.01$) with increasing PEG concentration. However, even at the highest PEG concentration (1% w/v), uptake was lower (Tukey's multiple comparison tests, $p < 0.0001$) and viability loss was higher compared to 10% FBS (Tukey's multiple comparison tests, $p < 0.001$).

Laser exposure with PVP, PEOX or F127 exhibited increased percentage of cells with uptake (Tukey's multiple comparisons test, $p < 0.0001$)) and decreased loss of viability (Tukey's multiple comparisons test, $p < 0.001$) compared to exposure with RPMI alone. Only PVP showed a dependence of percentage of cells with uptake (one-way ANOVA, $p < 0.0001$) and viability loss (one-way ANOVA, $p < 0.001$) with increasing polymer concentration. All three polymers achieved uptake levels that were similar to (Tukey's multiple comparisons test, $p > 0.05$ for PEOX) or greater than 5% FBS (Tukey's multiple comparisons test, $p < 0.05$ for PVP and F127)) and, in some cases (i.e., PVP, F127) comparable to 10% or 15% FBS (Tukey's multiple comparisons test, $p > 0.05$ for 0.6% and 1% PVP and F127). We conclude that synthetic polymers were able to provide comparatively enhanced cell viability protection compared to RPMI during photoporation, although all polymers did not perform equally well.

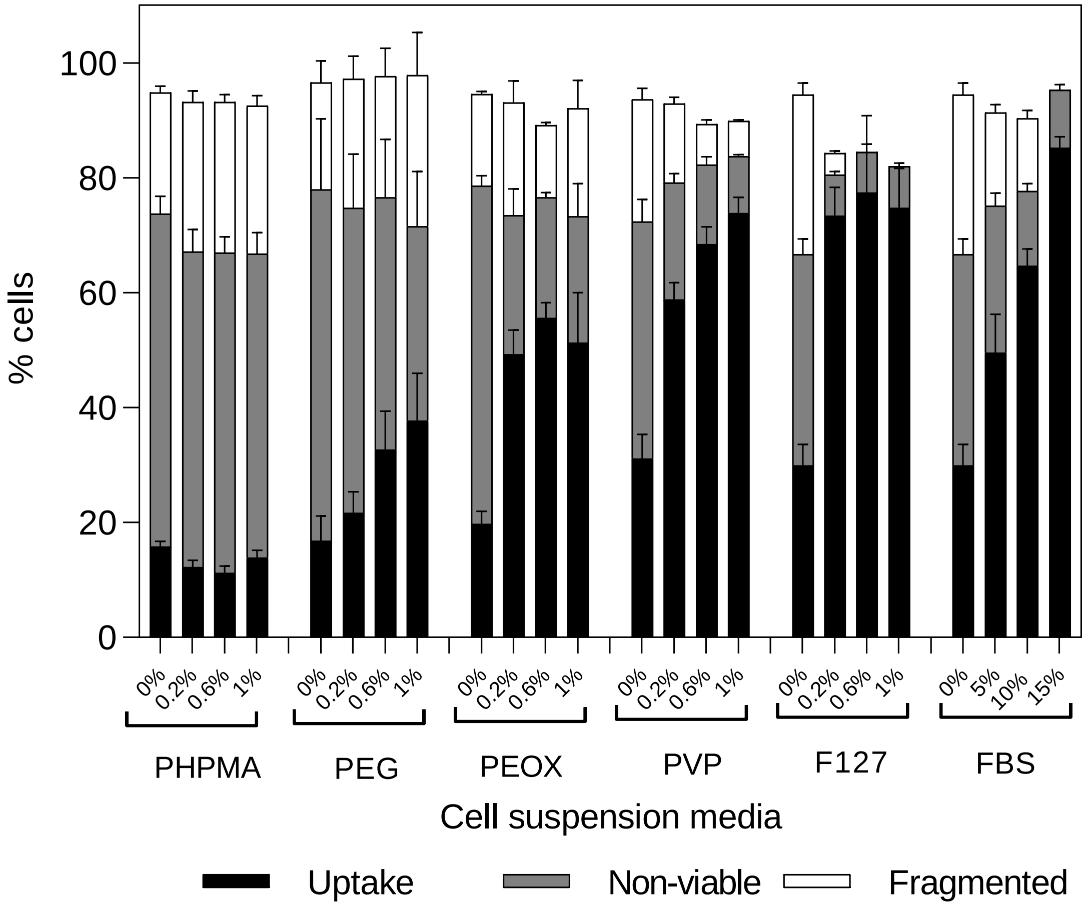

Figure 4.7: Changes in bio-effects due to addition of synthetic polymers to DU145 cell suspension media during laser exposure. Distribution of uptake cells, non-viable cells and fragmented cells with PHPMA, PEG, PVP, PEOX and F127 at different concentrations (w/v) compared to FBS at different concentrations (v/v). Laser exposure was carried out at a fluence of 55 mJ/cm^2 for 1 min. All samples contained 26.3 mg/L CB nanoparticles and 10 µM calcein. Data are expressed as mean ± SEM based on 3 replicates each.

4.3.6 Polymer properties governing viability protection performance

Polymers used in this study were chosen on the basis of being non-toxic to cells and general acceptance in prior studies of cell protection during mechanical insult. However, these polymers have varying properties and their ability to protect cell viability also varied, as shown in Figure 4.7. We hypothesized that the physical interactions between polymers (and proteins) and the cell membrane were responsible for viability protection, since intracellular uptake, as well as loss of cell viability, are believed to be caused during photoporation due to creation of transient pores in the cell membrane. Given that the creation of aqueous pores across the cell membrane pores requires creation of a hydrophilic pathway across the hydrophobic core of the cell membrane[168], we explored the possibility of hydrophobic interactions between the polymer and the cell membrane being dominant force that lead to accelerated cell repair and cell viability protection.

We characterized polymer hydrophobicity on the basis of contact angle with water. Figure 4.8 shows bio-effects plotted against contact angle of each of the polymers used. We found that for each polymer concentration, percentage of uptake cells increased (one-way ANOVA, $p < 0.0001$) and percentage of nonviable cells decreased (one-way ANOVA, $p < 0.0001$) with increasing polymer contact angle. This correlation is consistent with our hypothesis that hydrophobic interactions are important to the protective effect of polymers on cells during photoporation.

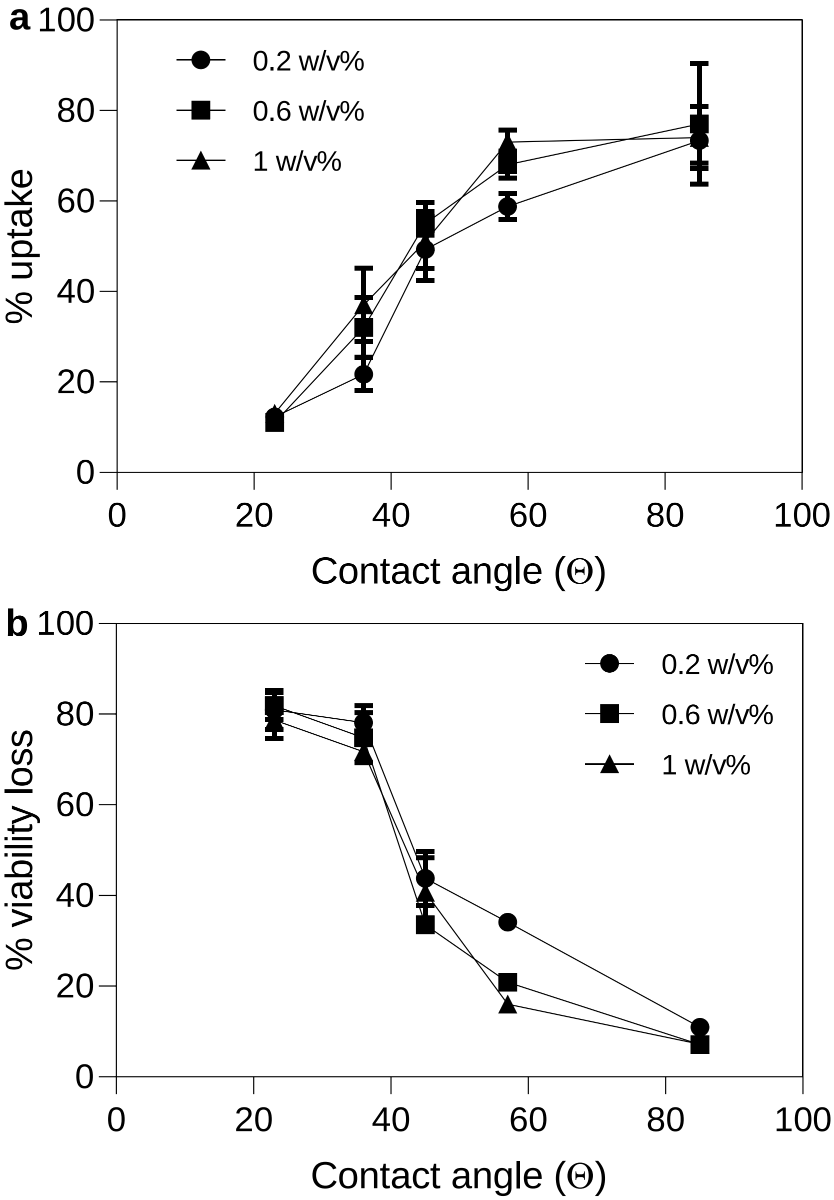

Figure 4.8: Changes in bio-effects as a function of polymer contact angle after laser exposure of DU145 cell suspension. Percentage of (a) uptake cells and (b) non-viable+fragmented cells with different polymer having different contact angles: 23º for PHPMA, 36º for PEG, 45º for PEOX, 57º for PVP and 85º for Pluronic F127[169]. The bio-effects data are the same as in Figure 4.7. Laser exposure was carried out at a fluence of 55 mJ/cm^2 for 1 min. All samples contained 26.3 mg/L CB nanoparticles and 10 µM calcein. Data are expressed as mean ± SEM based on 3 replicates each.

Polymers such as PEG, have previously been shown to offer viability protection against fluid-mechanical damage in bioreactors[170,171], allow faster cell growth[172], and offer cell wound healing as a trauma therapeutic[173]. In addition, higher molecular weight PEG has been shown to offer better cell growth in suspension media[172]. We therefore studied the effect of molecular weight of PEG, as well as PVP on bio-effects.

As seen in Figure 4.9, increasing molecular weight increased percentage of viable cells with calcein uptake (one-way ANOVA, $p < 0.0001$) while it decreased percentage of non-viable and fragmented cells (one-way ANOVA, $p < 0.0001$). For cells suspended in 10 kDa PEG, ~21 ± 2% were uptake cells while ~70 ± 5% cells lost viability. In comparison, cells suspended in 600 kDa PEG behaved significantly differently, with ~63 ± 4% of cells showing uptake (Tukey's multiple comparisons test, $p < 0.0001$) while ~29 ± 2% of cells lost viability (Tukey's multiple comparisons test, $p < 0.0001$).

Therefore, above results suggest that PEG molecular weight plays an important role in determining its ability to provide viability protection during photoporation. A similar trend for varying molecular weight of PVP present in cell suspension media during photoporation was observed as well. Bio-effects plot in Figure 4.9 showed that with increasing molecular weight of PVP in cell suspension media, percentage of viable cells with calcein uptake increased (one-way ANOVA, $p < 0.0001$) while percentage of non-viable and fragmented cells, represented as viability loss had decreased (one-way ANOVA, $p < 0.05$). Hence, the viability protection ability of both polymer additives appears to be dependent on their molecular weights.

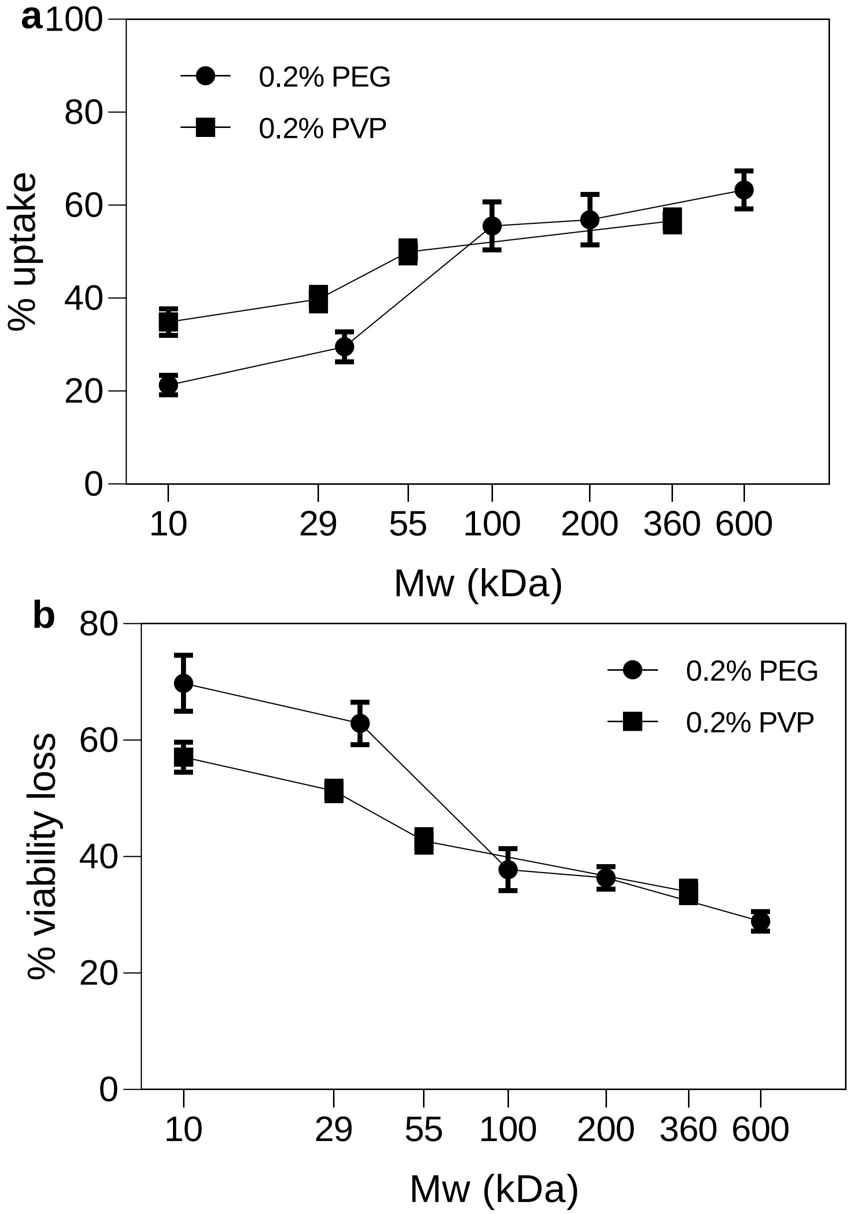

Figure 4.9: Changes in bio-effects as a function of polymer molecular weight after laser exposure of DU145 cell suspension. Percentage of (a) uptake cells and (b) non-viable+fragmented cells with different polymer having different contact angles: 0.2 w/v% 10 kDa, 35 kDa, 100 kDa, 200 kDa and 600 kDa PEG; and 10 kDa, 29 kDa, 55 kDa and 360 kDa PVP. Laser exposure was carried out at a fluence of 55 mJ/cm^2 for 1 min. All samples contained 26.3 mg/L CB nanoparticles and 10 µM calcein. Data are expressed as mean ± SEM based on 3 replicates each.

4.4 Discussion

In this chapter, we have explored the effects of FBS addition in cell suspension media during nanoparticle-mediated photoporation for fluorescent calcein delivery into DU145 cells. Photoporation can cause three different bio-effects – uptake of calcein into viable cells (uptake cells), viability loss due to poration (non-viable cells) and viability loss due to fragmentation (fragmented cells). When cells were exposed to high laser fluence during photoporation, significant viability loss occurred due to cell death and fragmentation. Data in Figure 4.1 showed that lower fluence caused less viability loss, which then increased with increase in laser fluence. Similar result has previously been observed in studies aimed at understanding the effects of changing photoporation parameters[9].

However, when FBS was present in the cell suspension media during photoporation, either total bio-effects become lower at low fluence, compared to no FBS case or, total viability loss became lowered at high fluence resulting in higher percentage of viable cells with calcein uptake, compared to no FBS case. Although this was true for all three concentrations of FBS tested in the current study, increasing FBS concentrations resulted in greater viability protection. Previous studies have also shown FBS concentration dependent viability protection and faster growth of mammalian cells in agitated and aerated bioreactors[14,167]. In these studies, however, FBS was added to protect cells against fluid-mechanical damage caused by shear and bubble breakup. Therefore, the mechanism for viability protection could be different than in photoporation. We found that FBS can protect HDF cell viability as well during photoporation and thus, this feature is not exclusive to a single cell type. It was also shown that FBS is needed to be present in cell suspension media when cells get exposed to laser pulses and pores are formed, to provide viability protection. This observation suggests that the presence of FBS is essential during cell membrane pore formation to lower the viability loss.

FBS contains many proteins, hormones, enzymes, electrolytes, carbohydrates, and other compounds[174]. These components vary in concentration and size as well. To check for the components that might be responsible for providing viability protection, we size filtered the FBS before adding in cell suspension media. Photoporation experiments showed that components greater than 5 kDa and 30 kDa in size showed similar viability protection as seen in full FBS containing media. We hypothesized that the albumin (66 kDa) molecules present in FBS, were responsible for viability protection. Data collected from experiments, done with BSA present in cell suspension media during photoporation, were seen to be consistent with this hypothesis. Moreover, we discovered that viability protection ability was not exclusive to BSA proteins, since HG proteins were also able to protect cell viability during photoporation.

Albumin has been shown to have favorable bio-chemical interactions with cell membrane thereby increasing drug delivery efficiency in prior studies[175]. Our studies also show increased delivery efficiency due to FBS and BSA addition, but these increments were caused by decrease in viability loss. However, comparable delivery enhancement and viability protection were seen, even when FBS proteins were denatured using heat and sonication. Denaturing proteins should dampen their biological activity and thus reduce the bio-chemical interactions between protein molecules and cell membrane during pore formation. Therefore, above results suggested that viability protection offered by FBS might be caused by physical interactions between FBS protein and cells. A physical mechanism was reported to be the reason behind cell viability protection caused by serum addition in bioreactors[161]. These were shown to be caused by changes in cell suspension media properties such as viscosity[176]. However, increase in cell suspension media viscosity by adding CMC failed to improve cell viability or calcein uptake in our studies. Adding FBS did increase cell suspension media viscosity although that did not appear to help protect cell viability during photoporation.

Following the result that viability protection offered by FBS during photoporation might be due to physical interaction between FBS proteins and cells, we explored if this behavior can also be seen with polymer additives. We chose neutral and water-soluble polymers, some of which had already been used in cell culture bioreactors, as viability protection additives. Of the five polymers investigated, PEG, PVP, PEOX and Pluronic F127 showed greater viability protection during photoporation when compared to PHPMA. However, the extent of viability protection was observed to be different for different polymers. For example, for 0.6 w/v% polymer addition in cell suspension media, percentage of uptake cells were ~33 ± 7% for PEG addition, while, in comparison, percentage of uptake cells were ~56 ± 3% for PEOX, ~69 ± 3% for PVP and ~77 ± 13% for F127 addition.

Several factors could be responsible for this variability in viability protection. When cell membranes are porated, hydrophobic parts of the lipid bilayer can be exposed, introducing thermodynamic and biological instability[173]. Therefore, we hypothesized that polymers that have hydrophobic components can favorably associate with exposed hydrophobic lipid parts and help in accelerated resealing of the pore opening. We used water contact angle as a measure of hydrophobicity and found that percentage of uptake cells increased with increasing contact angle and percentage of viability loss decreased.

Polymers with higher contact angle had higher hydrophobicity and therefore, these results support the above hypothesis. It is important to note that all these polymers are considered hydrophilic since they are water soluble. However, each of these polymers can act as amphiphilic with both hydrophilic and hydrophobic components present in the molecular structure.

Pluronic F127 is a triblock, non-ionic surfactant with hydrophobic polypropylene glycol (PPG) part bound to hydrophilic PEG chains on each side. This amphiphilic feature allows Pluronic F127 to associate with exposed hydrophobic parts of porated cell membrane and lower the risk of downstream damages to ionic balances and subcellular components[173]. A similar analysis can be made for other polymers (PEG, PEOX and PVP), although without neat separation between hydrophobic and hydrophobic parts. For these polymers, a close relative can be polysoaps that have repeating units of intrinsic amphiphilic monomers[177]. Therefore, increasing molecular weight can raise the chances of favorable association with exposed lipid hydrophobic parts. This is supported by our results that showed higher percentage of uptake cells and lower viability loss with increasing molecular weights of PEG and PVP.

In addition, increasing molecular weight also increases hydrodynamic radius of polymers. For example, PEG hydrodynamic radius varies from 2.8 nm for 10 kDa to 29.9 nm for 600 kDa[178]. Given the larger size of higher molecular weight polymers, they might find it easier to span and thereby seal the cell membrane pore opening, which should work synergistically with greater number of hydrophobic sites to provide accelerated cell repair.

For decades, polymers have garnered attention for their ability to prevent cell viability loss in bioreactors caused by fluid mechanical damages[167]. Polymers have been extensively used as cell growth accelerator[172] and proliferator[179]. In addition, they have been also been used as membrane sealants to aide in repair and regeneration of damaged cell membrane[173,180]. PEG, PVP and Pluronics have found themselves amidst FBS and BSA for almost all these applications[181]. But the exact mechanism of viability protection for each of these additives dependent on the molecules used[170,176,182] and are still under investigation. The most current mechanism hypothesizes that these additives enhance cell repair by either directly sealing the membrane pores or indirectly assisting to do so[173,180,183] though favorable hydrophobic interactions is supported by data shown in our results. Presence of hydrophobic sites in BSA molecules (native and denatured) adds to the proposed mechanism of viability protection.

4.5 Conclusion

Nanoparticle-mediated photoporation can be used for intracellular delivery of molecules in biotechnology, diagnostic and therapeutic applications. This physical route of creating transient cell membrane pore often encounters trade-off between delivery and viability loss. Through this study, we showed that FBS can lower cell viability loss at high laser fluence. Specifically, in some cases, percentage of viable cells increased from less than 25% to greater than 80% only by the addition of FBS, which allowed use of more aggressive photoporation conditions that helped in significantly increasing the percentage of viable cells with molecular uptake. This cell viability protection behavior was shown to be caused by physical interactions introduced by serum proteins. Further, certain polymer additives were also shown to provide protection against cell viability loss, which were shown to be affected by their hydrophobic interactions with exposed cell membrane pores. In conclusion, nanoparticle-mediated photoporation can be more efficiently used to deliver molecules intracellularly when cells are suspended in media containing serum or certain polymer additives during laser exposure.

CHAPTER 5. OPTIMIZATION OF INTRACELLULAR MACROMOLECULE DELIVERY BY NANOPARTICLE-MEDIATED PHOTOPORATION

5.1 Introduction

High molecular weight biomolecules such as proteins, peptides, and nucleic acids have found usage in latest advancements of medical applications such as cellular imaging, diagnostics and therapies. Molecules such as DNA, RNA can be delivered inside cells to perform wide variety of applications including gene expression study [184,185], and gene therapy[186,187]. Similarly, proteins and peptides can be delivered to intracellular targets for imaging[188,189] and disease treatment[190]. For example, i*n vivo* protein therapy has been used to replace compromised macromolecules inside cell, while avoiding the complications of gene therapy[191,192]. But the presence of cell membrane restricts the delivery of these macromolecules[193]. Several researchers use the slow and passive diffusion-controlled endocytic route[194,195] to enable the uptake of macromolecules by cells. However, endosomal entrapment and pH changes[153] can sometimes render these molecules inactive or less effective[196,197].

Consequentially, alternative routes have also been explored to overcome this physical barrier by employing biological (e.g. viral vectors[4,198]), chemical (e.g. polymeric and particulate formulation[155]) and physical (e.g. microinjection[84], sonoporation[199] and electroporation[140]) methods to enable molecular delivery into cells. However, the issues related to cytotoxicity, immunogenicity, off-target specificity and restricted application[4,5] has still limited use of these methods.

Recently, nanoparticle-mediated photoporation was introduced as a platform technology to deliver molecules inside cells[6,146,200]. This method uses photoacoustic and thermal output of nanoparticles, when irradiated with 1064 nm wavelength near infrared (NIR) pulsed laser beam, to create transient membrane pores enabling intracellular delivery[12]. This method was optimized for delivery of low molecular weight calcein (0.66 kDa) molecules resulting in greater than 90% cells with uptake with minimal viability loss[12]. Further, EGFR mRNA knockdown[11] and EGFP silencing[201] was achieved by delivering anti-EGFR and anti-EGFP siRNA into Human cells using nanoparticle-mediated photoporation, although using different nanoparticle and delivery route.

However, majority of the molecules delivered efficiently were lower than 15 kDa in size. Experiments aimed at delivering molecules bigger than 100 kDa, such as plasmid DNA resulted in very low delivery efficiency[6,12]. Therefore, through this study, we examine the feasibility of nanoparticle-mediated photoporation to deliver wide range of macromolecules and provide laser exposure conditions to improve delivery efficiency of macromolecules with molecular weight ranging from 4 kDa to 2,000 kDa. Previous studies have suggested that macromolecular delivery might be restricted by pore size and molecular diffusion time[12]. We hypothesized that we can enhance macromolecular delivery efficiency by increasing the size of cell membrane pores and time available for macromolecule diffusion to and across cell membrane pores.

5.2 Material and methods

5.2.1 Cell preparation

DU145 human prostate cancer cells (American Type Culture Collection, CITY VA) were grown with cell media containing RPMI 1640 (Cellgro, Herndon, VA), 10% v/v FBS (Corning, Palo Alto, CA) and 1% P/S (Cellgro). The cells were incubated in tissue culture flasks at 37°C, 98% relative humidity and 5% CO_2 for growth. At 85% confluency, cells were harvested using 0.25% Trypsin/EDTA (Cellgro), after which, the cells were suspended at a concentration of 10^6 cells/ml in RPMI.

5.2.2 Nanoparticle dispersion preparation

25 nm CB powder (Black pearls 470, Cabot, Boston, MA), at a concentration of 400 mg/L, were used to prepare CB nanoparticle dispersion in DI water, which contained 0.013% (v/v) Tween-80 (Sigma-Aldrich, St. Louis, MO) solution stability enhancement (prevent particle aggregation for a homogeneous dispersion). The dispersion was sonicated for 35 min in an ultrasonic water bath (FS3OH, Fisher Scientific, Pittsburg, PA) followed by sonication with ultrasonic needle for 1 min (Sonics Ultracell, Sonics & Materials, Newton, CT). The final CB nanoparticle dispersions had aggregate diameter of 195 nm , which was measured using dynamic light scattering (DLS) measurements (ZetaSizer Nano, Malvern Instruments, Malvern, UK).

5.2.3 Sample preparation for laser exposure

520 μL of DU145 cells (10^6/mL) suspended in RPMI were mixed with 37 μL of 400 mg/L CB nanoparticle dispersion and 5.5 μL of 10 g/L FITC-labelled dextran (Sigma-

Aldrich, St. Louis, MO) solution in a 1.5 mL Eppendorf tube, to be used as exposure samples. The final CB nanoparticle concentration was calculated to be 26.3 mg/L while dextran concentration was calculated to be 98 mg/L. Samples were placed in ice bath to reduce endocytosis/cellular activity before and after-laser exposure.

5.2.4 Laser exposure and cell wash

Cell suspension containing CB nanoparticles and delivery molecules were transferred to a 2 mm wide and 21 mm diameter cylindrical Pyrex glass cuvette (37-PX-2, Starna Cells, Atascadero, CA). An Nd:YAG solid-state laser (Continuum Powerlite II Plus, Continuum, San Jose, CA) working at a frequency of 10 Hz, was used to apply 5-9 ns laser pulses of 1064 nm wavelength for 1 - 10 min. Laser fluence was varied between 25 and 88 mJ/cm^2. Samples were exposed to laser beam that irradiated the whole surface with uniform energy profile. Subsequently, samples were transferred back to the Eppendorf tubes and placed in ice. ‘Sham’ exposures with samples containing cells, CB nanoparticles, and dextran or calcein were used as negative controls that experienced the same handling and procedures except laser irradiation. After laser-irradiation, non-viable cells were labeled with 13.4 μM propidium iodide (PI, Invitrogen, Grand Island, NY) and incubated for 10 min on ice. Cell samples were then washed 3 times with phosphate buffer saline (PBS) after centrifugation at 500 g, to remove excess dextran or calcein from the bulk solution before flow cytometer or microscopic analyses.

5.2.5 Data collection

A bench-top flow cytometer (BD Accuri, BD Biosciences, San Jose, CA) was used to quantify bio-effects in terms of cell viability (based on red fluorescence of PI) and intracellular uptake (based on green fluorescence of calcein or FITC tagged dextran). Green fluorescence was measured using 530/28 nm bandpass filter with excitation at 488 nm and red PI fluorescence was measured using a 670 nm longpass filter with excitation at 535 nm. Cell samples were analyzed at 35 μL/min flow rate for 1 min. Cells with green fluorescence greater than in sham exposure cells with calcein and PI but not exposed to laser irradiation were considered to have intracellular uptake. Cells with red fluorescence of PI greater than in sham cells were marked as non-viable.

Samples with only cells in RPMI were used as negative control, to construct a cell population gate in the forward-scattered (FSC) and side-scattered (SSC) analysis, and were marked as intact cells. Possible cell loss due to cell fragmentation (appearing as low forward scatter and low side scatter events on the flow cytometer) were accounted for by taking the difference between number of viable cells detected in a given sample and number of viable cells detected in sham samples, and were marked as fragmented cells.

5.2.6 Data analysis

A minimum of 3 replicates were used for each experiment. Mean and standard error of the mean (SEM) were calculated using the 3 replicates. Analysis of variance (ANOVA, $\alpha = 0.05$) was performed to compare 3 or more experimental conditions using Graphpad Prism 8 (GraphPad Software, La Jolla, CA) followed by post-hoc Tukey's pairwise comparison. Statistical significance was marked by a p value < 0.05.

5.3 Results

5.3.1 Initial studies of intracellular macromolecule delivery by nanoparticle-mediated photoporation

Previous studies have optimized delivery of a small molecule (i.e., calcein (0.66 kDa)) to ~90% of cells with no significant viability loss[9,12]. To assess the effect of molecular weight on the delivery efficiency of larger macromolecules using nanoparticle-mediated photoporation, DU145 cells were suspended with six different FITC-labeled dextran molecules of 4 kDa, 10 kDa, 40 kDa, 150 kDa, 500 kDa and 2000 kDa molecular weight and exposed to laser conditions previously found to be favorable for intracellular delivery of calcein [9].

Flow cytometry analysis identified four types of cells after laser exposure: cells which were viable and had no uptake of molecules; cells which were viable and had successful uptake of fluorescent molecules (uptake cells); non-viable cells which did not recover from poration (non-viable cells, indicated by PI staining); and cells which were lost due to fragmentation (fragmented cells).

We hypothesized that delivery efficiency of molecules will be dependent on their molecular weight. Figure 5.1 shows number of intact and viable cells plotted against FITC fluorescence intensity for calcein and 4 kDa – 2000 kDa dextran delivery, obtained after flow cytometer analysis. Histograms show cells that were not exposed to laser pulses and exhibited only background fluorescence ("no laser" in Figure 5.1). In contrast, cells that were exposed to laser pulses at 33 mJ/cm^2 fluence for 1 min exhibited varying levels of intracellular uptake ("with laser" in Figure 5.1).

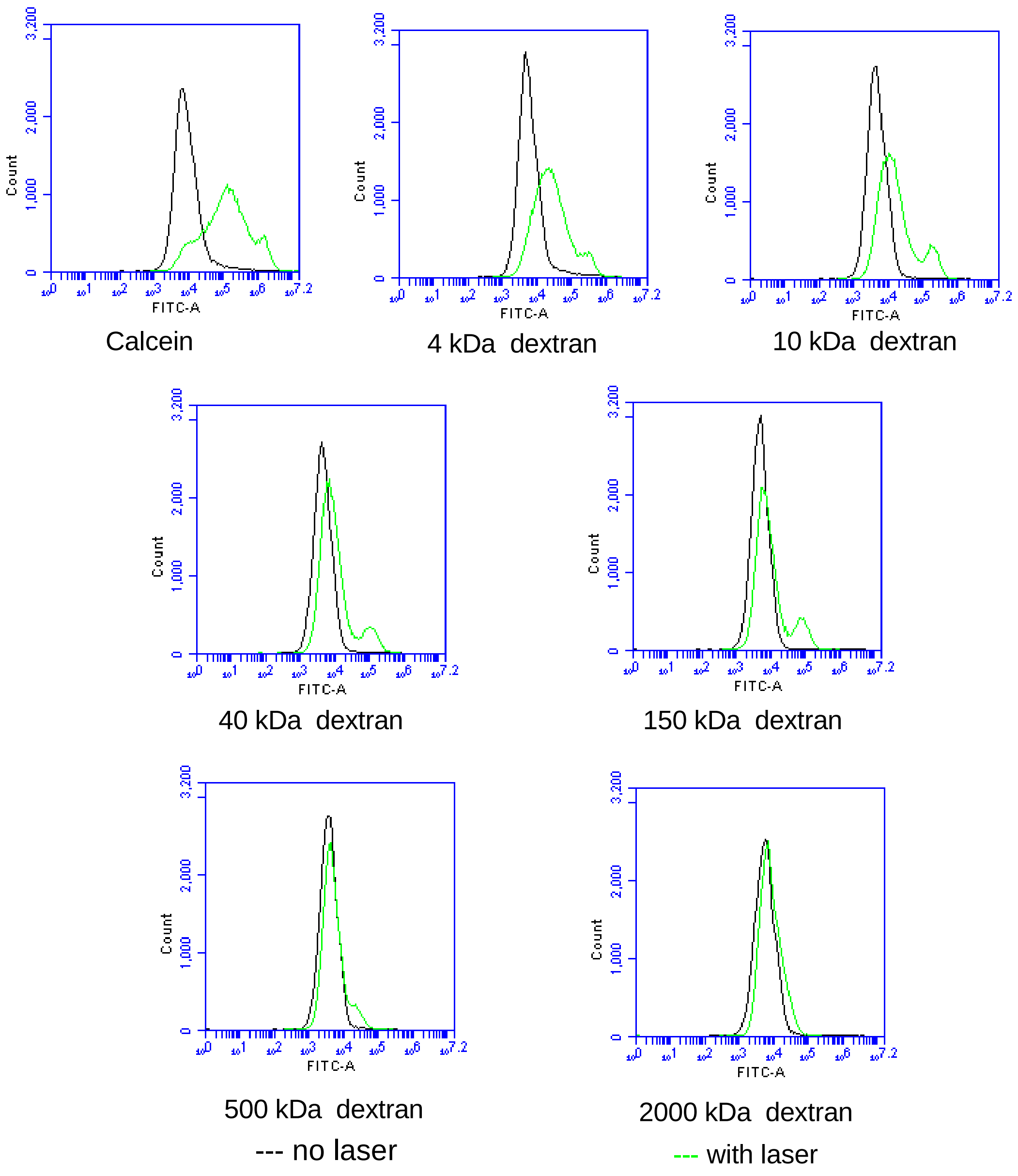

Calcein

4 kDa dextran

10 kDa dextran

40 kDa dextran

150 kDa dextran

500 kDa dextran

2000 kDa dextran

--- no laser

--- with laser

Figure 5.1: Representative flow cytometer histograms showing green (FITC) fluorescence intensity versus cell count plot after photoporation-mediated delivery of calcein and dextran (of molecular weights between 4 kDa and 2,000 kDa). "--- no laser" plots have viable cells that were not exposed to laser pulses and were used as negative control, while "---with laser" plots have viable cells that were exposed to laser pulses at 33 mJ/cm^2 fluence for 1 min, and exhibit increased fluorescence corresponding to uptake of molecules. These histograms are each representative of 3 independent replicate samples

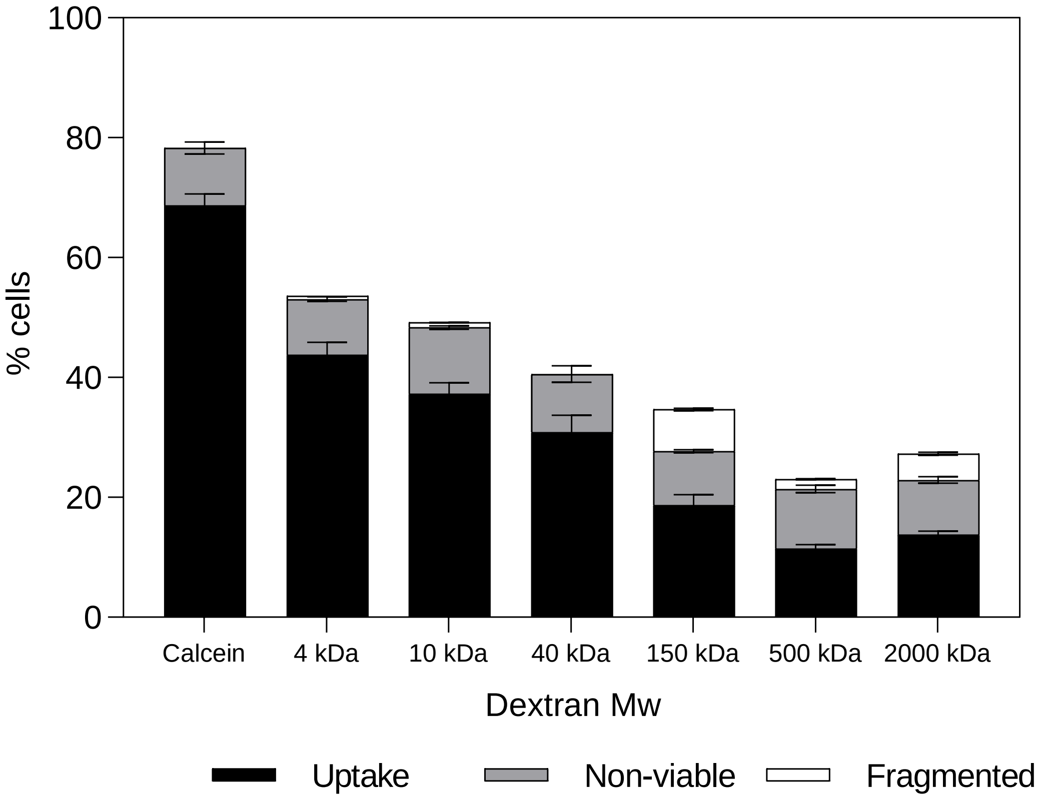

Figure 5.2: Changes in bio-effects as a function of molecular weight of the delivery molecule after laser exposure of DU145 cell suspension. Distribution of uptake cells, non-viable cells and fragmented cells is shown after laser exposure at a fluence of 33 mJ/cm^2 for 1 min. All samples contained 26.3 mg/L CB nanoparticles and 98 mg/L of the uptake molecule: calcein or dextran with molecular weight ranging from 4 kDa to 2,000 kDa. Data are expressed as mean ± SEM based on 3 replicates each.

Corresponding bio-effects plot in Figure 5.2 shows that ~69 ± 2% cells had calcein uptake due to photoporation. At same exposure condition, percentage of uptake cells for dextran delivery decreased with increase in molecular weight (one-way ANOVA, $p < 0.0001$). Only ~14 ± 1% cells showed 2000 kDa dextran uptake, which is significantly lower than calcein uptake (Tukey's multiple comparisons test, $p < 0.0001$). Due to lowering of uptake cells, the percentage of total bio-effects also decreased with increasing molecular weight (one -way ANOVA, $p < 0.0001$).

Increasing molecular weight of dextran molecules also increases their effective hydrodynamic radius and decreases their diffusivity[202]. As shown in Table 5.1, hydrodynamic radius varies from 1.4 nm for 4 kDa dextran to 28 nm for 2000 kDa dextran, and diffusivity varies from 1.5×10^{-6} cm^2/sec for 4 kDa dextran to 7.7×10^{-8} cm^2/sec for 2,000 kDa dextran. A size dependent bio-effects indicated that delivery efficiency might be limited by the pore size distribution created in cells during photoporation and/or the slower diffusion of macromolecules through the pores[12,203]. Therefore, we considered two hypotheses based on the above observation. The first hypothesis states that macromolecular delivery will be increased by increasing cell membrane pore size, which may be accomplished by increasing laser fluence (i.e. energy delivered per nanoparticle)[146].

Table 5.1: Hydrodynamic radius and diffusivity values for various fluorescent delivery molecules

Fluorescent molecule	Mw (kDa)	D (cm^2/sec)*	r_{Stokes} (nm)#
Calcein [203]	0.6	3.6×10^{-6}	0.6
Dextran – 4 [203]	4	1.5×10^{-6}	1.4
Dextran – 10 [204]	10	7.5×10^{-7}	2.9
Dextran – 40 [204]	40	4.4×10^{-7}	4.9
Dextran – 150 [203]	150	2.4×10^{-7}	8.9
Dextran – 500 [203]	500	1.4×10^{-7}	15
Dextran - 2000 [203]	2000	7.7×10^{-8}	28

*D: Diffusion coefficient determined in water at 25°C

#r_{Stokes}: Stokes radius calculated using the formula $r = kT/(6\eta\pi D)$, where k is Boltzman's constant, T is the absolute temperature, η is the viscosity, and D is the diffusion coefficient

The second hypothesis states that macromolecular delivery will be increased by increasing the time available for macromolecule diffusion to and across cell membrane pores, which should be accomplished by increasing laser exposure duration (i.e. total number of laser pulses).

5.3.2 Enhancing 2000 kDa dextran delivery by increasing laser fluence

To test the first hypothesis, we varied laser fluence from 25 mJ/cm^2 to 88 mJ/cm^2, while keeping the exposure duration and other parameters constant, and measured intracellular uptake of 2000 kDa dextran. Bio-effects data, plotted in Figure 5.3, showed that the total bio-effects increased with increasing fluence (one-way ANOVA, $p < 0.0001$) and saturated around ~100% at 66 – 88 mJ/cm^2 (one-way ANOVA, $p > 0.05$). However, percentage of cells with 2000 kDa dextran uptake initially increased when fluence was raised from 25 mJ/cm^2 to 44 mJ/cm^2 (one-way ANOVA, $p < 0.0001$) but then decreased with further increase in fluence till 66 mJ/cm^2 (one-way ANOVA, $p < 0.0001$). Further increase in fluence did not make a significant change in percentage of uptake cells (one-way ANOVA, $p > 0.05$). Therefore, results in Figure 1.3 indicate that increasing laser fluence can improve 2000 kDa dextran delivery however, at the expense of cell viability, especially at higher fluence. Highest uptake was seen for 44 mJ/cm^2 with ~47 ± 2% uptake cells and ~30 ± 1% cell viability loss. This suggests that increasing pore size might increase macromolecular delivery efficiency by photoporation however, viability loss places a restriction on reaching higher percentages of uptake cells.

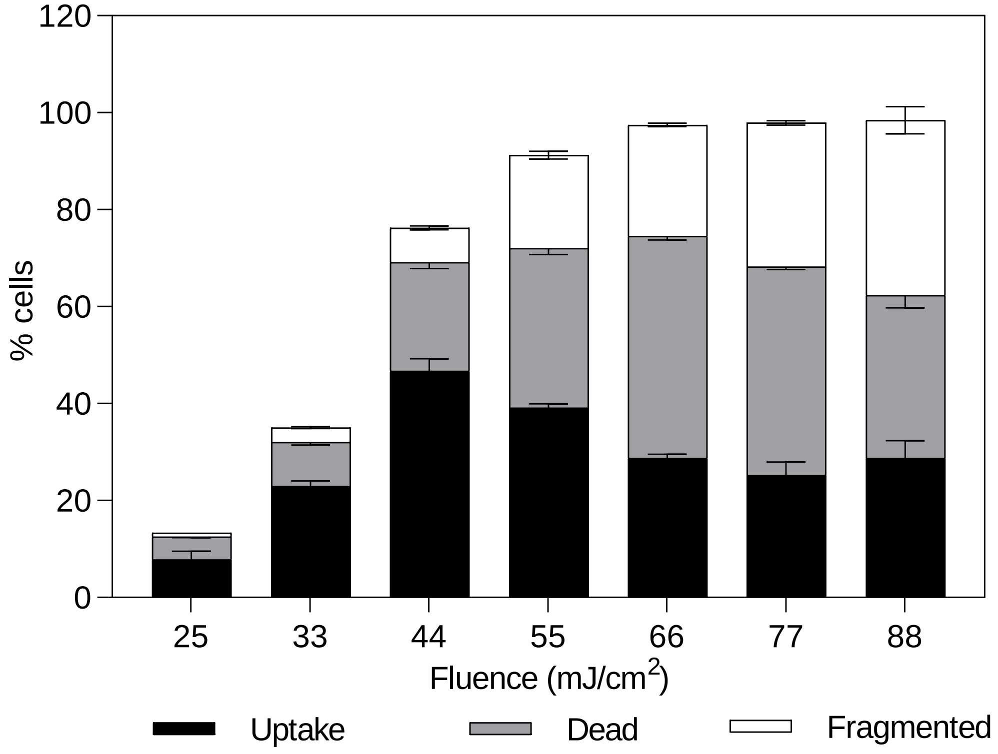

Figure 5.3: Changes in bio-effects as a function of laser fluence after laser exposure of DU145 cell suspension. Distribution of uptake cells, non-viable cells and fragmented cells is shown after laser exposure for 1 min. All samples contained 26.3 mg/L CB nanoparticles and 98 mg/L of 2,000 kDa dextran. Data are expressed as mean ± SEM based on 3 replicates each

5.3.3 Enhancing 2000 kDa dextran delivery by increasing exposure duration at low laser fluence

To test the second hypothesis, we explored whether increasing exposure duration (i.e. number of laser pulses) could enhance the intracellular delivery efficiency of 2000 kDa dextran. Exposure duration was varied from 1 min to 10 min while keeping laser fluence constant at a low level of 25 mJ/cm^2 or 29 mJ/cm^2. Increased laser exposure

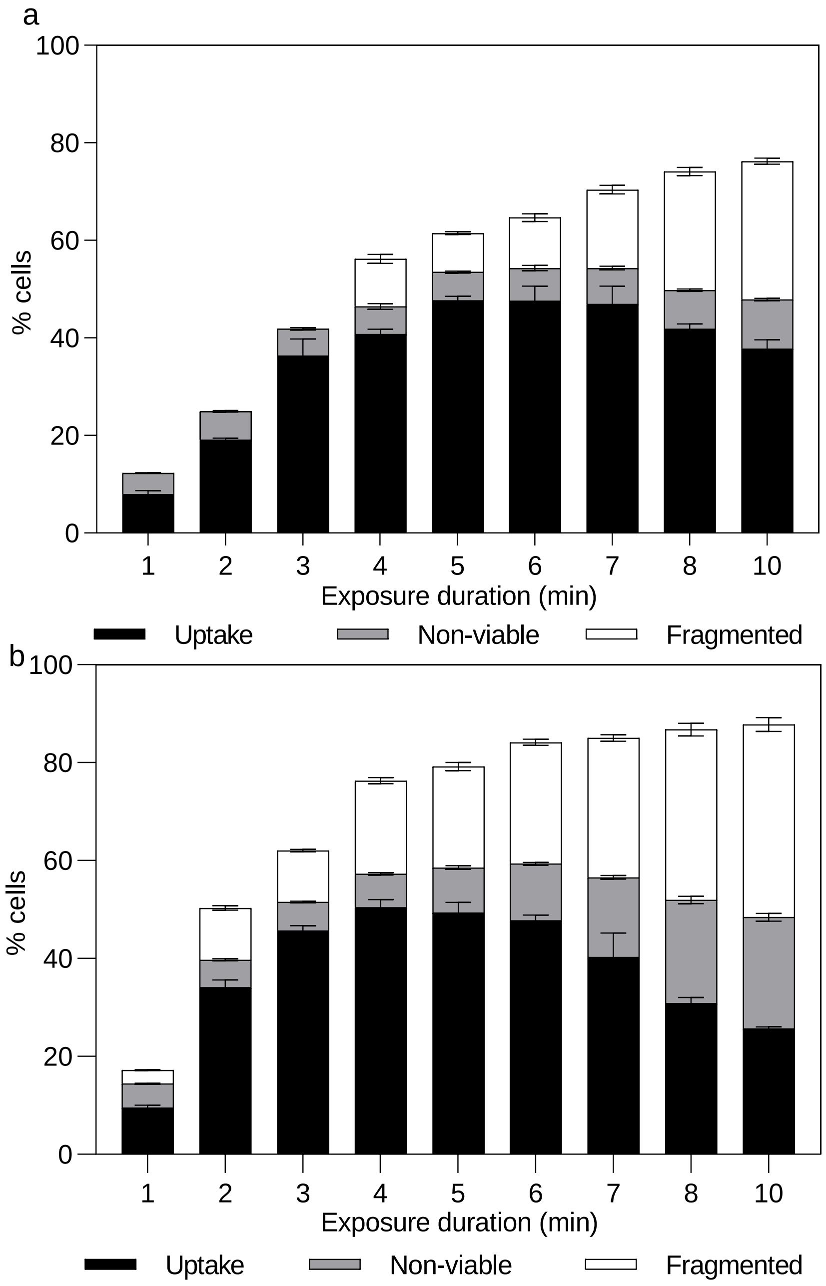

Figure 5.4: Changes in bio-effects as a function of laser exposure duration after laser exposure of DU145 cell suspension. Distribution of uptake cells, non-viable cells and fragmented cells is shown after laser exposure at (a) 25 mJ/cm^2 and (b) 29 mJ/cm^2 for 1 – 10 min. All samples contained 26.3 mg/L CB nanoparticles and 98 mg/L of 2,000 kDa dextran. Data are expressed as mean ± SEM based on 3 replicates each

duration was accomplished by increasing the total number of laser pulses because laser pulse width was fixed at 5 – 9 ns. Bio-effects data, plotted in Figure 5.4a, shows that at 25 mJ/cm^2 fluence, percentage of cells with 2000 kDa dextran uptake increased when the exposure duration was increased from 1 min to 5 min (one-way ANOVA, $p < 0.0001$). Further increase in exposure duration led to decrease in percentage of uptake cells (one-way ANOVA, $p < 0.01$) and increase in cell viability loss (one-way ANOVA, $p < 0.0001$ for both non-viable and fragmented cells).

Highest uptake was seen for 5 min exposure with ~48 ± 1% uptake cells and ~14 ± 1% cell viability loss. Therefore, we obtained less viability loss for highest delivery percentage when exposure duration was increased compared to increasing laser fluence. A subsequent experiment with 29 mJ/cm^2 laser fluence (Figure 5.4b) showed similar profile as seen at the lower fluence. However, in this case, highest uptake was seen for 4 min exposure with ~50 ± 2% uptake cells and ~26 ± 1% cell viability loss. Further increase in exposure duration led to decrease in percentage of uptake cells (one-way ANOVA, $p < 0.0001$) and increase in cell viability loss (one-way ANOVA, $p < 0.0001$ for both non-viable and fragmented cells).

5.3.4 Macromolecular delivery at low fluence and longer exposure duration

We saw that longer exposure duration at lower laser fluence was able to deliver 2000 kDa dextran with relatively high efficiency and low viability loss. To test the delivery efficiency of other macromolecules at these conditions, we performed photoporation experiments to deliver dextrans ranging in molecular weight from 4 kDa to 2000 kDa dextran at 25 mJ/cm^2 for 5 min exposure and at 29 mJ/cm^2 for 4 min

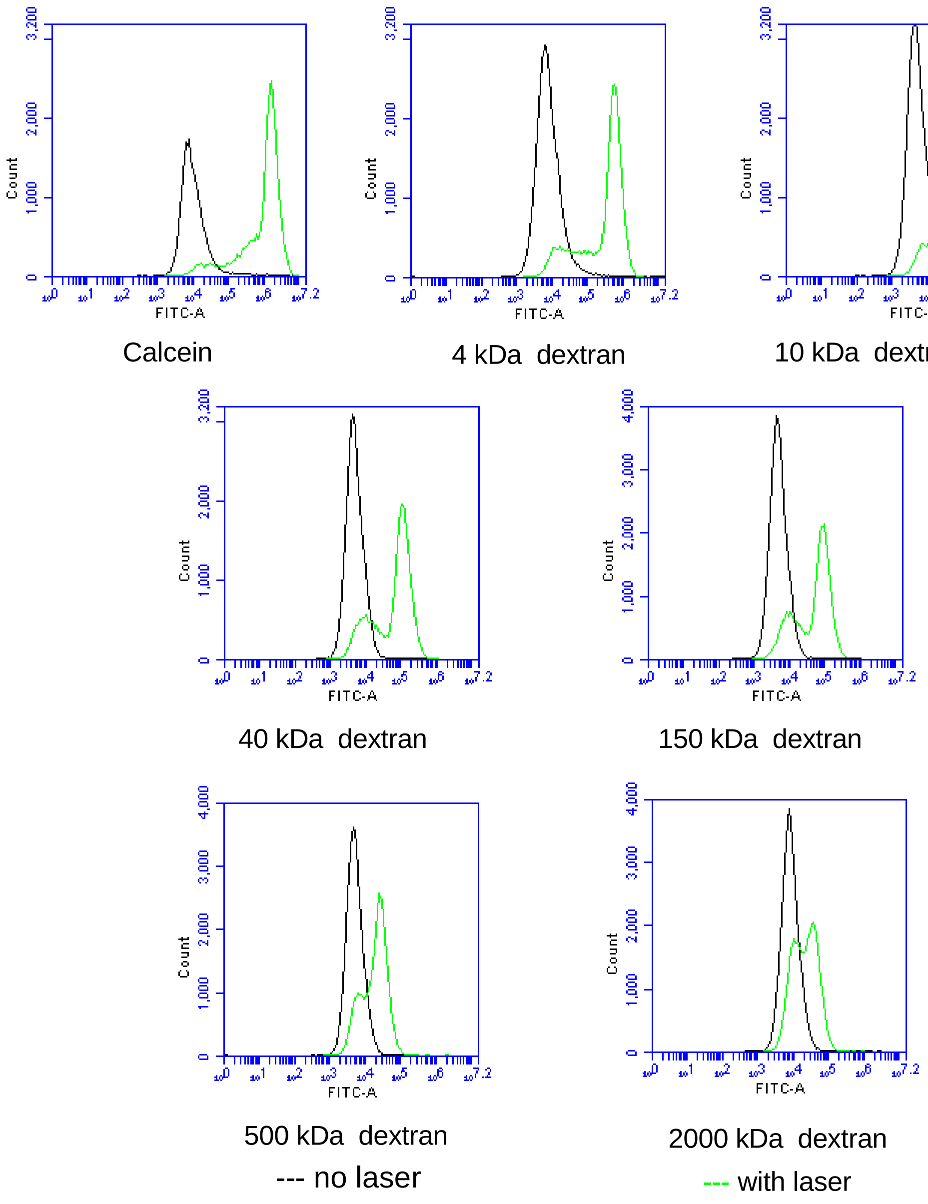

Calcein

4 kDa dextran

10 kDa dextran

40 kDa dextran

150 kDa dextran

500 kDa dextran

2000 kDa dextran

--- no laser

--- with laser

Figure 5.5: Representative flow cytometer histograms showing green (FITC) fluorescence intensity versus cell count plot after photoporation-mediated delivery of calcein and dextran (of molecular weights between 4 kDa and 2,000 kDa). "---no laser" plots have viable cells that were not exposed to laser pulses and were used as negative control, while "---with laser" plots have viable cells that were exposed to laser pulses at 25 mJ/cm^2 fluence for 5 min, and exhibit increased fluorescence corresponding to uptake of molecules. These histograms are each representative of 3 independent replicate samples.

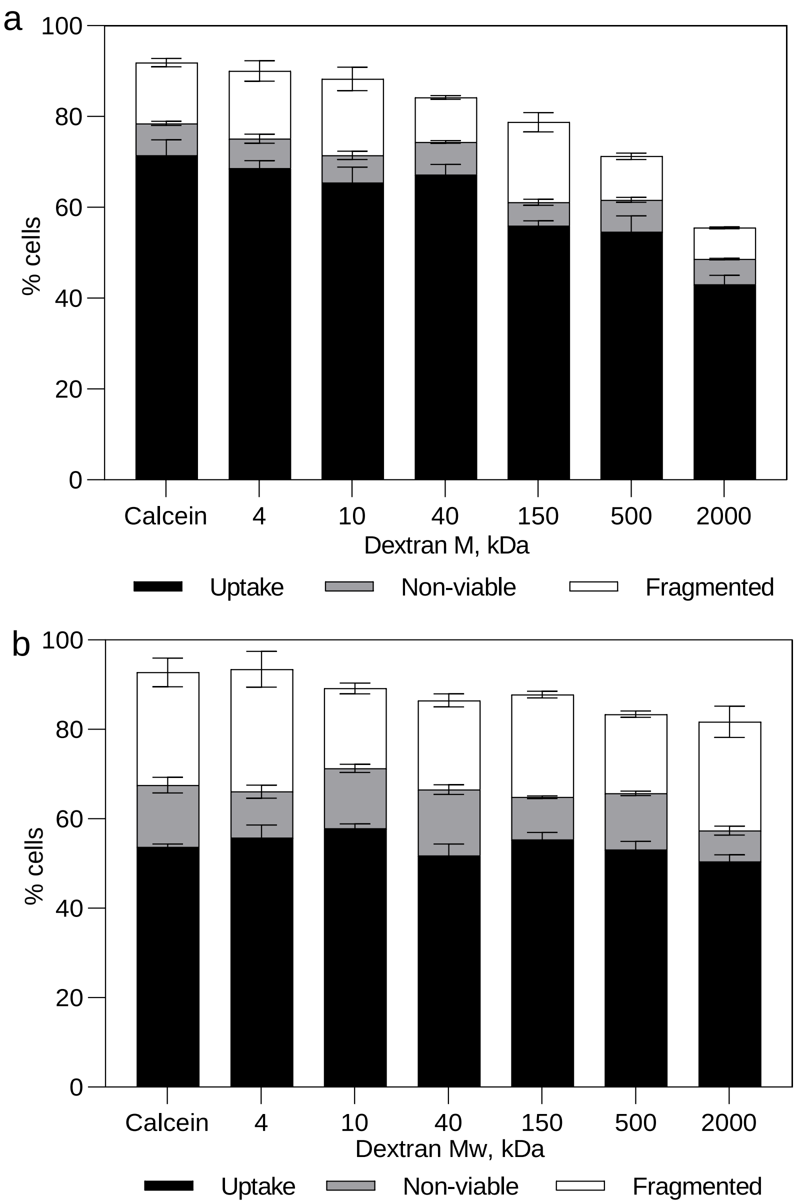

Figure 5.6: Changes in bio-effects as a function of molecular weight of the delivery molecule after laser exposure of DU145 cell suspension. Distribution of uptake cells, non-viable cells and fragmented cells is shown after laser exposure at a fluence of (a) 25 mJ/cm^2 for 5 min and (b) 29 mJ/cm^2 fluence for 4 min. All samples contained 26.3 mg/L CB nanoparticles and 98 mg/L of the uptake molecule: calcein or dextran with molecular weight ranging from 4 kDa to 2,000 kDa. Data are expressed as mean ± SEM based on 3 replicates each.

exposure. Figure 5.5 shows flow cytometer plots for number of intact and viable cells plotted against FITC fluorescence intensity for delivery of calcein and the dextrans. Like in Figure 5.1, we show “no laser” negative controls and “with laser” samples exposed to laser pulses at 25 mJ/cm^2 fluence for 5 min.

Corresponding bio-effects data in Figure 5.6a indicates that at 25 mJ/cm^2 fluence, percentage of uptake cells decreased with increasing molecular weight (one-way ANOVA, $p < 0.0001$). However, the delivery efficiency of macromolecules was significantly higher than Figure 5.2. At the original conditions studied, 69% – 14% of cells took up molecules over the range of molecular weights (Figure 5.2), whereas the optimized conditions resulted in uptake of the molecules to 71% - 43% of cells, which is significantly higher uptake (two-way ANOVA, p value < 0.0001)

Similarly, at 29 mJ/cm^2 fluence and 4 min exposure (Figure 5.6b), the percentage of cells with macromolecular delivery as a function of molecular weight was significantly greater (two-way ANOVA, p value < 0.0001) than at the original condition (Figure 5.2). At 29 mJ/cm^2 fluence at least 50% of cells took up molecules at all molecular weights over the range of 0.66 kDa (calcein) to 2,000 kDa (dextran).

5.4 Discussion

This study sought to identify conditions that enable efficient intracellular delivery of macromolecules by nanoparticle-mediate photoporation Through parametric sweep, previous studies were able to provide operating conditions for very high calcein delivery efficiency to DU145 cells without significant viability loss[12]. Similar observation was seen for calcein delivery into Chinese Hamster Ovary (CHO) cells using nanoparticle-mediated photoporation[205]. However, calcein is a small molecule, and there are many other molecules of interest for intracellular delivery that are much larger in size. Molecules like RNA and proteins range in size from 10s to 100s of kDa molecule weight, and plasmid DNA is typically greater than 1000 kDa.

Our study of dextrans ranging in molecule weight from 4 kDa to 2,000 kDa showed that delivery efficiency dropped dramatically with increasing molecular weight at the initial conditions studied (Figure 5.1). We hypothesized that this might occur not only because macromolecules may be sterically hindered during transport through transmembrane nanopores, and also because their diffusivity decreases with increasing molecular weight

Data in Figure 5.3 and Figure 5.4 showed that transport of 2,000 kDa dextran into cells was affected by the laser fluence and laser exposure duration. Increasing laser fluence at 1 min exposure increased percentage of cells with molecular uptake till it reached a certain maximum, after which the percentage started to decrease. Meanwhile, laser fluence increase also caused an increase in percentage of non-viable and fragmented cells, with percentage of fragmented cells increasing monotonically until the highest fluence applied. Similarly, increasing laser exposure duration at low fluence increased percentage of uptake cells until a maximum and then started to decrease. Non-viable and fragmented cell percentages also showed similar trend as seen when increasing fluence. However, at conditions corresponding to the maximum uptake percentage in each case, exposure duration increase had lower percentages of non-viable and fragmented cells compared to fluence increase, indicating that increasing exposure duration may be preferable to increasing laser fluence when optimizing for uptake of macromolecules.

Delivery of molecules into cells can be thought of in two steps: (i) transport from the bulk solution to the membrane surface and (ii) transport across the membrane through pores created by photoporation. Prior analysis of this type of transport process in the context of transmembrane pores created by sonoporation concluded that the rate-limiting step was transport from bulk solution to the edge of the pore on the membrane surface [203]. Because the plasma membrane of a cell measures on the order of 10 nm, even large macromolecules can diffuse that short distance relatively quickly.

To facilitate further analysis, we can calculate characteristic times for diffusion (t) as

$$t = \frac{L^2}{D} \tag{2}$$

where L is the characteristic distance of diffusion and D is the diffusivity of the diffusing molecules (diffusivity values are given in Table 5.1). This approach indicates that calcein diffuses a distance of 10 nm (i.e., cell membrane thickness) with a characteristic time of 30 ns and diffuses a distance of 10 µm (i.e., cell radius) with a characteristic time of 30 ms. In contrast, 2,000 kDa dextran diffuses with characteristic times that are three orders of magnitude longer, i.e., 10 µs and 10 s across a distance of 10 nm and 10 µm, respectively.

This analysis supports the idea that extending the duration of laser exposure may be especially important for delivery of macromolecules. While pores may only need to be open for microseconds in order to fill a cell with calcein, pores need to stay open for seconds in order to fill a cell with 2,000 kDa dextran. The 5-9 ns laser pulses separated by 100 ms gaps provides time for macromolecules near the membrane to diffuse into the cell during the short transmembrane pore lifetime and for those molecules to be replenished with new molecules from the bulk during the time between pulses, thereby providing new molecules to diffuse into the cell during the subsequent pulse.

With this in mind, we plotted percentage of uptake cells against $Mw^{-1/3}$ (which is a measure of molecular radius that is proportional to diffusivity[206]) in Figure 5.7a. For laser exposure for 1 min exposure, percentage of uptake cells increased linearly with $Mw^{-1/3}$ (one-way ANOVA, $p < 0.0001$; linear regression, $R^2 = 0.09677$) This linear dependence suggests that at this exposure condition, delivery efficiency may be directly limited by macromolecular diffusivity. When exposure time was increased to 4 or 5 min (at lower fluence values), the dependence of percentage of uptake cells on $Mw^{-1/3}$ was lowered (since the slope and linear regression, R^2 (= 0.6011 for 5 min and 0.0802 for 4 min) both lowered), though still significantly different than original exposure condition in Figure 5.1 (one-way ANOVA, $p < 0.01$).

This suggests that these longer laser exposures provided more time for viable, porated cells to take up enough molecules to achieve sufficient intracellular fluorescence to be considered an uptake cell. Rather than assessing the binary outcome of uptake or no uptake, we measured the FITC fluorescence intensity shift of laser irradiated cells as a measure of the number of dextran-tagged fluorophores delivered across cell membrane. When plotted against $Mw^{-1/3}$ in Figure 5.7b, we found that the mean fluorescence intensity shift for all three exposure conditions (i.e., 1, 4 and 5 min) increased linearly with $Mw^{-1/3}$ (one-way ANOVA, $p < 0.0001$; linear regression, $R^2 = 0.9166$ for 5 min, 0.9234 for 4 min and 0.9079 for 1 min). We also found that fluorescence levels for the 4 and 5 min exposure conditions were significantly higher than at the 1 min exposure condition (two-way

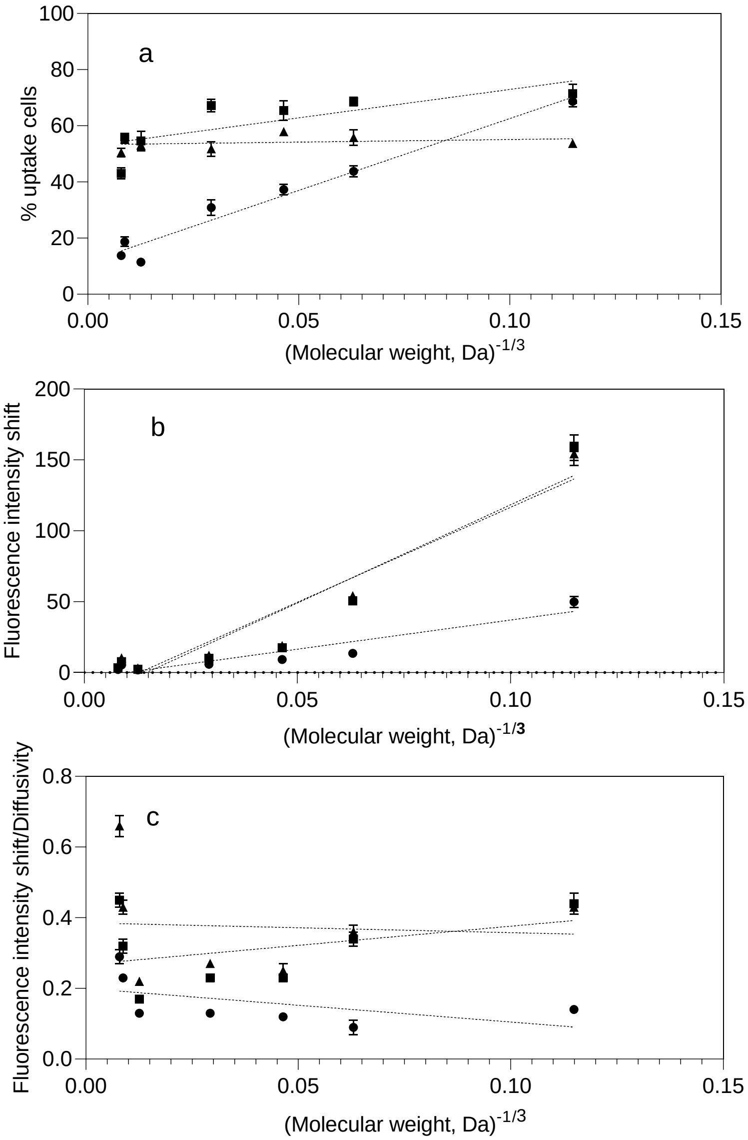

Figure 5.7: Analysis of changes in bio-effects after laser exposure of DU145 cell suspension based on size of uptake molecules. (a) Percentage of uptake cells, (b) mean fluorescence intensity shift among uptake cells, and (c) mean fluorescence intensity shift/diffusivity among uptake cells is plotted versus molecular weight$^{-1/3}$, which is a measure of molecular radius. Cells were exposed to laser at a fluence of ● 33mJ/cm^2 for 1 min, ■ 25 mJ/cm^2 for 5 min and ▲ 29 mJ/cm^2 for 4 min. All samples contained 26.3 mg/L CB nanoparticles and 98 mg/L of the uptake molecule: calcein or dextran with molecular weight ranging from 4 kDa to 2,000 kDa. Data are expressed as mean ± SEM based on 3 replicates each.

ANOVA, $p < 0.0001$). This is again consistent with diffusivity being the rate limiting step to determine extent of molecular uptake into a cell.

Finally, when mean FITC fluorescence intensity shift of laser exposed cells was normalized to the diffusivity of the delivered macromolecules and plotted against $Mw^{-1/3}$, Figure 5.7c shows that the slopes of the linear correlations were not significantly non-zero for 4 and 5 min exposure conditions (linear regression, $p > 0.05$). This finding provides further support for the dependence on intracellular transport of macromolecules being directly limited by their rates of diffusion.

5.5 Conclusion

This study investigated the use of nanoparticle-mediated photoporation for intracellular delivery of macromolecules. When DU145 cells were exposed to NIR laser pulses in the presence of CB nanoparticles, we found that intracellular uptake of molecules depended significantly on molecular weight (ranging from 0.6 kDa to 2,000 kDa) when using 1 min exposures previously optimized for delivery of a small molecule (calcein). Increasing laser fluence to increase percentage of cells with macromolecular uptake led to higher viability loss. In comparison, increasing exposure duration (i.e. number of laser pulses) at low fluence led to higher percentage of cells with macromolecular delivery with lower cell viability loss and, in one case, intracellular uptake no longer depended on molecular weight. Further analysis suggested that intracellular delivery may be diffusion limited, which scales with $Mw^{-1/3}$. We conclude that delivery of macromolecules into cells by nanoparticle-mediated photoporation is optimized by using laser pulses with longer exposure time at lower fluence. This observation may be explained by longer exposure times providing more time for macromolecules to diffuse to and into cells, which occurs more slowly than for smaller molecules.

CHAPTER 6. DISCUSSION

6.1 Context from prior literature

Intracellular delivery of molecules through the use of external sources has been investigated in literature for several years[142,207]. These can have potential applications in cellular studies, imaging, diagnostics and therapy. Creating transient cell membrane pores through the application of external forces has often been more efficient due to their ability to bypass the endocytic pathway, which reduces drug efficacy. These external forces have been generated using electroporation, ultrasound, microfluidics, etc., and are applicable to most cell types. However, the major challenge of these methods is balancing the trade-off between percentage of cells with molecular uptake and viability loss.

An alternate route for intracellular delivery using nanoparticle-mediated photoporation was introduced recently[6]. Initial studies with CB nanoparticles and femtosecond laser pulses showed efficient delivery of uptake markers while maintaining high cell viability. Later, nanosecond laser pulses were used instead of femtosecond lasers due to their ease of handling and instrument cost, in addition to it being globally researched for several clinical applications[8]. CB nanoparticles were chosen based on their broad-spectrum absorbance feature (300 nm to 1100 nm), while 1064 nm wavelength was chosen based on their weak absorption by tissue material and body fluids such as water and blood. Use of this combination ensured that in a system of CB nanoparticles, cells and cell suspension media, irradiated with 1064 nm laser pulses, CB nanoparticles would preferentially absorb the laser, with little or no direct effect of the laser on cells and suspension media. Through several parametric studies in the prior literature, nanoparticle-mediated photoporation was optimized to deliver fluorescent calcein molecules to almost 90% of DU145 prostate cancer cells while maintaining high cell viability. In addition, 13 kDa siRNA was also delivered, causing EGFR knockdown in 49% of ovarian cancer cells exposed to laser pulses in presence of CB nanoparticles[11].

Several studies were conducted to explore the underlying mechanism of nanoparticle-mediated photoporation. After several iterations, the proposed mechanism included generation of transient vapor bubbles surrounding nanoparticles, producing local photoacoustic and thermal output due to the interaction between CB nanoparticles and laser pulses. These generated outputs were believed to cause external stress on cell membrane causing transient pore formation, allowing the delivery of target molecule inside cellular cytosol. It was shown that the nanoparticles absorb energy delivered through laser and heat up to temperatures greater than 100^{o}C within 10 ns. In addition, the pores created by laser exposure close significantly faster than after ultrasound and electroporation exposure, which translated into higher delivery percentages with lesser cell viability losses[7].

Subsequent studies investigated the role of cellular mechanics on nanoparticle-mediated photoporation and concluded that intracellular delivery efficiency could be enhanced by destabilizing cytoskeleton[10]. However, no significant changes were observed for cytoskeleton strengthening and cell membrane fluidity manipulation. Furthermore, it was proposed that energy input per cell is strong predictor of bio-effects caused by photoporation. However, the above study did not account for other energy parameters that can also alter bio-effects[9].

Through this thesis, we aim to bridge some of the knowledge gap that exists between understanding the role of several components associated with nanoparticle-mediated photoporation in causing cell membrane poration and intracellular delivery of molecules. In particular, we looked into the effects of changing cellular microenvironment on bio-effects and further explored their implications.

6.2 Role of nanoparticle and associated energy transduction parameters

CB nanoparticles suspended with cells during laser irradiation act as energy transducer, absorbing energy delivered through laser pulses and generating acoustic and thermal output. To understand the role of nanoparticle's physical properties on bio-effects, we tried to explore the effects of changing nanoparticle material, size and shape. However, varying each property individually was not possible due to the limitations set by available nanoparticles. For example, when SiC nanoparticles were used instead of CB, several properties such as nanoparticle size, 1064 nm light absorbance, heat capacity and thermal conductivity changed. Therefore, it was difficult to extract the role of these individual properties on nanoparticle-mediated photoporation. However, we realized that any given nanoparticle property change would eventually affect the energy transduction parameters and we can measure those changes by theoretically calculating three associated transient parameters – peak nanoparticle temperature, number of bubbles formed during laser irradiation and peak bubble size.

Through subsequent studies, we demonstrated that each of these energy transduction parameters could individually alter bio-effects, and thus are all significant in causing photoporation. We also showed that bio-effects can be enhanced by increasing a product

P, derived using power law correlation of transduction parameters. This suggests that several combination of peak nanoparticle temperature, number of bubbles and bubble size can cause similar bio-effects as long as their product parameter P remains the same. For example, if there is a restriction on the number of nanoparticles that can be used, then bubble size and peak nanoparticle temperature can be manipulated to provide desired bio-effects. In addition, our studies also found that we cannot control bio-effects by controlling one energy parameter (total energy absorbed, energy absorbed per nanoparticle and energy per nanoparticle mass), which means no single dominant energy parameter exists that can be used to manipulate nanoparticle-mediated photoporation.

6.3 Role of serum addition in cell suspension media

This section was focused on exploring and understanding the role of serum addition in cell suspension media associated with nanoparticle-mediated photoporation. Experimental results showed that presence of serum during laser irradiation aids in cell viability preservation, enabling high percentage of viable cells with molecular uptake. This ability of serum is greatly amplified at high laser fluence irradiation (> 44 mJ/cm^2), when majority of cells would lose viability due to cell death and fragmentation. Conversely, when serum was present, amount of viable cells increased by up to 350%, especially at serum concentrations equal to or above 10%.

Subsequent studies showed that albumin proteins present in serum were responsible for this viability protection feature; however, this ability was not exclusive to albumin proteins only. Cell viability benefited from presence of HG proteins as well and showed enhanced delivery efficiency. We also found that protein biological activity was not required for viability protection since use of denatured serum proteins showed no significant difference from regular serum in providing viability protection.

Irrelevance of protein biological activity in providing viability protection indicated that this feature can be mimicked by other molecules as well. Literature has examples of several polymers being used for improving cell culture productivity by providing protection against “fluid-mechanical damages” in bioreactors[167]. Additionally, polymers such as PEG and Pluronics have also been used for improving cell viability during electroporation and nanoparticle-mediated photoporation[132,173]. We were successful in showing that some neutral charge and hydrophilic polymers, such as PVP, PEG, PEOX and Pluronic F127 can provide viability protection during laser irradiation. Our experiments also revealed dependence of viability protection on polymer hydrophobicity and molecular weight. Additionally, we showed that although adding serum in cell suspension media increased its viscosity, this viscosity change was not responsible for viability protection.

Altogether, these results suggest that viability protection provided by serum was caused by non-biological interactions between serum proteins and cell membrane; which can be mimicked by polymer additives as well through hydrophobic interactions with cell membrane.

6.4 Role of delivery molecule size and subsequent optimization to enhance macromolecular delivery

Several attempts of delivering macromolecules using nanoparticle-mediated photoporation were made in past. However, the delivery percentages achieved were significantly low compared to calcein, especially for macromolecules > 100 kDa in size[12,126]. Our initial studies revealed a direct dependence of delivery percentage on molecular weight high calcein delivery condition. For example, at 33 mJ/cm^2 fluence for 1 min exposure, < 20% of cells had uptake of macromolecules of size > 100 kDa, compared to ~70% cells showing 0.66 kDa calcein uptake. These lower delivery efficiencies can be attributed to the decrease in diffusivity values with increase in molecular weight. We observed a linear relation between percentage of cells with molecular uptake and $Mw^{-1/3}$, which is proportional to diffusivity.

Learning from these results, we hypothesized that the macromolecular delivery efficiency could be enhanced by either increasing laser fluence (to generate larger cell membrane pores) or increasing duration of laser irradiation at low fluence (to allow greater diffusion times for macromolecules). Corresponding experimental studies provided data in support of the above two hypotheses. We were able to increase percentage of uptake cells with 2000 kDa Dextran in both the cases. However, trade-off between percentage of uptake cells and viability loss was more favorable at low laser fluence and longer exposure duration.

We were successful in delivering 500 kDa and 2000 kDa dextran to > 50% and > 45% of cells respectively. This was significantly greater than ~5% delivery of DNA plasmids of similar size achieved previously. Further analysis revealed that by increasing exposure duration at low laser fluence, not only were we delivering macromolecules to more percentage of cells, but we also delivered a greater number of macromolecules inside cellular cytosol.

CHAPTER 7. CONCLUSIONS AND RECOMMENDATIONS

7.1 Conclusions

Nanoparticle-mediated photoporation is a novel delivery platform that has potential to efficiently deliver diagnostic and therapeutic molecules intracellularly. Through this work, we explored the effects of changes in cellular microenvironment on cellular responses. Specifically, we highlighted the role of nanoparticle and associated transient parameters, investigated cell responses to the presence of serum during photoporation and, provided operating conditions for enhanced macromolecular delivery.

First, we demonstrated that changing nanoparticle composition directly influences energy transfer from laser to nanoparticle and from nanoparticle to surrounding fluid media. We also provided correlation between energy transduction parameters and final bio-effects caused by laser irradiation in presence of CB nanoparticles. Second, we showed that presence of serum proteins during laser irradiation provides cell viability protection and, for some exposure conditions, enhance percentage of cells with molecular uptake. Evidence suggested that albumin proteins (present in serum) were responsible for this feature; however, we showed that viability protection can be achieved using other protein molecules as well as certain neutral and hydrophilic polymers. Finally, yet importantly, we showed that macromolecular delivery appeared to be diffusion limited and the percentage of cells with macromolecular uptake can be enhanced by using lower laser fluence and longer exposure duration (i.e. greater number of pulses). This result is vital because it paves a way forward to deliver molecules such as proteins and plasmid DNAs, which are essential for novel therapies and diagnostics.

In summary, this thesis contributed to developing an understanding, of the role played by cellular microenvironment in nanoparticle-meditated photoporation; and provides a way forward to translate this platform technology, to deliver macromolecules of therapeutically relevant sizes, for *in vitro* applications. A typical use of nanoparticle-mediated photoporation has been for photothermal ablation, which are mainly focused on inducing local hyperthermia resulting in cell death[208]. However, this thesis provides a way to use nanoparticle-mediated photoporation for therapeutic applications by delivering molecules into cellular cytosol while maintaining high cell viability. Potential of serum proteins and polymers to be used as viability protection additives adds another paradigm in efficient intracellular drug delivery. Additionally, this thesis also provides a systematic study on the role of transient parameters involved in energy transduction, causing photoporation. The correlations developed can be used to generate desired bio-effects by controlling initial operating conditions.

7.2 Recommendations

7.2.1 In vitro protein and plasmid DNA delivery

Based on the results generated in CHAPTER 5, we now have the ability to deliver macromolecules of size > 100 kDa to close to 50% of cells. Since this platform technology is generally not limited by cell type, various diseases models and cellular diagnostic modalities can be tested. For example, as proof of concept, 150 kDa Dengue-HuMAbs can be delivered to DENV-infected Vero cells and checked for viral neutralization[101]. Further, delivery of larger GFP plasmid DNA to mammalian cells can be done using fluorescently tagged plasmids, and additional expression studies can be done using flow cytometry and/or fluorescent microscopy image analysis[209]. Most GFP expression studies require 48-72 hours after transfection and thus cells will need to be replated and harvested after the said duration of time for analysis.

Majority of non-viral methods report < 10% transfection efficiency for genetic cargo delivery even with high intracellular delivery percentages. Often this low percentage is attributed to negligible control over nuclear translocation of delivered genetic molecule and subcellular pathways leading to expression. We recommend Glucocorticoid (GC)-priming of cells, which has been used to enhance transgene expression[210]. Dexamethasone – an anti-inflammatory GC drug has been shown to promote transgenic reporter activity by manipulating downstream activity and thus can be used for improved expression[211].

7.2.2 Macromolecular delivery enhancement using viability protective additives

Presence of serum or certain polymer additives were shown to provide cell viability protection and improve percentage of uptake cells in CHAPTER 4. All these studies were conducted with 0.62 kDa calcein as delivery molecule. We propose using this advantage to improve macromolecular delivery efficiency. We conducted experiments to investigate whether adding 1 w/v% Pluronic F127 to cell suspension media will enhance percentage of cells with > 100 kDa molecule uptake. Use of Pluronic was given priority due to its cost benefits and general acceptance as cell repair additive[212].

Preliminary experiments in APPENDIX C gave us some promising results. We observed that percentage of cells with150 kDa and 500 kDa molecule uptake significantly higher when cells were suspended in media containing 1% F127 compared to no F127 media. It is important to mention that CB nanoparticles used, for this study, were 243 nm in diameter instead of regular 195 nm CB nanoparticles in previous chapters of this thesis. One big difference, caused by this change was higher bio-effects at any given experimental condition due to which, higher percentages of uptake cells were seen at lower exposure durations (for 150 kDa and 500 kDa molecules).

However, the percentage delivery for 2000 kDa molecules could not be improved to more than 30%. We recommend increasing laser exposure duration for 2000 kDa delivery since, we believe that delivery of 2000 kDa is diffusion limited (from CHAPTER 5). In addition, a parametric study with different nanoparticle size, concentration, laser fluence and exposure duration should provide more options to increase uptake percentage of 2000 kDa molecule delivery. Eventually, use of Pluronic F127 can be applied to enhance delivery and transfection efficiency of protein and nucleic acids. We do not recommend increasing percentage of Pluronic to more than 1 w/v% since that would also lead to significant rise in media viscosity and that would subsequently restrict molecular transport in extracellular space.

7.2.3 Use of liquid nanodroplets instead of solid nanoparticles as energy transducers

Energy transfer efficiency of CB nanoparticles governs the generation of thermal and acoustic output that cause cell membrane poration. The dependence on a solid energy transducer can be minimised by using liquid Perfluorocarbon (PFC) nanodroplets. PFC nanodroplets comprise of liquid PFC core and photoabsorber, encapsulated in a stabilizing lipid shell. When irradiated with laser pulses, the photoabsorber can absorb energy delivered and vaporize liquid PFC core, rapidly expanding in volume due to phase change.

This rapid volume expansion has been shown to produce photoacoustic waves, which in our case, can be utilized to transiently permeabilize cell membrane[213].

We investigated the use of PFC nanodroplets to enable intracellular delivery of calcein in APPENDIX B. For the experimental conditions tested, a maximum of ~20% uptake was observed at 88 mJ/cm^2 for 2.5 min exposure. Subsequent increase in exposure duration resulted in higher viability loss while laser fluence increase was restricted by the laser setup. Additionally, measured zeta potential of PFC dispersion was 0.28 mV which is highly unstable. Thus, lower delivery efficiency may be attributed to unstable dispersion in cell suspension and settling of PFC nanodroplets during laser irradiation, which would severely lower interactions between laser and nanodroplets. However, no experimental study was done to quantify the above-mentioned limitations. Therefore, we recommend studying dispersion properties such as photoacoustic and thermal output during laser irradiation. Photoacoustic output can be measured using needle hydrophone while thermal output can be calculated through bulk temperature rise measurements using thermocouple[13].

APPENDIX A. CUVETTE BOUNDARY EFFECTS

Several external factors/parameters in the cellular microenvironment can affect the bio-effects caused by nanoparticle-mediated photoporation. Some of these parameters such as nanoparticle concentration, laser fluence and exposure duration have been studied previously.

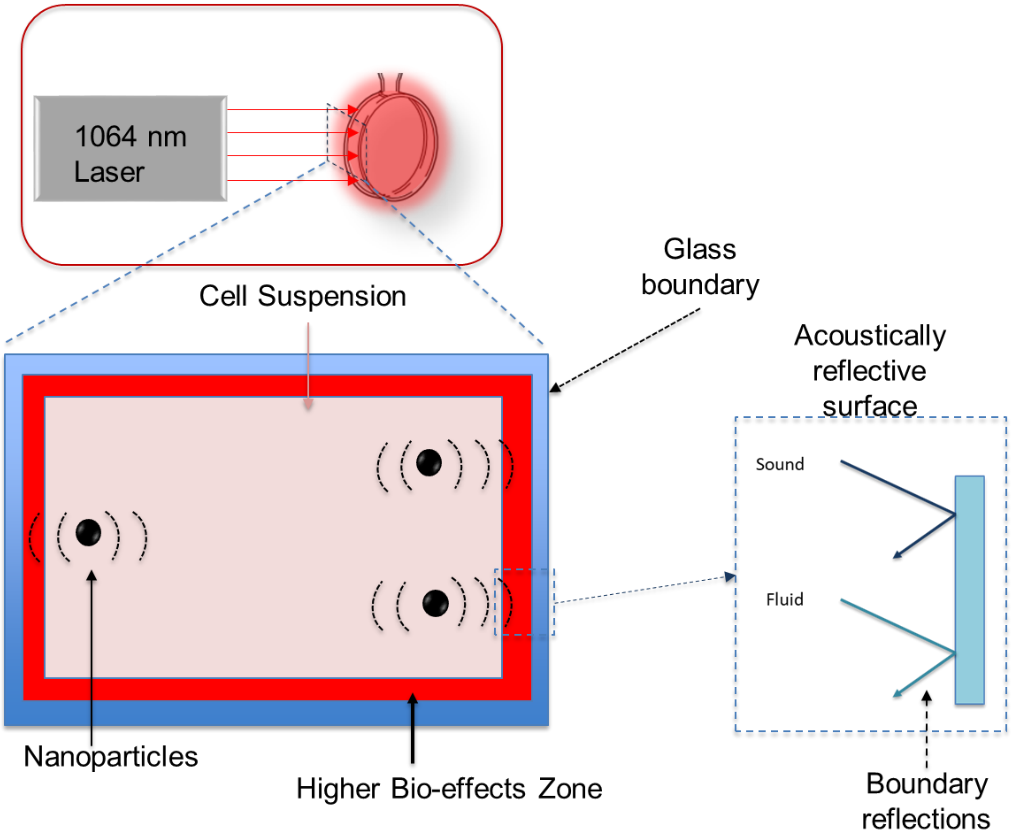

Figure A.1: A schematic representation of boundary effects caused by the acoustic density differences between cell suspension media, cuvette glass boundary and surrounding air.

The previous chapters of this thesis evaluate the role of nanoparticle and laser properties, cell-suspension media properties, as well as the size of the delivery molecules.

However, most of the past and current *in vitro* studies are done using Pyrex cuvette system, which have rigid glass boundary. The following sections evaluate the role of cuvette boundary in nanoparticle-mediated photoporation.

Due to acoustic impedance differences of sample fluid, glass boundary and surrounding air, the acoustic waves generated during laser exposure of CB nanoparticles, can be reflected from the fluid-solid interface (Figure A.1). This in turn can amplify the bio-effects caused by photoporation, by the interaction of these reflected waves with cells close to cuvette boundary (hence, we named this phenomenon as "boundary effects"). Previous studies had indicated that the presence of rigid glass boundary might cause greater bio-effects due to boundary reflections[214]. This study is a further extension, investigating whether presence of cuvette glass boundary does indeed cause greater bio-effects. We used variable path length and acoustically transparent cuvettes to analyze the effects of cuvette boundary on photoporation to distinguish between the effects of acoustic reflections and local fluid mechanics at the boundary. We also introduced a new experiment setup by sandwiching the glass cuvette between two acoustically transparent cuvettes filled with water to lower the acoustic reflections from the cuvette boundary.

A.1 Materials and methods

A.1.1 Cell preparation

DU145 human prostate carcinoma cells (American Type Culture Collection, VA) were grown in tissue culture flasks with cell media containing RPMI 1640 Medium (Cellgro, Herndon, VA), with 10% FBS (Corning, Palo Alto, CA) and 1% P/S (Cellgro). They were incubated at 37^{o}C, 5% CO_2 and 98% relative humidity levels during growth period. Cells were cultured at 85% confluency using 0.25% Trypsin/EDTA (Cellgro). After harvesting, DU145 cells were suspended in RPMI at a concentration of 10^6 cells/ml.

A.1.2 Nanoparticle dispersion preparation

CB nanoparticle dispersion preparation was done using 25 nm diameter CB nanoparticles (Black Pearls 470, Cabot, Boston, MA) and DI water. CB nanoparticles were added at a concentration of 1600 mg/L or 400 mg/L to DI water containing 0.013% (v/v) Tween-80 (Sigma-Aldrich, St. Louis, MO) to enhance solution stability (prevent particle aggregation for a homogeneous dispersion). The solution was first sonicated for 35 min in an ultrasonic water bath (FS3OH, Fisher Scientific, Pittsburg, PA) and then with an ultrasonic needle for 1 min (Sonics Ultracell, Sonics & Materials, Newton, CT). CB nanoparticles tend to aggregate in aqueous dispersions and thus the final aggregate diameter was measured to be 195 nm using Dynamic light scattering (DLS) measurements (ZetaSizer Nano, Malvern Instruments, Malvern, UK).

A.1.3 Exposure sample preparation

Exposure samples were prepared by mixing 520 µL of DU145 cells (10^6/mL) suspended in RPMI, 37 µL of 1600 mg/L or 400 mg/L CB dispersion and 5.5 µL of 1mM calcein (Molecular Probes, Eugene, OR) solution in a 1.5 mL Eppendorf tube. The final CB nanoparticle concentration became 105 mg/L or 26.3 mg/L and calcein concentration became 10 µM. Samples were stored in ice bath to reduce endocytosis/cellular activity before and after-laser exposure.

A.1.4 Laser exposure and cell wash

Cell samples were transferred to a 21 mm diameter cylindrical Pyrex glass cuvette (37-PX-2, Starna Cells, Atascadero, CA) or 3D printed low-density polyethylene (LDPE) cuvette with saran wrap (polyethylene) flat walls for laser exposure. For acoustically transparent walls, these cuvettes were sandwiched between LDPE cuvette with saran wrap flat walls shown in figure A.4a. An Nd:YAG solid-state laser (Continuum Powerlite II Plus, Continuum, San Jose, CA) was used as laser source to apply 5-9 ns pulses of 1064 nm wavelength at a frequency of 10 Hz. Samples were exposed to laser beam (21 mm diameter), which irradiated the whole surface with flat top (uniform) energy profile. Immediately after exposure, samples were transferred back to the Eppendorf tubes and stored in ice. Negative controls in the form of 'sham' exposures were samples containing cells, CB nanoparticles, and calcein that experienced the same handling and procedures except the laser exposure. To label non-viable cells post laser-irradiation, PI (Invitrogen, Grand Island, NY) was added at a final concentration of 13.4 μM for 10 min on ice. Cell samples were then washed 3 times with phosphate buffer saline (PBS) to remove excess calcein from the bulk solution before analysis.

A.1.5 Data Collection

Flow cytometry - Cells were analyzed using a bench-top flow cytometer (BD Accuri, BD Biosciences, San Jose, CA) to quantify bio-effects in terms of viable cells with intracellular uptake and non-viable cells (i.e. intact cells with PI staining). Calcein fluorescence was measured using 530/28 nm bandpass filter with excitation at 488 nm and PI fluorescence was measured using a 670 nm longpass filter with excitation at 535 nm. Cell samples were run at constant flow rate of 35 μL/min for 1 min. A negative control containing only cells in RPMI was used to construct a cell population gate in the forward-scattered (FSC) and side-scattered (SSC) analysis. Cells within this gate were considered to be intact cells. To account for possible cell loss due to cell fragmentation (appearing as low forward scatter and low side scatter events on the flow cytometer), the difference between the number of viable cells detected in a given sample and the number of viable cells detected in sham samples was taken as the number of cells lost to fragmentation. Samples were run at a constant flow rate of 35 μL/min for 1 min.

Power transmittance measurements - Laser beam power was measured using pyroelectric laser sensor (Ophir-Spiricon, LLC, North Logan, UT) with appropriate power rating connected to a power meter (Ophir Nova II, Ophir-Spiricon). At first, true laser power was measured by placing laser sensor in front of cuvette being irradiated with laser beam. Next, the laser sensor was moved behind the cuvette to measure the power transmitted through the glass cuvette. The difference between initial and exit power gave energy loss in cuvette due to absorption and scattering.

A.1.6 Data Analysis

A minimum of 3 replicates were used for each experimental condition. Mean and standard error of the mean were calculated using the 3 replicates. One-way analysis of variance (ANOVA, $\alpha = 0.05$) was performed to compare 3 or more experimental conditions using Graphpad Prism 8 (GraphPad Software, La Jolla, CA) followed by post-hoc Tukey's pairwise comparison. A value of $p < 0.05$ was considered statistically significant.

A.2 Results

A.2.1 Changing cuvette width to minimize the percentage of cells near glass boundary

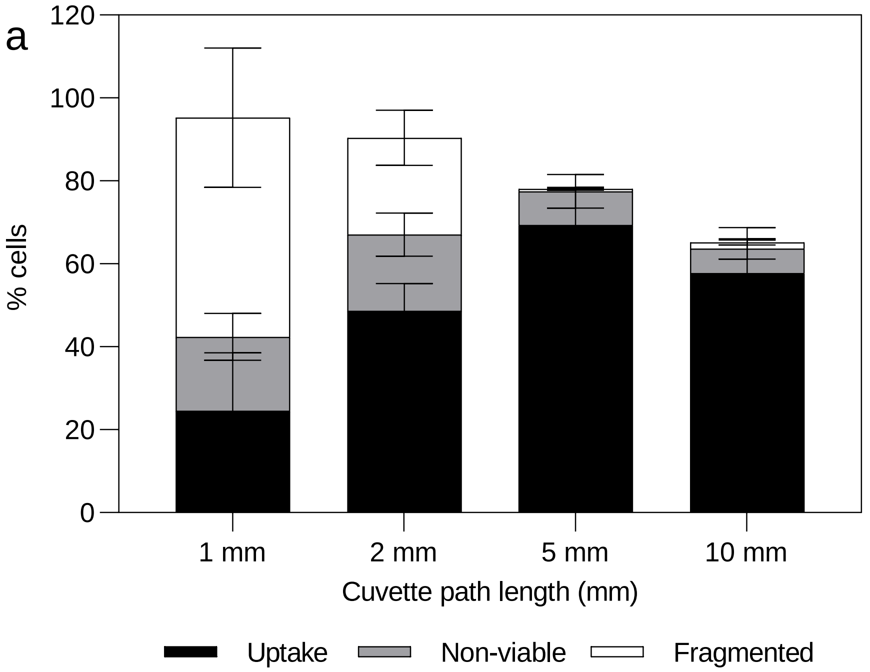

Figure A.2: Bio-effects plot at 44 mJ/cm^2 fluence, 1min exposure using 105 mg/L CB nanoparticle concentration for variable cuvette path length (width). All samples 10 µM calcein. Data are expressed as mean ± SEM based on 3 replicates each.

The first experiment designed to check for boundary effects was using variable cuvette width (1 mm to 10 mm wide) for cell suspension during laser irradiation. A 1 mm wide cuvette will have more percentage of cells close to the glass boundary than a 25 mm cuvette. Cells suspensions with 105 mg/L CB nanoparticles and calcein, were placed inside cuvettes with variable width and irradiated with 44 mJ/cm^2 laser fluence for 1 min (or 600 pulses). Bio-effects plots in Figure A.2 shows that percentage of uptake cells increased with increasing cuvette width (one-way ANOVA, $p < 0.01$) while percentage of non-viable (one-way ANOVA, $p < 0.05$) and fragmented cells decreased (one-way ANOVA, $p < 0.001$). This decreased loss in viability implies reduction of bio-effects with increasing cuvette width. To check whether the lowering of bio-effects was caused due to reduction of percentage of cells encountering reflected acoustic waves (causing boundary effects) or simply due to power loss due to cuvette width increase, we measured power transmitted through the cuvettes during laser irradiation. Table 2 shows initial power before the laser beam entered glass cuvette and exit power after laser beam crossed the whole cuvette (as shown in Figure A.3).

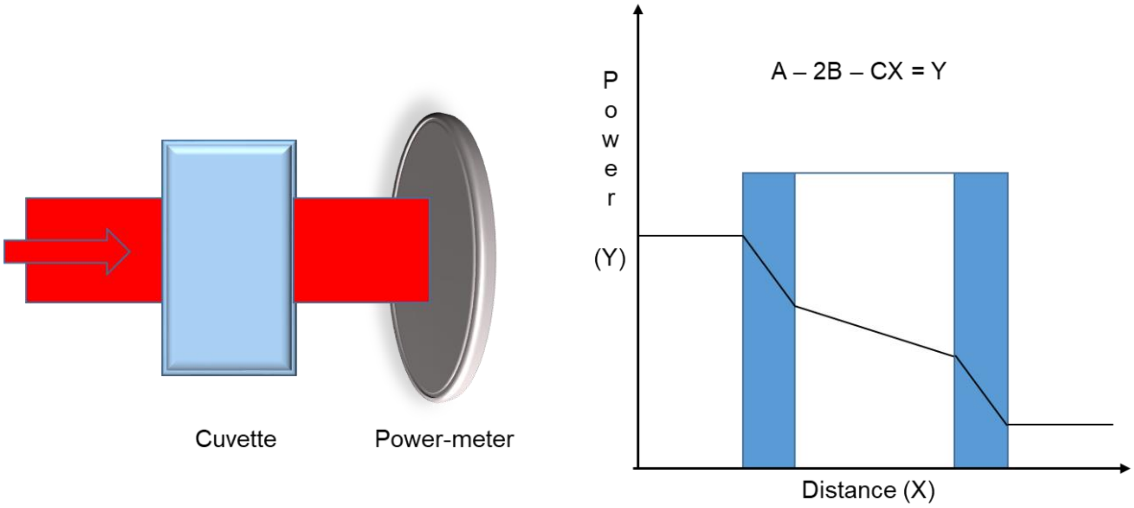

Figure A.3: A schematic representation of power loss caused interactions between laser beam and cuvette of varying path lengths (width). A: Initial power reading; B: Power loss in glass window; C: CB suspension loss factor; X: Distance from front window; Y: Exit power

This power loss can be attributed to energy absorbed and scattered by CB nanoparticles inside glass cuvette. Wider cuvette will have higher number of nanoparticles contributing to power loss. Therefore, CB nanoparticles in 25 mm cuvettes will encounter lower laser power on average than CB nanoparticles in 1 mm cuvettes. Subsequent bio-effects in 25 mm cuvettes should be lower compared to 1 mm cuvette, which appears to be the case in Figure A.2. Therefore, it is difficult to claim that the lowering of bio-effects with cuvette width increase was caused by reduction in boundary effects only.

Table A.1: Power transmission loss through cuvette measurements during laser exposure

Cuvette path length (width)	**Initial power (A), W**	**Final power (Y) transmitted through cuvette filled with CB and RPMI, W**	**% loss at exit**
1 mm	2.04 ±0.00	1.44 ±0.033	30%
2 mm	2.04 ±0.002	1.22 ±0.013	40%
5 mm	2.04 ±0.002	0.62 ±0.006	70%
10 mm	2.04 ±0.002	0.25 ±0.012	88%

A.2.2 Changing acoustic impedance difference to investigate effects of boundary reflections

To lower acoustic reflections from glass-air interface, as would be the case in a normal laser exposure experiment where cell suspensions are placed inside a glass cuvette and irradiated with laser pulses, two new cuvette designs were used (as shown in Figure A.4). In first design, the circular/curved boundary (2 mm wide) of the cell suspension cuvette was made of LDPE using 3D printing. Saran wrap was used to cover the flat surface/walls of the plastic cuvette (pc). This plastic cuvette was then sandwiched between two waterbath cuvettes made from same LDPE material with saran wrap stuck as flat surface/walls. In the second design, Pyrex glass cuvette was used as middle cell suspension cuvette however; two LDPE cuvettes (similar to the first design) were placed on either side to act as waterbath (figure A.4a). The waterbath cuvette width was varied from 2 mm to 25 mm to lower the acoustic reflections from plastic-air interface. Experimental results showed differences in bio-effects for cells placed inside varying width of waterbath cuvette

(Figure A.5). The first comparisons were between cells exposed to laser pulses with and without water bath for either plastic or glass cuvette.

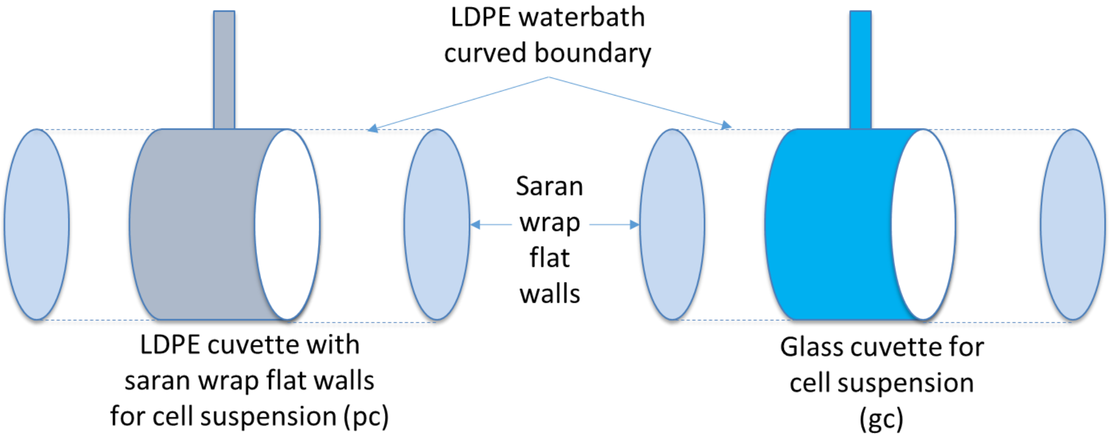

Figure A.4: A representative figure for cuvette with water bath design. pc – plastic cuvette made with LDPE 3D printed curved boundary and saran wrap flat walls; gc – glass cuvette made with Pyrex glass curved boundary and flat walls

Percentage of uptake cells whenever the cells were placed in waterbath were higher compared to when cells were not placed in waterbath, irrespective of the type of cell suspension cuvette used and the width of waterbath ($p < 0.05$). Additionally, either percentage of non-viable cells or fragmented cells (sometimes both) were lower for cells placed in waterbath compared to when cells were not placed in waterbath ($p < 0.05$). Second comparisons were between cells exposed to laser pulses in varying width of the waterbath. Percentage of uptake cells increased with increasing waterbath width (one-way ANOVA, $p < 0.0001$) while percentages of non-viable cells (one-way ANOVA, $p < 0.001$) and fragmented cells decreased (one-way ANOVA, $p < 0.01$), irrespective of type of cell suspension cuvette used.

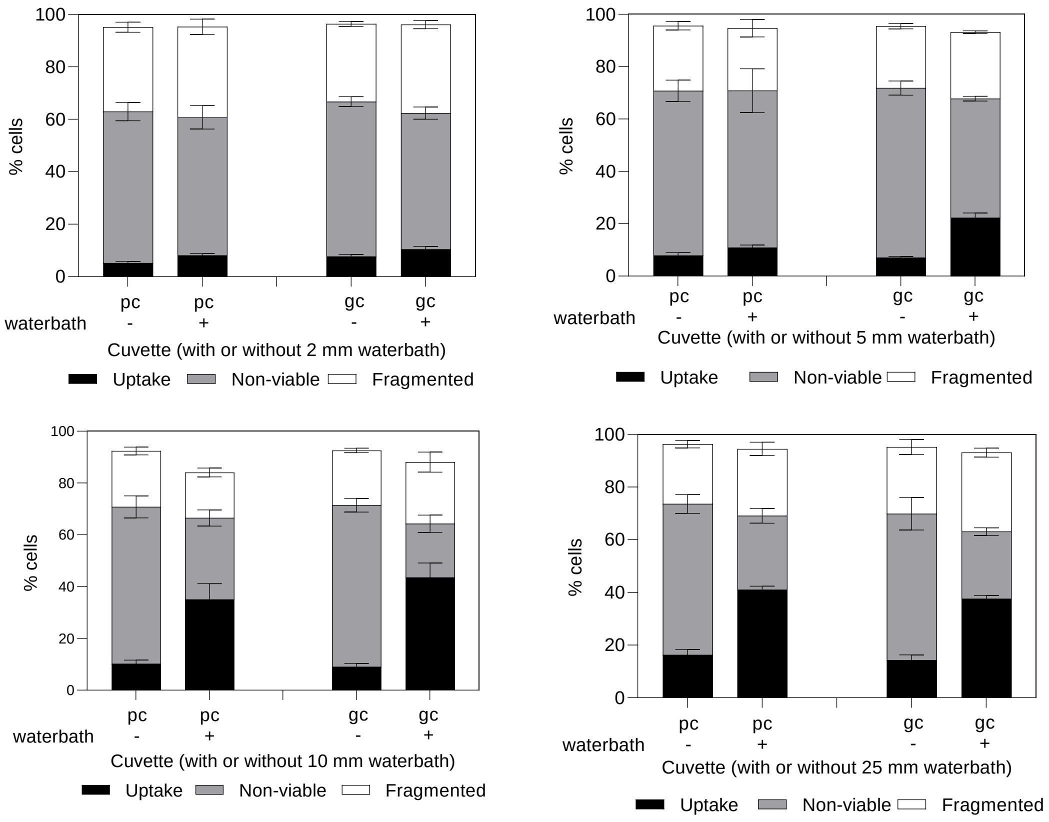

Figure A.5: Bio-effects plot at 55 mJ/cm^2 fluence, 1min exposure using 26.3 mg/L CB nanoparticle concentration for 2 mm cuvettes submerged in variable width of water bath. All samples 10 µM calcein. Data are expressed as mean ± SEM based on 3 replicates each.

These two comparisons show that bio-effects were lowered by adding waterbath, which suggests that adding waterbath reduced the acoustic reflections and thus bio-effects caused by boundary reflections were also lowered. However, lowering of boundary reflections indicates that the acoustic waves generated inside cell suspension cuvette, were able to traverse the solid boundary and penetrate the waterbath. To check whether these acoustic waves were actually responsible for causing boundary effects (i.e. higher bio-effects near solid walls), we designed another experiment where the cells suspension was kept in the middle cuvette and the CB was suspended in the waterbath. If the acoustic waves could traverse through the solid walls and are the cause of boundary effects then we should see significant bio-effects in the cells placed in the middle cuvette.

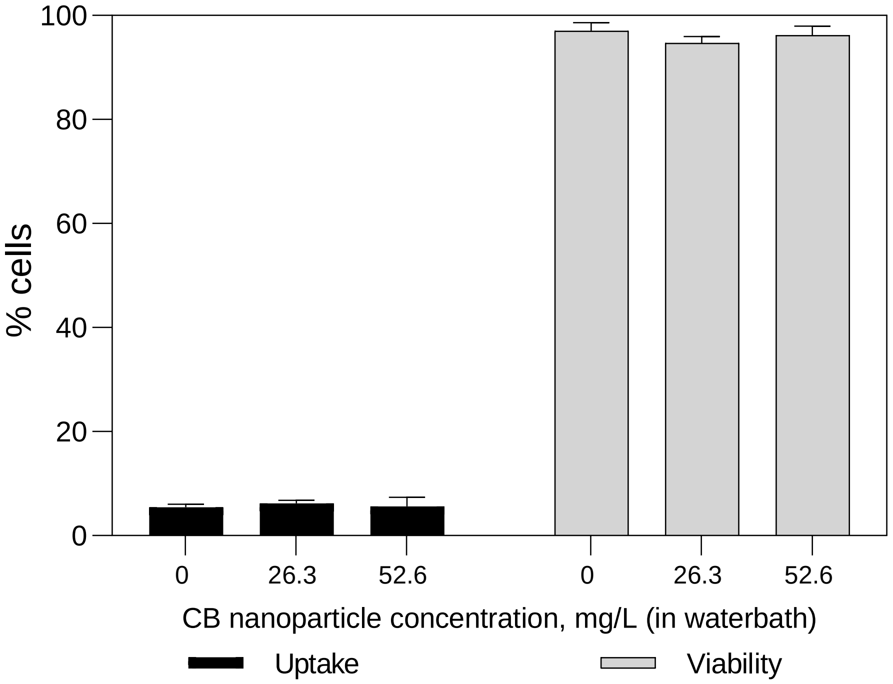

Figure A.6: Uptake and viability plot of cells suspension placed in middle cuvette and CB nanoparticles placed in waterbath. This design was irradiated with 77 mJ/cm^2 laser fluence for 1 min. All samples 10 µM calcein. Data are expressed as mean ± SEM based on 3 replicates each.

Results from 77 mJ/cm^2 laser fluence irradiation (as shown in Figure A.6) showed no significance differences between percentage of uptake cells at varying CB nanoparticle concentrations of 0 mg/L, 26.3 mg/L and 52.6 mg/L (one-way ANOVA, $p > 0.05$). Similarly, no differences were observed between percentages of viable cells at the three CB nanoparticle concentrations (one-way ANOVA, $p > 0.05$). These results imply that the acoustic waves generated in waterbath either did not traverse the solid boundary or were not significant enough to cause bio-effects. Analogically, if acoustic reflections were responsible for boundary effects seen in Figure A.5 but if acoustic waves could not traverse the solid boundary then adding waterbath should not lower bio-effects. Similarly, if acoustic waves did traverse the solid boundary but were not significant enough to cause bio-effects (as seen in Figure A.6), then again, dampened acoustic reflections should not be the cause of lower bio-effects seen in figure A.4b.

Since, acoustic reflections did not produce convincing results to prove that they can cause bio-effects and thus be the reason for boundary effects, we tried to explore the reasons of lower bio-effects seen in figure A.4b. One of the side effects of adding a waterbath could be lowering of bulk temperature. This in turn can also lower bio-effects.

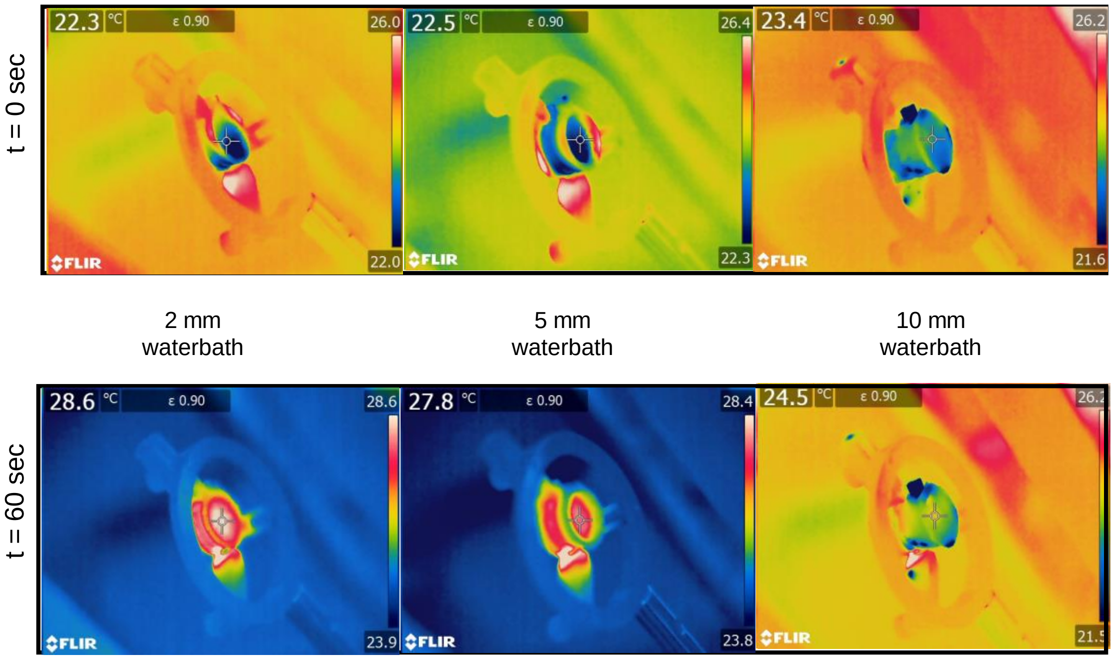

Figure A.7: Surface temperature measured at t = 0 and at t = 60 sec for 55 mJ/cm^2 fluence, 1min exposure using 26.3 mg/L CB nanoparticle concentration. All of these cases had 2 mm glass cuvettes submerged in variable width of water bath. All samples 10 µM calcein. Data are representative of 3 independent replicate samples.

To check whether adding waterbath did actually lower the temperature rise and affect heat transfer, we took infrared (IR) images of the cuvettes before and during laser irradiation, which provided surface temperature data (as shown in Figure A.7). IR imaging data revealed that temperature rise was lower for higher width waterbath. For example, as shown in Figure A.7, 6.3^{o}C temperature rise was recorded when 2 mm waterbath was used. However, the temperature rise recorded was 5.3^{o}C for 5 mm waterbath and only 1.1^{o}C for 10 mm waterbath.

A.3 Conclusion

In this appendix, we tested the hypothesis that acoustic boundary reflections lead to greater bio-effects, through two different study designs –i) changing cuvette width to vary the percentage of cells near cuvette boundary and, ii) using acoustically transparent cuvettes to minimize boundary reflections. We demonstrated that changing cuvette width does lead to lower bio-effects; however, this change might have been brought about by higher power loss in wider cuvettes. Further, we also showed that the design implemented to lower acoustic reflections did cause reduced bio-effects, however bulk temperature reduction also might have significant contribution in doing so. Therefore, in conclusion, we failed to find concrete evidence to support the hypothesis that acoustic boundary reflections were causing additional bio-effects.

APPENDIX B. PHOTOPORATION USING PERFLUOROCARBON NANODROPLETS

Recently, perfluorocarbon (PFC) nanodroplets have been explored as alternative for enhanced imaging and a potentially effective drug delivery vehicle[213]. Optically triggered PFC nanodroplets are composed of a liquid PFC core and encapsulated photoabsorber, all encased in a stabilizing lipid shell. After pulsed laser irradiation, the nanodroplets convert from liquid to gas, producing a photoacoustic signal (Figure B.1). PFC nanodroplets produce very small bubbles, can remain longer in aqueous solutions, and can undergo surface modification for potential targeted drug delivery. Vaporized nanodroplets also show more stable cavitation with minimal damage to surrounding tissue[213]. Additionally, the heat of vaporization of PFC liquids is lower than the heat of vaporization of water; therefore, PFC should require less heat to phase change[215].

We hypothesized that PFC nanodroplets could be used instead of CB nanoparticles to generate thermal and acoustic output through pulsed 1064 nm laser light irradiation, which could further be utilized to cause photoporation for intracellular molecular delivery.

B.1 Materials and methods

B.1.1 Cell preparation

DU145 human prostate carcinoma cells (American Type Culture Collection, VA) were grown in tissue culture flasks with cell media containing RPMI 1640 Medium (Cellgro, Herndon, VA), with 10% FBS (Corning, Palo Alto, CA) and 1% P/S (Cellgro). They were incubated at 37°C, 5% CO_2 and 98% relative humidity levels during growth period. Cells were cultured at 85% confluency using 0.25% Trypsin/EDTA (Cellgro). After harvesting, DU145 cells were suspended in RPMI at a concentration of 10^6 cells/ml.

B.1.2 PFC nanodroplets synthesis

We used the protocol described by Georgia Tech's Ultrasound Imaging and Therapeutics Research Laboratory. Glass syringe and round-bottom flask were first cleaned using chloroform. With the glass syringe, 0.1 mL DSPE-mPEG2000 and 0.02 mL DSPC (Avanti Polar Lipids Inc., AL) were added to the round-bottom flask. Next, 1 mg of Epolight 3072 dye (Epolin, NJ) was mixed to the lipid/chloroform solution. Chloroform was then evaporated using a RotoVap. The water bath was heated to 60°C and the circulating water was cooled to 20°C. Next, the vacuum pressure was lowered to 474 mmHg while spinning the flask at 100 rpm. This flask was then subjected to a continuous flow of Nitrogen gas to dry any residual chloroform. Next, 1 mL of PBS was added to the round bottom flask and parafilm was used to seal the flask. The solution was then vortexed and placed in a water bath sonicator for 5 minutes to homogenize. The solution was then transferred to a 2 mL centrifuge tube and spun for 1 min at 100 rcf, to pellet excess dye. The supernatant was transferred to a glass vial, and PBS was then added to bring the total volume back to 1 mL. Then, 50μL of perfluorohexane (Fluoromed, TX) was added to the solution and the vial was placed in ice and allowed to cool. A probe sonicator was used to mix the solution. Before using the droplets, the stock solution was diluted (1:20 or greater) and placed in a bath sonicator for 5 minutes.

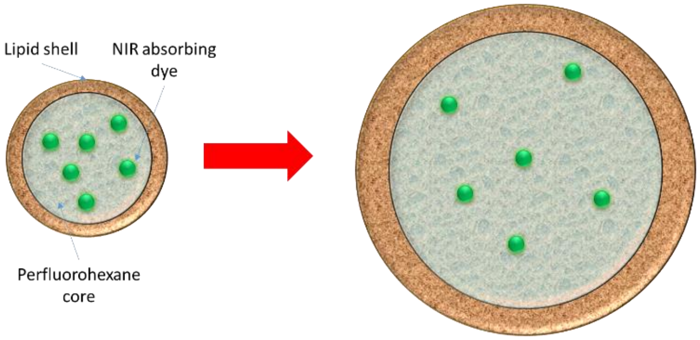

Figure B.1: A schematic representation (not to scale) of PFC nanodroplets before and after laser irradiation

B.1.3 Exposure sample preparation

Exposure samples were prepared by mixing 520 µL of DU145 cells (10^6/mL) suspended in RPMI, 37 µL of PFC solution and 5.5 µL of 1mM calcein (Molecular Probes, Eugene, OR) solution in a 1.5 mL Eppendorf tube. Samples were stored in ice bath to reduce endocytosis/cellular activity before and after-laser exposure.

B.1.3 Laser exposure and cell wash

Cell samples were transferred to a 21 mm diameter cylindrical Pyrex glass cuvette (37-PX-2, Starna Cells, Atascadero, CA). An Nd:YAG solid-state laser (Continuum Powerlite II Plus, Continuum, San Jose, CA) was used as laser source to apply 5-9 ns pulses of 1064 nm wavelength at a frequency of 10 Hz. Samples were exposed to laser beam (21 mm diameter), which irradiated the whole surface with flat top (uniform) energy profile. Immediately after exposure, samples were transferred back to the Eppendorf tubes and stored in ice. Negative controls in the form of 'sham' exposures were samples containing cells, PFC nanodroplets, and calcein that experienced the same handling and procedures except the laser exposure. To label non-viable cells post laser-irradiation, PI (Invitrogen, Grand Island, NY) was added at a final concentration of 13.4 μM for 10 min on ice. Cell samples were then washed 3 times with phosphate buffer saline (PBS) to remove excess calcein from the bulk solution before analysis.

B.1.4 Data collection

Cells were analyzed using a bench-top flow cytometer (BD Accuri, BD Biosciences, San Jose, CA) to quantify bio-effects in terms of viable cells with intracellular uptake and non-viable cells (i.e. intact cells with PI staining). Calcein fluorescence was measured using 530/28 nm bandpass filter with excitation at 488 nm and PI fluorescence was measured using a 670 nm longpass filter with excitation at 535 nm. Cell samples were run at constant flow rate of 35 μL/min for 1 min. A negative control containing only cells in RPMI was used to construct a cell population gate in the forward-scattered (FSC) and side-scattered (SSC) analysis. Cells within this gate were considered to be intact cells. To account for possible cell loss due to cell fragmentation (appearing as low forward scatter and low side scatter events on the flow cytometer), the difference between the number of viable cells detected in a given sample and the number of viable cells detected in sham samples was taken as the number of cells lost to fragmentation. Samples were run at a constant flow rate of 35 μL/min for 1 min.

B.1.6 Data Analysis

A minimum of 3 replicates were used for each experimental condition. Mean and standard error of the mean were calculated using the 3 replicates. One-way analysis of variance (ANOVA, $\alpha = 0.05$) was performed to compare 3 or more experimental conditions using Graphpad Prism 8 (GraphPad Software, La Jolla, CA) followed by post-hoc Tukey's pairwise comparison. A value of $p < 0.05$ was considered statistically significant

B.2 Results and discussion

Cells suspended with PFC nanodroplets and calcein were exposed to laser pulses for 1 min and 66 mJ/cm^2, 77 mJ/cm^2 and 88 mJ/cm^2. These higher fluences were chosen to investigate if there will be any bio-effects due to the acoustic waves produced by the vaporization of PFC nanodroplets. Results in Figure B.2 indicate very low bio-effects with percentage of uptake cells lower than 6% (one-way ANOVA, $p > 0.05$). Similarly, no significant differences were seen in non-viable cells (one-way ANOVA, $p > 0.05$), while no cells were lost due to fragmentation at all three fluences.

When cells were irradiated at 88 mJ/cm^2 but for higher exposure durations (1 min to 10 min), bio-effects seemed to increase with percentage of cells reaching ~20% at 2 min exposure (Figure B.3). However, further increase led to higher cell viability loss and percentage of uptake cells could not increase beyond 20%.

DLS size measurements gave an average diameter of 204.7 nm (±2.95 nm) for PFC nanodroplets and Zeta potential of 0.28 mV (±0.90 mV). It is possible that PFC nanodroplets were unstable in solution and thus may not remain homogenously distributed for a long time inside glass cuvette during laser irradiation. This might be one of the reasons for very low calcein delivery efficiency even at high exposure fluence. The viability loss observed for longer exposure duration at 88 mJ/cm^2 can be attributed to cell damage due to high laser energy for a prolonged duration.

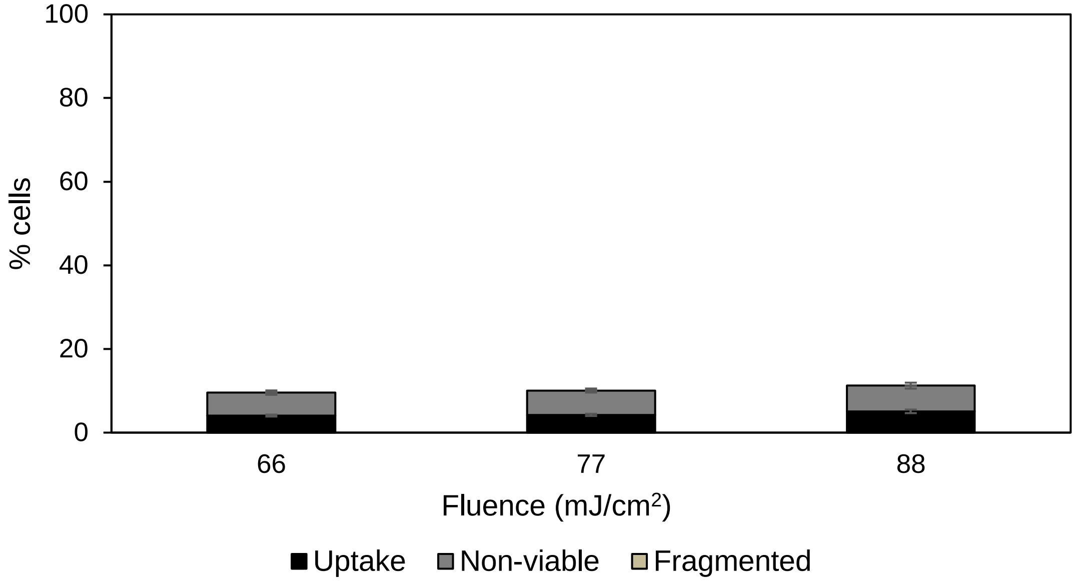

Figure B.2: Bio-effects plot for calcein delivery using PFC nanodroplets at 66, 77, 88 mJ/cm^2 for 1 min exposure. All samples 10 µM calcein. Data are expressed as mean ± SEM based on 3 replicates each.

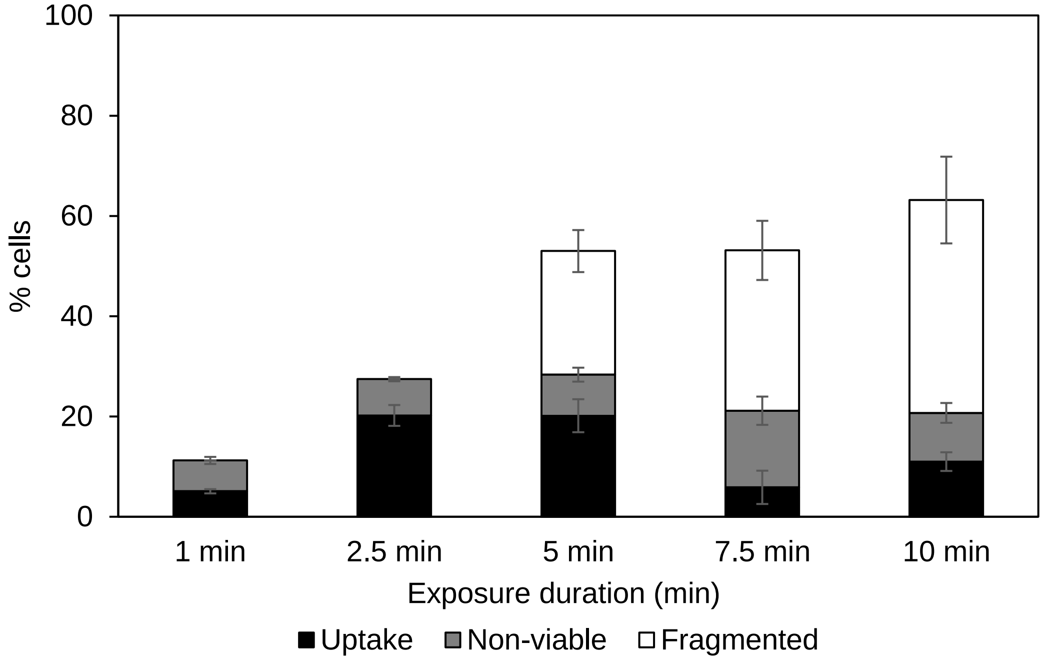

Figure B.3: Bio-effects plot for calcein delivery using PFC nanodroplets at 88 mJ/cm^2 for variable exposure duration. All samples 10 µM calcein. Data are expressed as mean ± SEM based on 3 replicates each.

B.3 Conclusion

PFC nanodroplets have shown potential to be used for intracellular drug delivery applications. However, a systematic parametric study comprising of PFC nanodroplets concentration, laser fluence, exposure duration as well as cell concentration is essential to figure out the optimized conditions for higher delivery percentages. Dispersion instability of PFC nanodroplets also needs to be addressed to push forward its *in vitro* applications.

APPENDIX C. MACROMOLECULAR DELIVERY USING BIGGER NANOPARTICLES, WIDER CUVETTES AND VIABILITY PROTECTION ADDITIVES

In CHAPTER 5, we showed that low laser fluence and higher exposure duration could enable higher macromolecular delivery. CB nanoparticles used in those studies were 195 nm in diameter and the cell suspensions were placed inside a 2 mm glass cuvette during laser exposure. We wanted to investigate the effects of changing nanoparticle size and glass cuvette width on the delivery efficiencies of molecules > 100 kDa in size.

Therefore, in this section, we first compare macromolecular delivery efficiency between 195 nm and 243 nm CB nanoparticles. We also evaluate the effects of increasing cuvette width from 2mm to 5 mm. Furthermore, since, serum and certain polymer additives can be used to provide cell viability protection during photoporation, we subsequently explore delivering high molecular weight dextran using nanoparticle-mediated photoporation, leveraging the cell viability protection offered by Pluronic F127 additives.

C.1 Materials and methods

C.1.1 Cell preparation

DU145 human prostate carcinoma cells (American Type Culture Collection, VA) were grown in tissue culture flasks with cell media containing RPMI 1640 Medium (Cellgro, Herndon, VA), with 10% FBS (Corning, Palo Alto, CA) and 1% P/S (Cellgro). They were incubated at 37^oC, 5% CO_2 and 98% relative humidity levels during growth period. Cells were cultured at 85% confluency using 0.25% Trypsin/EDTA (Cellgro). After harvesting, DU145 cells were suspended in RPMI or 1% w/v luronic F127 at a concentration of 10^6 cells/ml.

C.1.2 *Nanoparticle dispersion preparation*

CB nanoparticle dispersion preparation was done using 25 nm (Black pearls 470, Cabot, Boston, MA) or 81 nm diameter CB nanoparticles (N700, Continental Carbon Company, TX) and DI water. CB nanoparticles were added at a concentration of 400 mg/L, 800 mg/L or 1000 mg/L to DI water containing 0.013% (v/v) Tween-80 (Sigma-Aldrich, St. Louis, MO) to enhance solution stability (prevent particle aggregation for a homogeneous dispersion). The solution was first sonicated for 35 min in an ultrasonic water bath (FS3OH, Fisher Scientific, Pittsburg, PA) and then with an ultrasonic needle for 1 min (Sonics Ultracell, Sonics & Materials, Newton, CT). CB nanoparticles tend to aggregate in aqueous dispersions and thus the final aggregate diameter was measured to be 195 nm (for 25 nm particles) and 243 nm (for 81 nm particles) using Dynamic light scattering (DLS) measurements (ZetaSizer Nano, Malvern Instruments, Malvern, UK).

C.1.3 *Exposure sample preparation*

Exposure samples were prepared by mixing 1300 µL of DU145 cells (10^6/mL) suspended in RPMI, 92.5 µL of 400 mg/L, 800 mg/L or 1000 mg/L CB dispersion and 13.75 µL of 10 g/L FITC-labelled dextran (Sigma-Aldrich, St. Louis, MO) solution in a 1.5 mL Eppendorf tube, for 5 mm cuvette (and 0.4 times the volume for 2 mm cuvette). The final CB nanoparticle concentration became 26.3 mg/L, 52.6 mg/L or 65.75 mg/L and dextran concentration became 98 mg/L. Samples were stored in ice bath to reduce endocytosis/cellular activity before and after-laser exposure.

C.1.4 Laser exposure and cell wash

Cell samples were transferred to either a 2 mm or 5 mm long and 21 mm diameter cylindrical Pyrex glass cuvette (37-PX-5, Starna Cells, Atascadero, CA). An Nd:YAG solid-state laser (Continuum Powerlite II Plus, Continuum, San Jose, CA) was used as laser source to apply 5-9 ns pulses of 1064 nm wavelength at a frequency of 10 Hz. Samples were exposed to laser beam (21 mm diameter), which irradiated the whole surface with flat top (uniform) energy profile. Immediately after exposure, samples were transferred back to the Eppendorf tubes and stored in ice. Negative controls in the form of 'sham' exposures were samples containing cells, CB nanoparticles, and dextran that experienced the same handling and procedures except the laser exposure. To label non-viable cells post laser-irradiation, PI (Invitrogen, Grand Island, NY) was added at a final concentration of 13.4 μM for 10 min on ice. Cell samples were then washed 3 times with phosphate buffer saline (PBS) to remove excess dextran from the bulk solution before analysis.

C.1.5 Data collection

Cells were analyzed using a bench-top flow cytometer (BD Accuri, BD Biosciences, San Jose, CA) to quantify bio-effects in terms of viable cells with intracellular uptake and non-viable cells (i.e. intact cells with PI staining). FITC-labelled dextran fluorescence was measured using 530/28 nm bandpass filter with excitation at 488 nm and PI fluorescence was measured using a 670 nm longpass filter with excitation at 535 nm. Cell samples were run at constant flow rate of 35 μL/min for 1 min. A negative control containing only cells in RPMI was used to construct a cell population gate in the forward-scattered (FSC) and side-scattered (SSC) analysis. Cells within this gate were considered to be intact cells. To account for possible cell loss due to cell fragmentation (appearing as low forward scatter and low side scatter events on the flow cytometer), the difference between the number of viable cells detected in a given sample and the number of viable cells detected in sham samples was taken as the number of cells lost to fragmentation.

C.1.6 Data Analysis

A minimum of 3 replicates were used for each experimental condition. Mean and standard error of the mean were calculated using the 3 replicates. One-way analysis of variance (ANOVA, $\alpha = 0.05$) was performed to compare 3 or more experimental conditions using Graphpad Prism 8 (GraphPad Software, La Jolla, CA) followed by post-hoc Tukey's pairwise comparison. A value of $p < 0.05$ was considered statistically significant.

C.2 Results and discussions

C.2.1 Macromolecular delivery using 195 nm or 243 nm CB nanoparticles and 2mm or 5 mm glass cuvette with cells suspended in RPMI

Suspensions containing 65.75 mg/L CB nanoparticles of diameter 195 nm and 243 nm, cells and 2000 kDa dextran molecules were placed inside 2mm and 5mm wide glass cuvettes. These were then irradiated with laser pulses at 29 mJ/cm^2 for variable amounts of time. Figure C.1 shows bio-effects for each of these subsets at different exposure durations. When cells were suspended with 195 nm CB nanoparticles, total percentage of cells affected appear to increase with increasing exposure durations (i.e. number of pulses) for both the cuvettes used (Figure C.1a and b). Consequently, the percentage of cells with 2000 kDa dextran uptake also increased with increasing exposure duration (one-way ANOVA, $p < 0.0001$). However, percentage of fragmented cells were always greater in 2 mm cuvettes than 5 mm cuvette at any given exposure condition. For example, when cells were irradiated with laser pulses for 5 min, ~21% cells were fragmented in 2mm cuvettes

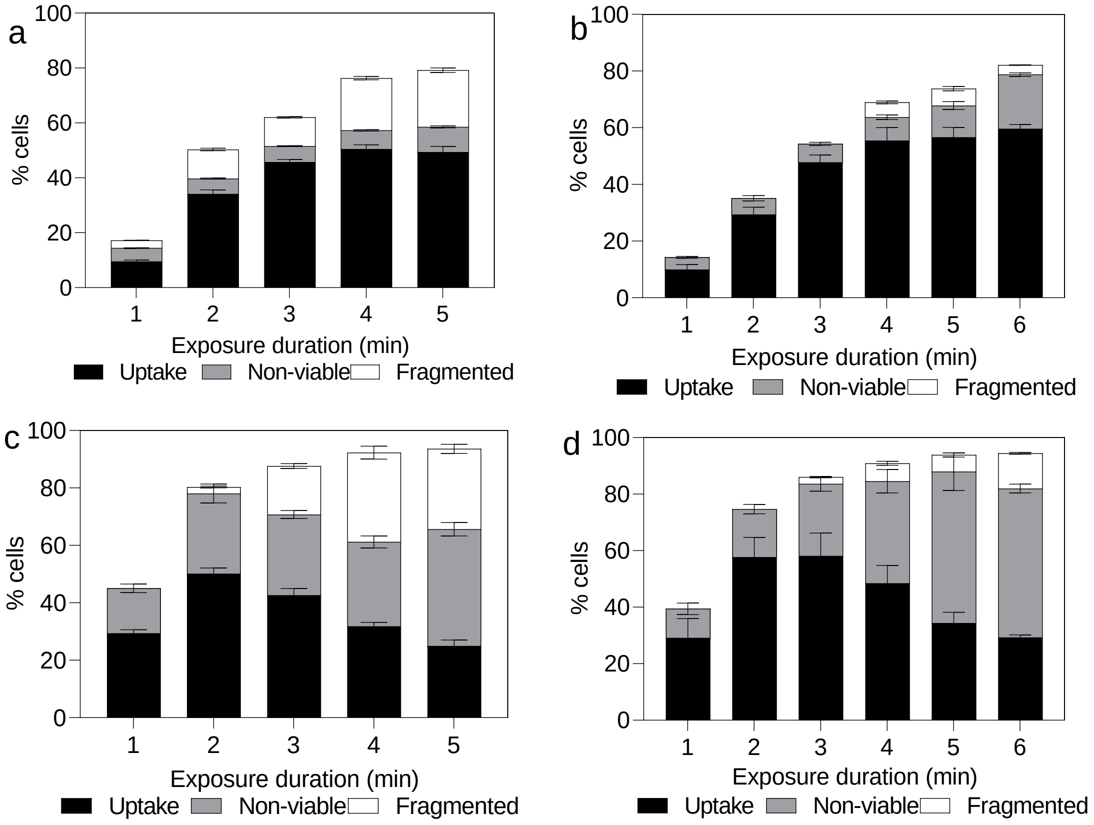

Figure C.1: Bio-effects plot for delivery of 2000 kDa dextran using 29 mJ/cm^2 fluence, 26.3 mg/L CB nanoparticles, a) 200 nm CB nanoparticles using 2 mm cuvette, b) 200 nm CB nanoparticles using 5 mm cuvette, c) 243 nm CB nanoparticles using 2 mm cuvette, d) 243 nm CB nanoparticles using 5 mm cuvette; with varying exposure duration. Data are expressed as mean ± SEM based on 3 replicates each.

compared to ~6% cell fragmentation in 5 mm cuvette ($p < 0.0001$). This suggests higher bio-effects in 2 mm cuvettes compared to 5 mm cuvettes.

Further, when cells were suspended with 243 nm CB nanoparticles, total percentage of cells affected trend differently than in the case of 195 nm CB nanoparticles (Figure C.1c and d). For both the cuvette widths, total percentages of cells affected increased when exposure duration was varied from 1 min to 3 min (one-way ANOVA, $p < 0.0.001$) and then saturated with further increase in exposure durations (one-way ANOVA, $p > 0.05$).

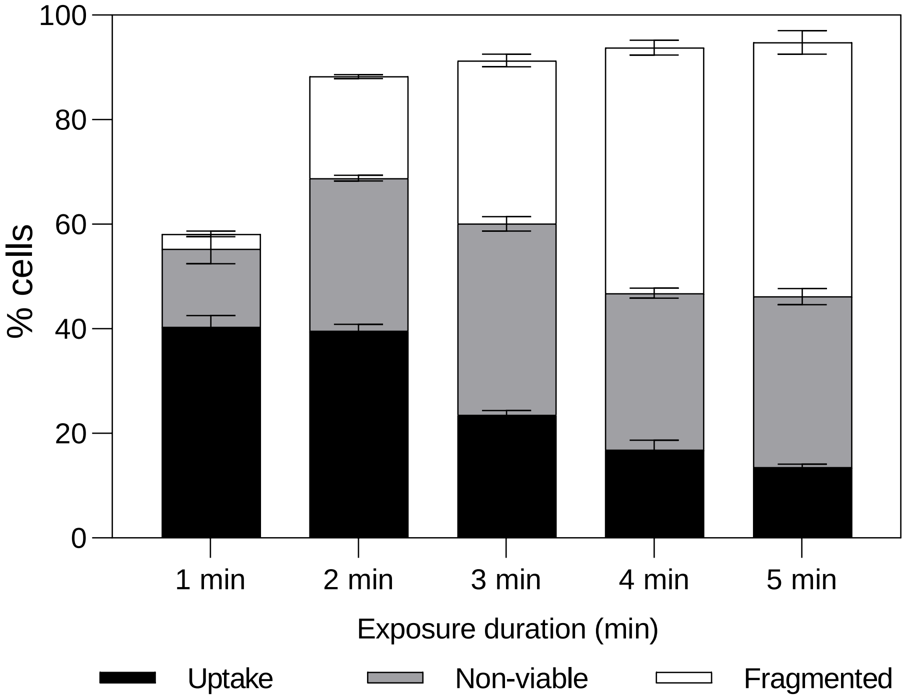

Figure C.2: Bio-effects plot for delivery of 2000 kDa dextran at 33 mJ/cm^2 fluence using 26.3 mg/L 243 nm CB nanoparticles and 5 mm cuvette for varying exposure duration. Data are expressed as mean ± SEM based on 3 replicates each.

Additionally, percentage of cells with 2000 kDa dextran uptake reached maximum at 2 min exposure, after which it showed a decreasing profile with increase in exposure duration for both the cuvette widths. However, cell viability loss continued to increase with increasing exposure duration (one-way ANOVA, $p < 0.001$). Similar to 195 nm CB nanoparticles, cells placed inside 2 mm cuvette faced greater bio-effects than the ones in 5 mm cuvette. Comparing both the nanoparticles sizes, 243 nm CB nanoparticles had greater bio-effects than 195 nm CB nanoparticles at similar exposure conditions. One possible reason for such behaviour could be that 243 nm store higher amount of energy per nanoparticles and thus form bigger bubbles than 195 nm nanoparticles, even though the total energy absorbed for both the cases would be almost equal. Formation of bigger bubbles might have caused greater bio-effects. Overall, highest percentage of cells with 2000 kDa uptake were ~60% and ~59% (no significant difference, $p > 0.05$) for 195 nm

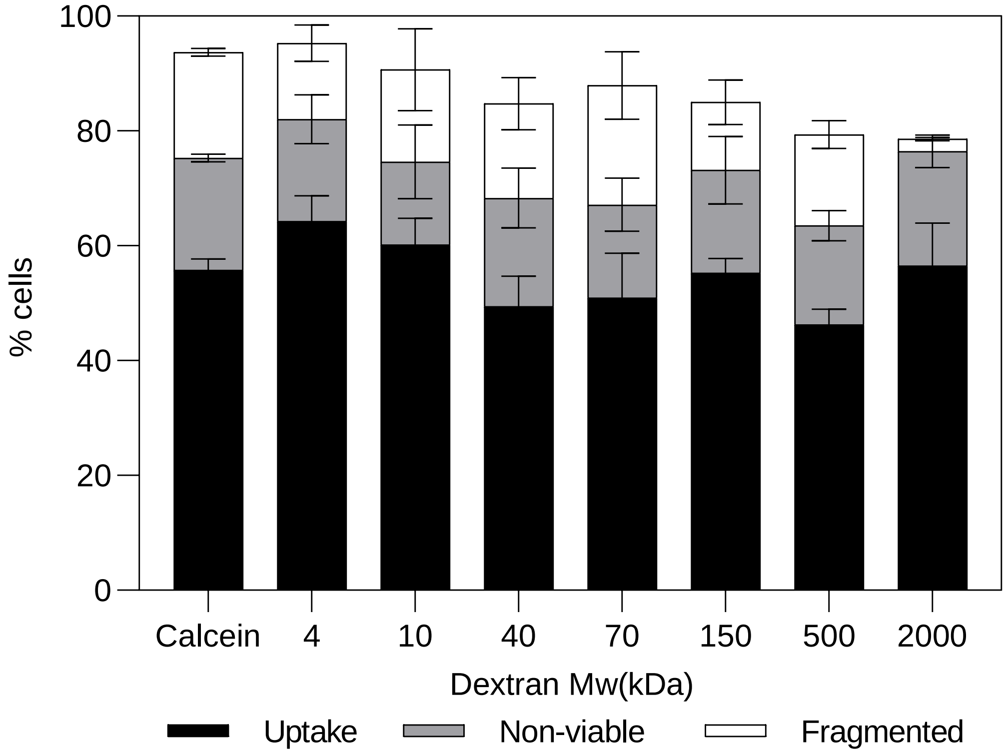

Figure C.3: Bio-effects plot for delivery of 4 kDa to 2000 kDa dextran at 29 mJ/cm^2 fluence for 4 min exposure using 65.75 mg/L 243 nm CB nanoparticles and 5 mm cuvette. Data are expressed as mean ± SEM based on 3 replicates each.

and 243 nm CB nanoparticle respectively. In both the cases, highest uptake percentages were achieved using 5 mm cuvettes. An additional experiment using 243 nm CB nanoparticles and 5 mm cuvette at 33 mJ/cm^2 showed higher bio-effects compared to 29 mJ/cm^2 but the percentage of uptake cells were always $< 40\%$ (Figure C.2).

Finally, we performed laser irradiation experiments using 243 nm CB nanoparticles, 5 mm cuvette at 29 mJ/cm^2 for 4 min exposure and found percentage of uptake cells to be $> 45\%$ for each of the different molecular weight dextran (Figure C.3). In addition, no significant differences were seen in total bio-effects for any of the delivery molecules (one-way ANOVA, $p > 0.05$).

C.2.2 Macromolecular delivery using 243 nm CB nanoparticles and 5 mm glass cuvette with cells suspended in 1 wt/vol% Pluronic F127

Pluronic F127 showed significant viability protection against cell damage in our previous studies. For this section, we conducted experiments to deliver 150 kDa, 500 kDa and 2000 kDa dextran using 243 nm CB nanoparticles and 5 mm cuvette in the presence of 1% F127 in cell suspension media. Our hypothesis was that using 1% F127 in suspension media, we can significantly improve macromolecular delivery efficiency compared to the case when cells are suspended in RPMI only.

Data in Figure C.4 shows bio-effects for 150 kDa dextran delivery at 33 mJ/cm^2 for variable exposure duration (i.e. number of pulses). At any given exposure duration, percentage of cells with 150 kDa dextran uptake were significantly higher for cells suspended in 1% F127 compared to RPMI only ($p < 0.0001$). However, percentage of

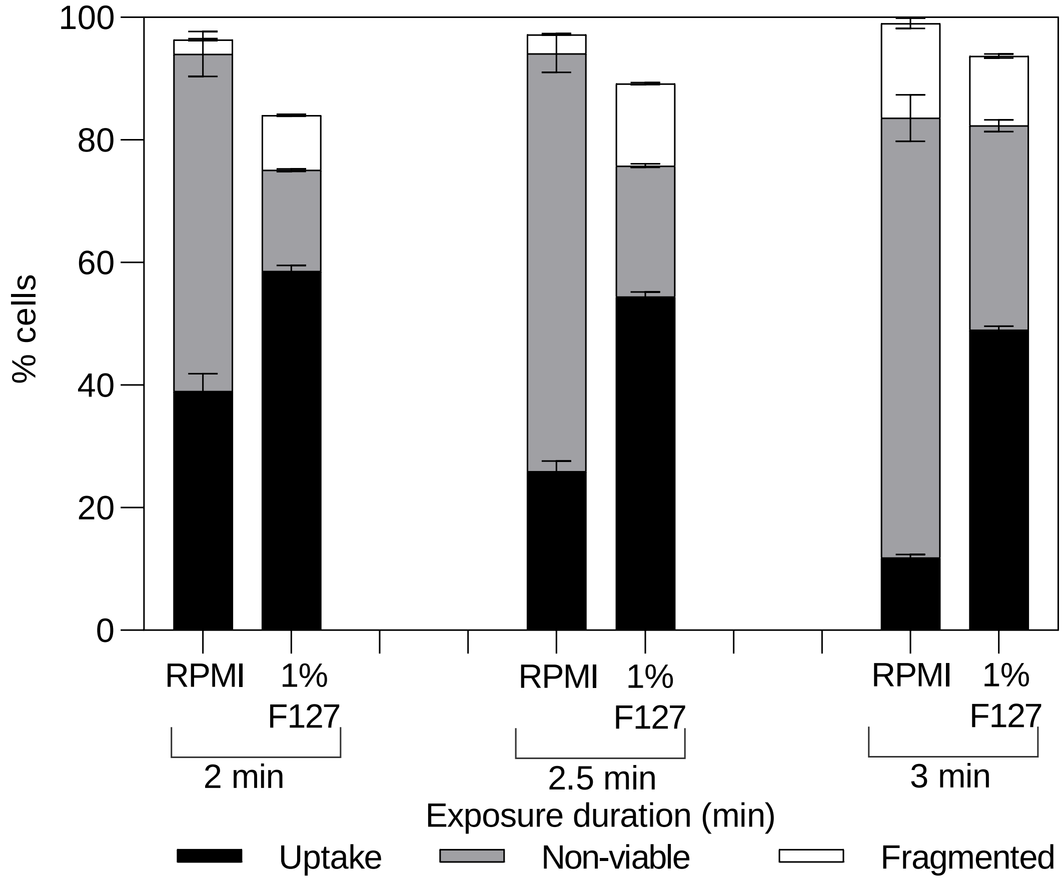

Figure C.4: Bio-effects plot for delivery of 150 kDa dextran using 33 mJ/cm^2 fluence, 52.6 mg/L CB nanoparticles with varying exposure duration. Data are expressed as mean ± SEM based on 3 replicates each.

uptake cells decreased with the increase in exposure duration (one-way ANOVA, $p < 0.0001$), while percentage of viable loss increased, for both the cases (one-way ANOVA, $p < 0.0001$). Overall, highest delivery efficiency was observed (~59%) for 2 min exposure when cells were suspended in 1% F127 media.

Once we confirmed that adding 1% F127 was beneficial for enhancing 150 kDa dextran molecule delivery efficiency, we performed photoporation experiments to deliver 500 kDa and 2000 kDa dextran molecules as well. Figure C.5 shows bio-effects plots for each of these delivery molecules at 33 mJ/cm^2 and varying exposure durations. Although we were successful in delivering 150 kDa and 500 kDs dextran to more 50% of cells, the percentage of cells with 2000 kDa dextran uptake remained lower than 30%. A possible reason could be lower diffusivity value for 2000 kDa molecules, limiting uptake percentages.

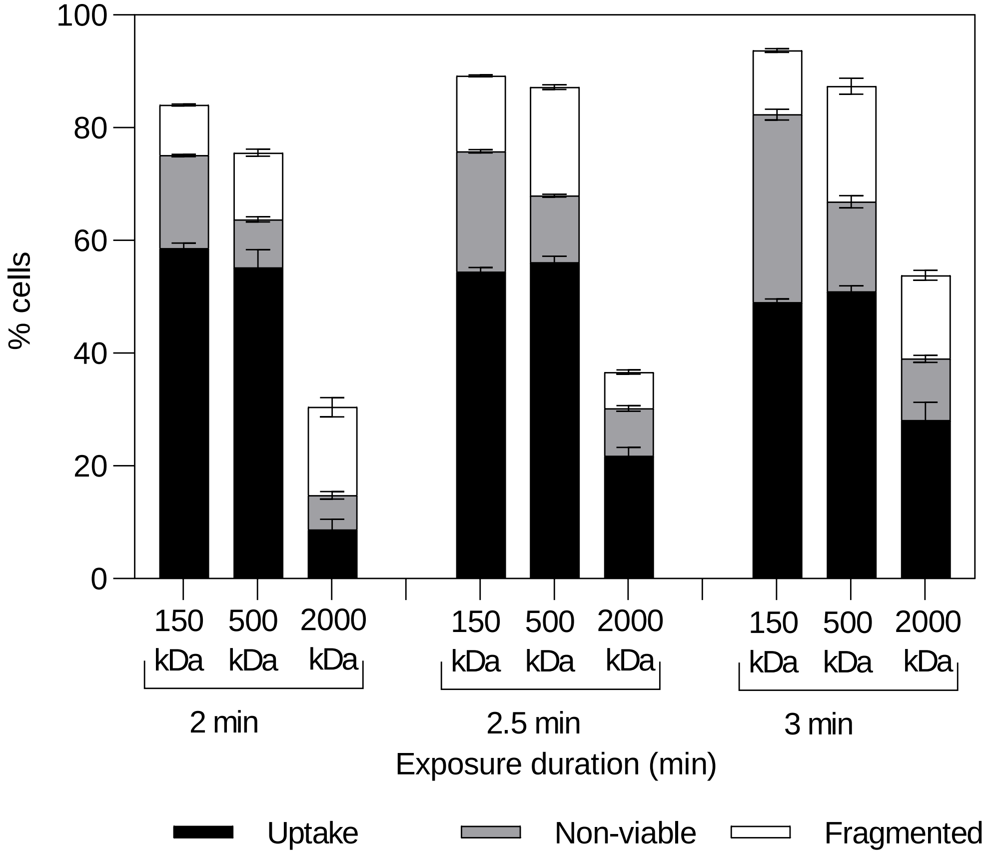

Figure C.5: Bio-effects plot for delivery of 150 kDa, 500 kDa and 2000 kDa dextran using 33 mJ/cm^2 fluence, 52.6 mg/L CB nanoparticles with varying exposure duration. Data are expressed as mean ± SEM based on 3 replicates each.

To improve 2000 kDa delivery efficiency, we increased laser fluence and varied exposure duration, in presence of 1% F127. Data in Figure C.6 shows bio-effects at 33 –

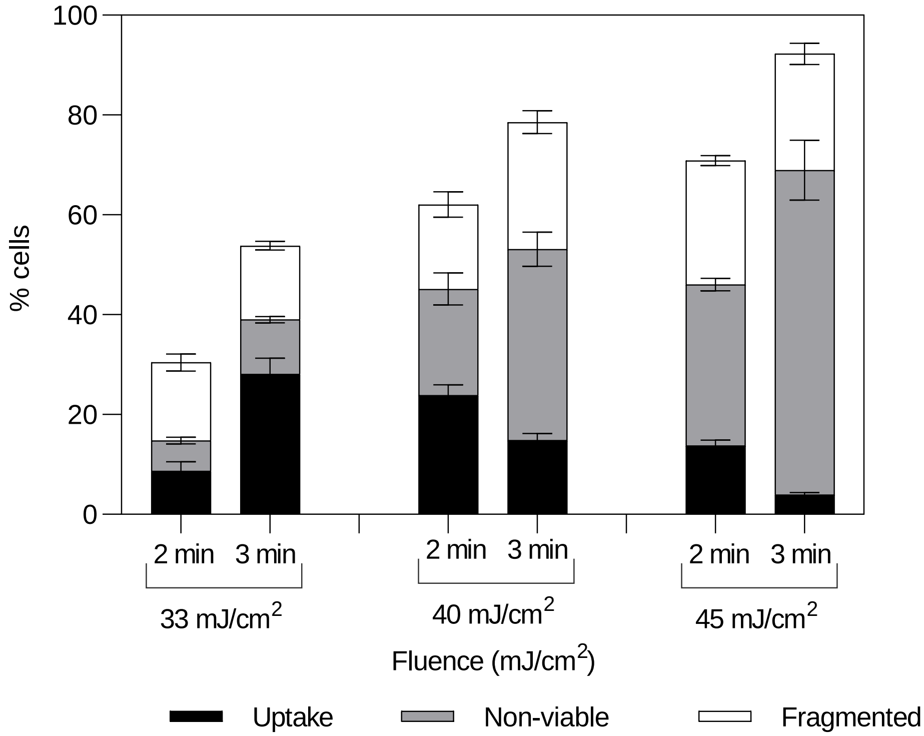

Figure C.6: Bio-effects plot for delivery of 2000 kDa dextran using varying fluence, 52.6 mg/L CB nanoparticles with exposure duration of 2 min and 3 min. Data are expressed as mean ± SEM based on 3 replicates each.

45 mJ/cm^2 fluence. Increasing laser fluence does increase the total bio-effects but fails to increase percentage of uptake cells above 30%. Highest uptake was seen for 3 min exposure at 33 mJ/cm^2 and any further increase in fluence at this exposure duration lead to higher viability loss instead of increasing uptake percentage. These results suggested that we might need to increase exposure duration instead of laser fluence to improve the 2000 kDa delivery efficiency.

Therefore, in the next study, we further increased exposure duration at 33 mJ/cm^2 fluence. Data in Figure C.7a shows that percentage of uptake cells increased when exposure duration was changed to 3.5 min ($p < 0.05$) but no significant difference was observed between 3.5 min and 4 min ($p > 0.05$).

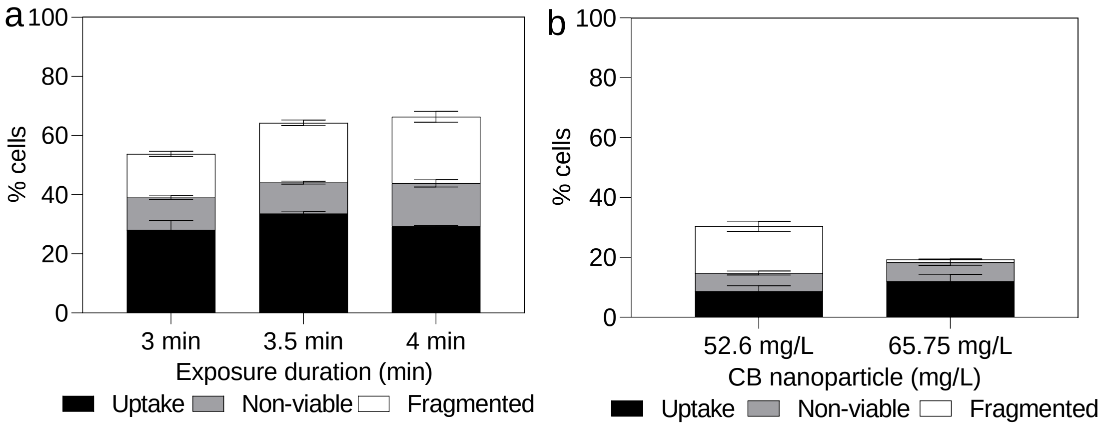

Figure C.7: Bio-effects plot for delivery of 2000 kDa dextran using 33 mJ/cm^2 fluence a) 52.6 mg/L CB nanoparticles and variable exposure duration, and b) 52.6 and 65.75 mg/L CB nanoparticles and 2 min exposure. Data are expressed as mean ± SEM based on 3 replicates each.

On the other hand, percentage of viable cells continued to decrease with increase in exposure duration (one-way ANOVA, $p < 0.001$). This suggested that uptake percentage had reached its maximum at 3.5 min and further increase would only lead to viability loss without increase in uptake percentage of 2000 kDa dextran. An attempt to improve uptake percentage by increasing CB nanoparticle concentration also did not cause any significant increase in 2000 kDa uptake ($p > 0.05$, Figure C.7b).

C.3 Conclusion

Comparative studies between two different sized nanoparticles showed that 243 nm CB nanoparticles caused more bio-effects (which lead to higher uptake cell percentage in some cases). On the other hand, 2 mm cuvette width had higher bio-effects than 5 mm cuvette. Greater power loss in cuvette path length could be one of the reasons for such observation. Overall, we demonstrated that > 45% cells with macromolecular delivery of > 100 kDa in size. It is important to mention that we can individually optimize the delivery efficiencies, which would mean different operating conditions for different molecular weight. We also showed that viability loss during nanoparticle-mediated photoporation can be reduced with Pluronic F127 addition in cell suspension media. We were able to enhance percentage of cells with 150 kDa and 500 kDa molecules to more than 50%, however, same could not be achieved for 2000 kDa molecule in presence of Pluronic F127. Therefore, to conclude, we showed that we can achieve better macromolecular delivery efficiency using 243 nm CB nanoparticles and 5 mm cuvette, while reduce viability loss and improve percentage of uptake cells using Pluronic F127.

APPENDIX D. SUPPLEMENTARY MATERIAL FOR CHAPTER 3

D.1 Methods to calculate physical properties used to calculate nanoparticle, energy absorption and energy transduction parameters

The equations used to determine physical properties are shown below, along with example calculations. For those calculations, the following values were used:

a) CB particle diameter: 25 nm (also referred to as carbon spheres)

b) CB nanoparticles dispersion aggregate diameter: 195 nm (radius of the aggregates formed in dispersion phase)

c) Cuvette width: 2 mm

d) Cuvette diameter: 21 mm

e) CB nanoparticle sample concentration: $1.6 * 10^{-3}\ \frac{kg}{L}$

f) Volume of solution in cuvette: $5.625 * 10^{-7}\ m^3$

g) Radius of cuvette: $0.011\ m$

h) Laser fluence: $88\ \frac{mJ}{cm^2}$

i) Bulk density of CB: $1800\ \frac{kg}{m^3}$

j) Porosity of CB: 0.7667

k) Index of Refraction of media (water) = 1.33

l) Carbon Refractive Index = 2-0.29i[216]

Calculation methods with examples:

Total Volume of Carbon:

$$\frac{Sample\ Concentration * Volume\ of\ Solution}{Density\ of\ Carbon}$$

$$\frac{1.6 * 10^{-3}\ \frac{kg}{L} * 5.625 * 10^{-7}\ m^3}{1800\ \frac{kg}{m^3}} = 5 * 10^{-13}\ m^3$$

Total Number of CB Particles:

$$\frac{Total\ Volume\ of\ Carbon}{Volume\ of\ Each\ Carbon\ Particle}$$

$$\frac{5 * 10^{-13}\ m^3}{\frac{4}{3}\pi(1.25 * 10^{-8}\ m)^3} = 6.11 * 10^{10}$$

Total CB Particles in an aggregate:

$$\frac{(1 - Porosity) * Volume\ of\ one\ aggregate}{Volume\ of\ Each\ Carbon\ particle}$$

$$\frac{(1 - 0.7667) * \frac{4}{3}\pi(9.78 * 10^{-8}\ m)^3}{\frac{4}{3}\pi(1.25 * 10^{-8}\ m)^3} = 111.7$$

Total Number of CB nanoparticle aggregates:

$$\frac{Total\ Number\ of\ Carbon\ particles}{Total\ Carbon\ particles\ in\ an\ aggregate}$$

$$\frac{6.11 * 10^{10}}{111.7} = 5.46 * 10^{8}$$

An online calculator[217] was used to calculate Mie scattering data which yields: scattering cross section (SCS), backscattering cross section (BCS), and extinction cross section (ECS) for each CB particle sphere. Using the output generated, total scattering area can be calculated as

Total Scattering Cross Section Area: $SCS + BCS$

$$1.27 * 10^{-20}\ m^2 + 1.90 * 10^{-20}\ m^2 = 3.17 * 10^{-20}\ m^2$$

Then, the total absorption area of CB particle is calculated as

Area absorbed by each Carbon particle: $ECS - Total\ Scattering\ Area$

$$2.096 * 10^{-17}\ m^2 - 3.17 * 10^{-20}\ m^2 = 2.093 * 10^{-17}\ m^2$$

This area absorbed value is for 1 CB particle. However, the CB nanoparticle dispersion contains multiples of these particles. Therefore, we calculated total absorption area of all the CB particles in dispersion (for a 1.6 mg/L dispersion) as:

$$Total\ Number\ of\ Carbon\ particles * Area\ Absorbed\ for\ each\ carbon\ particle$$

$$6.11 * 10^{10} * 2.093 * 10^{-17}\ m^2 = 1.279 * 10^{-6}\ m^2$$

If we divide total absorption area of all CB particle the total area of the cuvette, which the laser passes through, we can get the percentage of energy absorbed (which is dependent on ratio of the area used for absorption) from the laser beam that irradiates the whole cuvette surface area:

$$\frac{Total\ absorption\ area\ of\ CB\ particles\ in\ dispersion}{Area\ of\ Cuvette}$$

$$\frac{1.279 * 10^{-6}\ m^2}{\pi(0.011\ m)^2} = 0.00336$$

Similarly, we can calculate the percentage of scattered energy as:

$$\frac{Total\ Number\ of\ Carbon\ particles * Total\ Carbon\ particles\ in\ one\ aggregate * Total\ Scattering\ Energy}{Area\ of\ Cuvette}$$

$$\frac{6.11 * 10^{10} * 111.7 * 3.17 * 10^{-20}\ m^2}{\pi(0.011\ m)^2} = 5.69 * 10^{-4}$$

Therefore, using percentage of energy absorbed, the total energy (Q) absorbed by the carbon is:

$$Area\ of\ Cuvette * Fluence * Percent\ Energy\ Absorbed$$

$$\pi(0.011\ m)^2 * 880000\ \frac{mJ}{m^2} * 0.00336 = 1.12\ mJ$$

We can relate energy absorbed to number of moles of water evaporated (using heat balance):

$$Q = m_{CB}c_{pCB}\Delta T + n_{H2O}(c_{pH2O}\Delta T + \Delta H_{vapH2O})$$

$$.00112\,J = (37 * 10^{-6}\,L * 1.6\frac{g}{L} * \frac{562.5\,\mu L}{37\,\mu L})\left(0.7\frac{J}{g\,℃}\right)(100℃ - 23℃)$$

$$+ n_{H2O}((4.184\ \frac{J}{g\,℃}(100℃ - 23℃) +\ 2260\ \frac{J}{g})$$

$$n_{H2O} = 4.17 * 10^{-7}g$$

We can then find the amount of water evaporated per nanoparticle:

$$\frac{n_{H2O} * Specific\,Volume\,of\,Water}{Total\,Number\,of\,Aggregates}$$

$$\frac{4.17 * 10^{-7}g * 0.00167\frac{m^3}{g}}{5.46 * 10^8} = 1.28 * 10^{-18}\,m^3$$

Determine peak bubble radius

To find the radius of each bubble + nanoparticle aggregate:

$$((Volume\ water\ per\ nanoparticle + Volume\ of\ each\,nanoparticle) * \frac{3}{4\pi})^{\frac{1}{3}}$$

$$r = (\left(1.28 * 10^{-18}\,m^3 + \frac{4}{3}\pi(9.78 * 10^{-8}\,m)^3\right) * \frac{3}{4\pi})^{\frac{1}{3}} =\ 6.74 * 10^{-7}\,m$$

Determine peak bubble size

To find the how big the bubble grows from the nanoparticle:

$$(Radius\ of\ each\ bubble + nanoparticle) - (Radius\ of\ carbon\ black\ disperion)$$

$$(6.74 * 10^{-7}\,m) - (9.78 *\ 10^{-8}) = 5.74 * 10 * 10^{-7}\,m$$

Determine peak nanoparticle temperature

Peak nanoparticle temperature was calculated using energy absorbed through heat balance-

$$T_{final} = T_{initial} + \frac{Q}{m_{CB} * c_{pCB}}$$

$$T_{final} = 20\,℃ + \frac{0.00112\,J}{(1.6\,\frac{g}{L} * 562.5 * 10^{-9} L * 0.7 \frac{J}{g\,℃})} = 1798\,℃$$

Determine CB nanoparticle refractive index

Since a CB nanoparticle is an aggregate of smaller CB particles with water filling the spaces in between, we need to account for role played by water present in CB nanoparticle aggregate pores on refractive index during laser – nanoparticle interaction[218,219]. Generally -

Dielectric function is presented as $\varepsilon = \varepsilon' + i\varepsilon''$

Refractive index of a material $n^* = n + ik$

Dielectric function is related to refractive index as $(n^*)^2 = \varepsilon$

Therefore,

$$\varepsilon' = n^2 + k^2$$

$$\varepsilon'' = 2nk$$

To account for the porosity of the nanoparticle, effective dielectric constant is calculated as - effective dielectric function $\varepsilon_{av} = \varepsilon_m \frac{\varepsilon(1+2\emptyset)+2\varepsilon_m(1-\emptyset)}{\varepsilon(1-\emptyset)+\varepsilon_m(2+\emptyset)}$

where, ε_m is the medium dielectric constant (water), ε is the material dielectric constant (CB) and $\emptyset$ is the material volume fraction (1-porosity).

This allows us to calculate a new Refractive index as

$$n_{av}{}^2 = \frac{((\varepsilon'^2 + \varepsilon''^2) + \varepsilon')}{2}$$

$$k_{av}{}^2 = \frac{((\varepsilon'^2 + \varepsilon''^2) - \varepsilon')}{2}$$

For example, for 195 nm CB nanoparticles: $\emptyset = 0.23, n^* = 2 - i0.29, \varepsilon' = 4.0841, \varepsilon'' = -1.16$, aand $\varepsilon_{water} = 1.76 - i0.000005$

Therefore, $\varepsilon_{av} = 2.177 - i0.147$

And new CB refractive index becomes 1.476 – i0.05

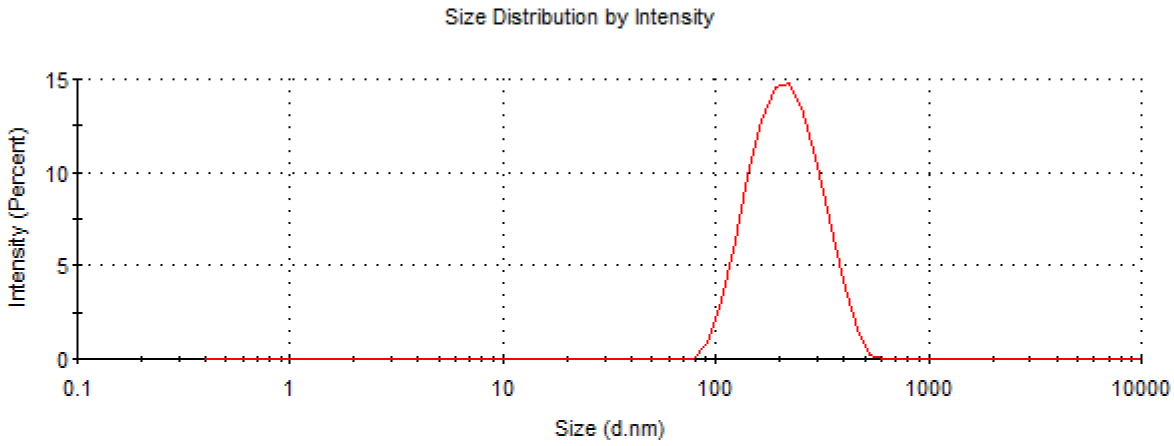

Figure D.1: DLS size distribution of CB nanoparticles showing a mean diameter of ~195 nm with a dispersity of 0.116 for 25 nm CB particles

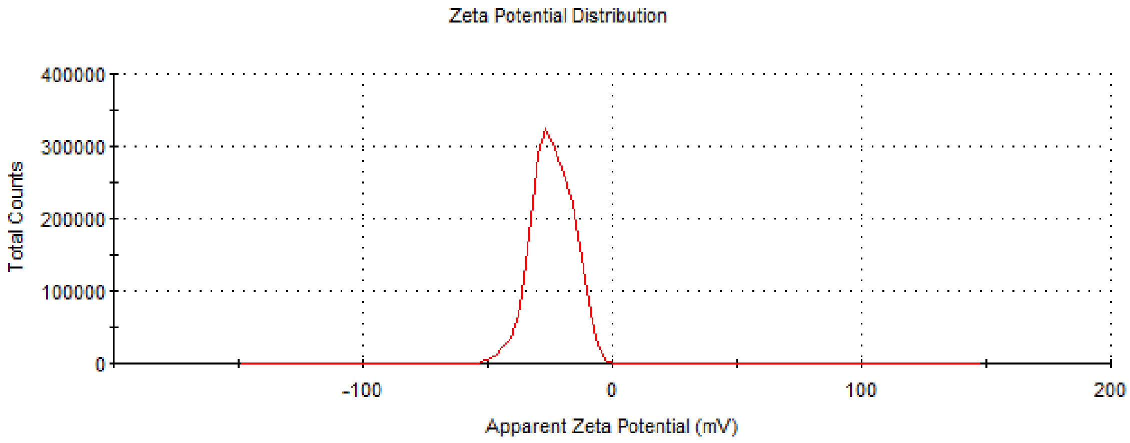

Figure D.2: Zeta potential distribution of CB nanoparticles showing a mean Zeta potential of -24 mV for 25 nm CB particles.

D.2 Bio-effects correlation plots

These plots were generated for 10 µM calcein delivery using 195, 367 and 507 nm CB nanoparticles for 1 min exposure (600 pulses) of 1064 nm laser beam in 2 mm glass cuvette, with cells suspended at 10^6/mL concentration.

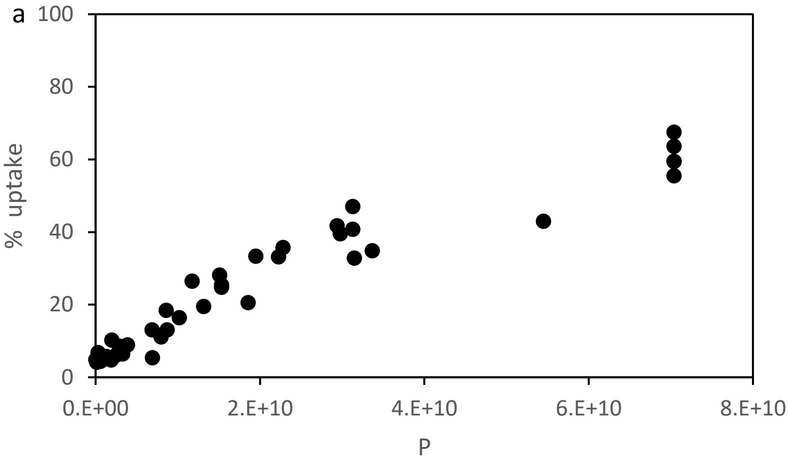

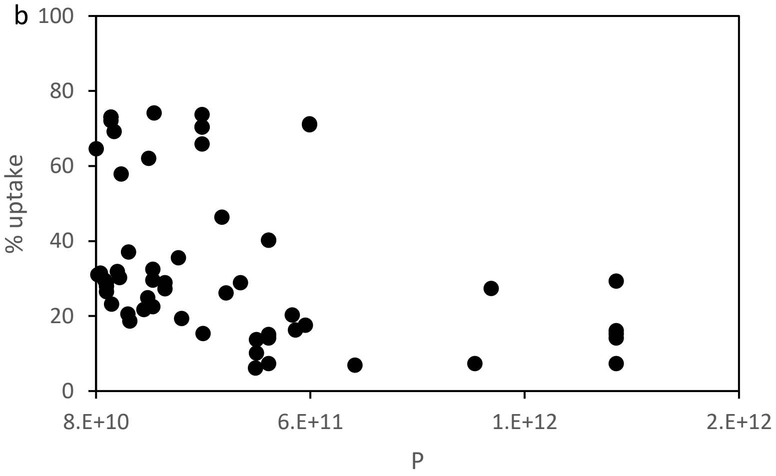

Figure D. 3: (a and b) Correlation between %uptake cells and parameter P. P is the product of (peak nanoparticle temperature)^2, (total number of bubbles)$^{0.5}$ and (peak bubble radius)$^{0.25}$

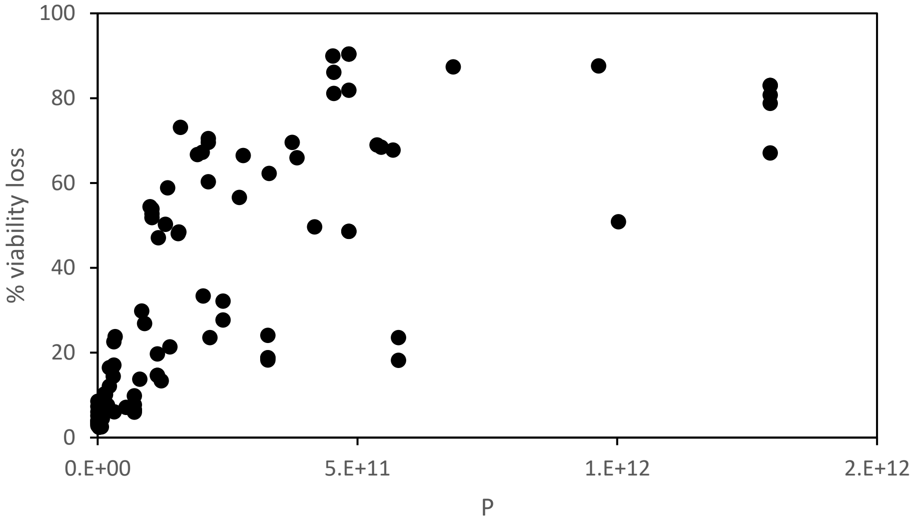

Figure D.4: Correlation between %viability loss (non-viable and fragmented) and parameter P. P is the product of (peak nanoparticle temperature)^2, (total number of bubbles)$^{0.5}$ and (peak bubble radius)$^{0.25}$

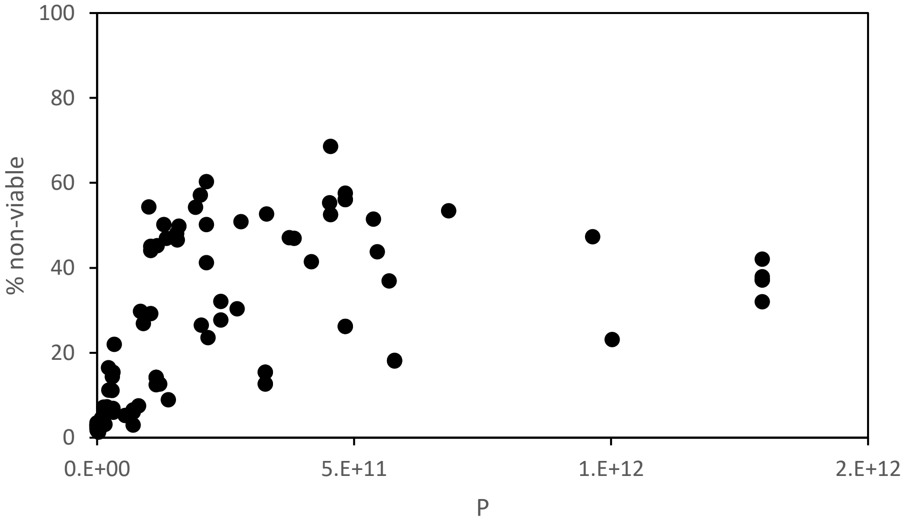

Figure D. 5: Correlation between %non-viable cells and parameter P. P is the product of (peak nanoparticle temperature)^2, (total number of bubbles)$^{0.5}$ and (peak bubble radius)$^{0.25}$

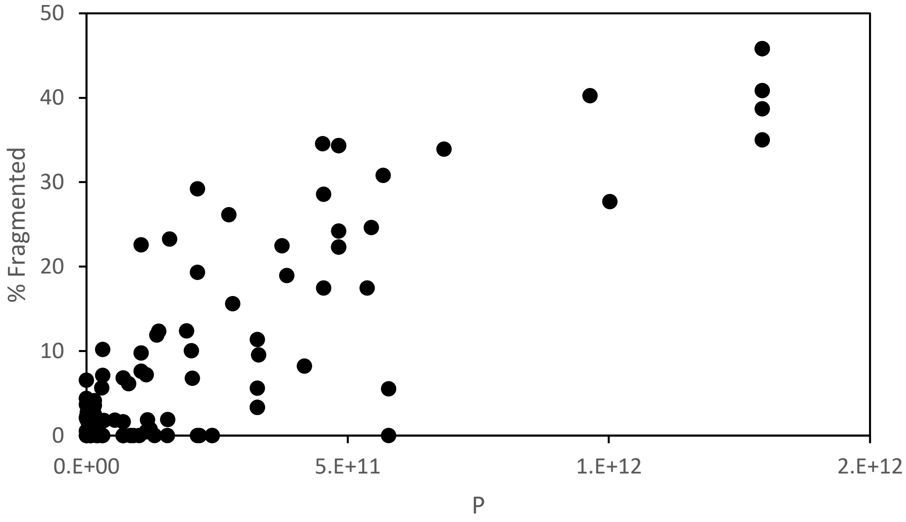

Figure D. 6: Correlation between %fragmented cells and parameter P. P is the product of (peak nanoparticle temperature)^2, (total number of bubbles)$^{0.5}$ and (peak bubble radius)$^{0.25}$

APPENDIX E. SUPPLEMENTARY MATERIALS FOR CHAPTER 4

E.1 Is viscosity change the reason behind viability protection ability of FBS?

Adding FBS in cell suspension media changes certain physical properties of suspension media. One such property that can alter bio-effects is viscosity change[9].

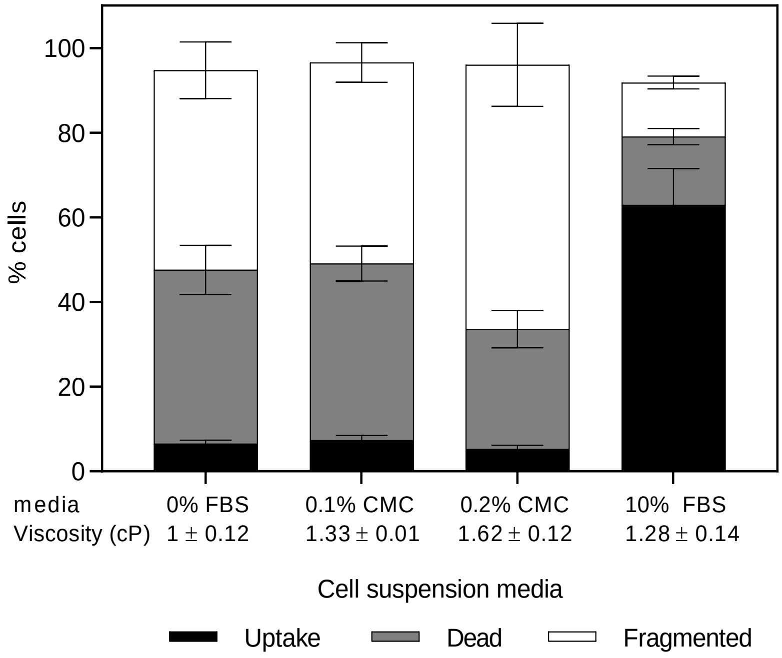

Figure E.1: Changes in bio-effects due to viscosity increase by adding CMC. Distribution of uptake cells, non-viable cells and fragmented cells with 0.1% w/v and 0.2% w/v CMC or 10% v/v FBS to DU145 cell suspension media during laser exposure. Laser exposure was carried out at a fluence of 88 mJ/cm^2 for 1 min. All samples contained 26.3 mg/L CB nanoparticles and 10 μM calcein. Viscosity was measured using viscometer at 25°C (Brookfield DV2T, Brookfield AMETEK, Middleboro, MA). Data are expressed as mean ± SEM based on ≥ 3 replicates each.

Matching the viscosity of media containing 10% FBS by adding 0.1% CMC does not appear to provide cell viability protection (non-significant difference between 0% FBS and

0.1% CMC, Tukey's multiple comparison tests, $p > 0.05$). Increasing the viscosity further by adding 0.2% CMC increased the percentage of fragmented cells (Tukey's multiple comparison tests, $p < 0.0001$), and therefore, cell viability protection offered by serum appears to be not caused by increment in cell suspension media viscosity.

E.2 Temperature rise in the presence of viability protection additives

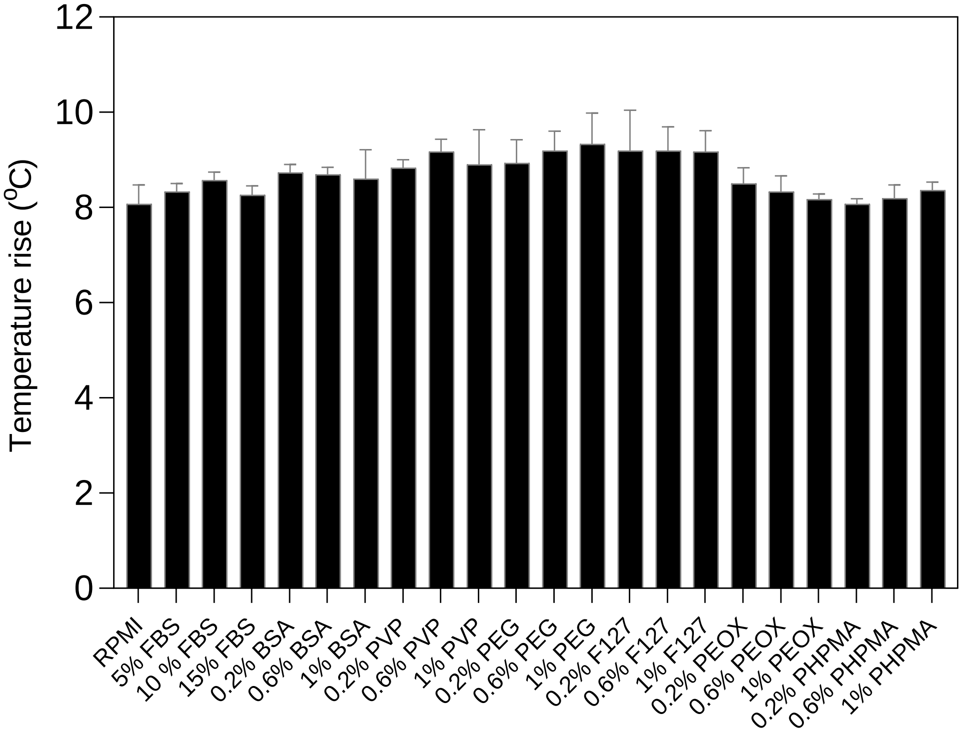

Figure E.2: Changes in bulk -temperature rise measured for various additives. All samples contained 26.3 mg/L CB nanoparticles and 10 µM calcein, and were exposed to laser pulses for 1 min at 55 mJ/cm^2 laser fluence. The starting temperature was ambient conditions (i.e., 20 – 25 °C) and the temperature was measured using a standard J-type thermocouple. Data are expressed as mean ± SEM based on ≥ 3 replicates each

We measured cell suspension media’s temperature rise due to laser exposure, to check if these additives affect the absorbance or energy dissipation properties of either nanoparticles or suspension media itself. No significant difference was observed in any of the cases (using Tukey’s post-hoc multiple comparison tests, $p > 0.05$) measured implying that these parameters are not affected due to polymer or serum addition and thus are also not responsible for cell-viability protection.

REFERENCES

[1] R.C.C. Ryther, A.S. Flynt, J.A. Phillips, J.G. Patton, siRNA therapeutics: Big potential from small RNAs, Gene Ther. 12 (2005) 5–11. https://doi.org/10.1038/sj.gt.3302356.

[2] A. Wittrup, J. Lieberman, Knocking down disease: a progress report on siRNA therapeutics, Nat. Rev. Genet. 16 (2015) 543–552. https://doi.org/10.1038/nrg3978.

[3] C. Huang, M. Li, C. Chen, Q. Yao, Small interfering RNA therapy in cancer: Mechanism, potential targets, and clinical applications, Expert Opin. Ther. Targets. 12 (2008) 637–645. https://doi.org/10.1517/14728222.12.5.637.

[4] A. Pfeifer, I.M. Verma, Gene Therapy : Promises and Problems, Annu. Rev. Genomics Hum. Genet. 2 (2001) 177–211. https://doi.org/10.1146/annurev.genom.2.1.177.

[5] N. Desai, Challenges in Development of Nanoparticle-Based Therapeutics, AAPS J. 14 (2012) 282–295. https://doi.org/10.1208/s12248-012-9339-4.

[6] P. Chakravarty, W. Qian, M.A. El-Sayed, M.R. Prausnitz, Delivery of molecules into cells using carbon nanoparticles activated by femtosecond laser pulses, Nat. Nanotechnol. 5 (2010) 607–611. https://doi.org/10.1038/nnano.2010.126.

[7] A. Sengupta, M.D. Gray, S.C. Kelly, S.Y. Holguin, N.N. Thadhani, M.R. Prausnitz, Energy Transfer Mechanisms during Molecular Delivery to Cells by Laser-Activated Carbon Nanoparticles, Biophys. J. 112 (2017) 1258–1269. https://doi.org/10.1016/j.bpj.2017.02.007.

[8] A. Sengupta, Intracellular Drug Delivery Using Laser Activated Carbon Nanoparticles, 2014.

[9] S.Y. Holguin, N.N. Thadhani, M.R. Prausnitz, Effect of laser fluence, nanoparticle concentration and total energy input per cell on photoporation of cells, Nanomedicine Nanotechnology, Biol. Med. 14 (2018) 1667–1677. https://doi.org/10.1016/j.nano.2018.04.015.

[10] S.Y. Holguin, C.F. Anderson, N.N. Thadhani, M.R. Prausnitz, Role of cytoskeletal

mechanics and cell membrane fluidity in the intracellular delivery of molecules mediated by laser-activated carbon nanoparticles, Biotechnol. Bioeng. 114 (2017) 2390–2399. https://doi.org/10.1002/bit.26355.

[11] A. Sengupta, R. Mezencev, J.F. McDonald, M.R. Prausnitz, Delivery of siRNA to ovarian cancer cells using laser-activated carbon nanoparticles., Nanomedicine (Lond). 10 (2015) 1775–84. https://doi.org/10.2217/nnm.15.27.

[12] A. Sengupta, S.C. Kelly, N. Dwivedi, N. Thadhani, M.R. Prausnitz, Efficient Intracellular Delivery of Molecules with High Cell Viability Using Nanosecond-Pulsed Laser- Activated Carbon Nanoparticles, ACS Nano. (2014) 2889–2899. https://doi.org/10.1021/nn500100x.

[13] S.Y. Holguin, M.D. Gray, P. Joseph, N.N. Thadhani, M.R. Prausnitz, Photoporation Using Carbon Nanotubes for Intracellular Delivery of Molecules and Its Relationship to Photoacoustic Pressure, Adv. Healthc. Mater. 7 (2018). https://doi.org/10.1002/adhm.201701007.

[14] K.T. Kunas, E.T. Papoutsakis, Increasing serum concentrations decrease cell death and allow growth of hybridoma cells at higher agitation rates, Biotechnol. Lett. 11 (1989) 525–530. https://doi.org/10.1007/BF01040029.

[15] R. Tippett, Mortality and Cause of Death, 1900 v. 2010, Heal. Environ. (2014).

[16] L.J. Su, H.H. Lin, M.S. Wu, L. Pan, K. Yadav, H.H. Hsu, T.Y. Ling, Y.T. Chen, H.C. Chang, Intracellular Delivery of Luciferase with Fluorescent Nanodiamonds for Dual-Modality Imaging of Human Stem Cells, Bioconjug. Chem. 30 (2019) 2228–2237. https://doi.org/10.1021/acs.bioconjchem.9b00458.

[17] A. Kollmannsperger, A. Sharei, A. Raulf, M. Heilemann, R. Langer, K.F. Jensen, R. Wieneke, R. Tampé, Live-cell protein labelling with nanometre precision by cell squeezing, Nat. Commun. 7 (2016) 1–7. https://doi.org/10.1038/ncomms10372.

[18] C. Tu, L. Santo, Y. Mishima, N. Raje, Z. Smilansky, J. Zoldan, Monitoring protein synthesis in single live cancer cells, Integr. Biol. (United Kingdom). 8 (2016) 645–653. https://doi.org/10.1039/c5ib00279f.

[19] A. Paganin-Gioanni, E. Bellard, J.M. Escoffre, M.P. Rols, J. Teissié, M. Golzio, Direct visualization at the single-cell level of siRNA electrotransfer into cancer cells, Proc. Natl. Acad. Sci. U. S. A. 108 (2011) 10443–10447.

https://doi.org/10.1073/pnas.1103519108.

[20] F. Ma, Y. Li, B. Tang, C.Y. Zhang, Fluorescent Biosensors Based on Single-Molecule Counting, Acc. Chem. Res. 49 (2016) 1722–1730. https://doi.org/10.1021/acs.accounts.6b00237.

[21] Thomas Gaj; Charles A. Gersbach and Carlos F. Barbas, ZFN, TALEN and CRISPR/Cas-based methods for genomeengineering, Trends Biotechnol. 31 (2013) 397–405. https://doi.org/10.1016/j.tibtech.2013.04.004.ZFN.

[22] L. Warren, P.D. Manos, T. Ahfeldt, Y.H. Loh, H. Li, F. Lau, W. Ebina, P.K. Mandal, Z.D. Smith, A. Meissner, G.Q. Daley, A.S. Brack, J.J. Collins, C. Cowan, T.M. Schlaeger, D.J. Rossi, Highly efficient reprogramming to pluripotency and directed differentiation of human cells with synthetic modified mRNA, Cell Stem Cell. 7 (2010) 618–630. https://doi.org/10.1016/j.stem.2010.08.012.

[23] K. Kelley, S.L. Lin, Induction of somatic cell reprogramming using the microRNA miR-302, 1st ed., Elsevier Inc., 2012. https://doi.org/10.1016/B978-0-12-398459-3.00004-6.

[24] D. Kim, C.H. Kim, J. Il Moon, Y.G. Chung, M.Y. Chang, B.S. Han, S. Ko, E. Yang, K.Y. Cha, R. Lanza, K.S. Kim, Generation of Human Induced Pluripotent Stem Cells by Direct Delivery of Reprogramming Proteins, Cell Stem Cell. 4 (2009) 472–476. https://doi.org/10.1016/j.stem.2009.05.005.

[25] S.J. Singer, G.L. Nicolson, The Fluid Mosaic Model of the Structure of Cell Membranes, Science (80-.). 175 (1972) 720 LP – 731. https://doi.org/10.1126/science.175.4023.720.

[26] G.L. Nicolson, The Fluid - Mosaic Model of Membrane Structure: Still relevant to understanding the structure, function and dynamics of biological membranes after more than 40 years, Biochim. Biophys. Acta - Biomembr. 1838 (2014) 1451–1466. https://doi.org/10.1016/j.bbamem.2013.10.019.

[27] Fluid Mosaic Model, Libretexts. (2019). https://bio.libretexts.org/Bookshelves/Introductory_and_General_Biology/Book%3A_General_Biology_(Boundless)/5%3A_Structure_and_Function_of_Plasma_Membranes/5.1%3A_Components_and_Structure/5.1B%3A_Fluid_Mosaic_Model.

[28] X. Zhang, W.T. Godbey, Viral vectors for gene delivery in tissue engineering, Adv.

Drug Deliv. Rev. 58 (2006) 515–534. https://doi.org/10.1016/j.addr.2006.03.006.

[29] R. Zufferey, J.E. Donello, D. Trono, T.J. Hope, Woodchuck hepatitis virus posttranscriptional regulatory element enhances expression of transgenes delivered by retroviral vectors., J. Virol. 73 (1999) 2886–92. http://www.ncbi.nlm.nih.gov/pubmed/10074136%0Ahttp://www.pubmedcentral.nih.gov/articlerender.fcgi?artid=PMC104046.

[30] L. Naldini, U. Blömer, P. Gallay, D. Ory, R. Mulligan, F.H. Gage, I.M. Verma, D. Trono, In Vivo Gene Delivery and Stable Transduction of Nondividing Cells by a Lentiviral Vector, Science (80-.). 272 (1996) 263 LP – 267. https://doi.org/10.1126/science.272.5259.263.

[31] C.M. Varga, N.C. Tedford, M. Thomas, A.M. Klibanov, L.G. Griffith, D.A. Lauffenburger, Quantitative comparison of polyethylenimine formulations and adenoviral vectors in terms of intracellular gene delivery processes, Gene Ther. 12 (2005) 1023–1032. https://doi.org/10.1038/sj.gt.3302495.

[32] M.A. Kay, J.C. Glorioso, L. Naldini, Viral vectors for gene therapy: The art of turning infectious agents into vehicles of therapeutics, Nat. Med. 7 (2001) 33–40. https://doi.org/10.1038/83324.

[33] S. Caccomo, FDA approves innovative gene therapy to treat pediatric patients with spinal muscular atrophy, a rare disease and leading genetic cause of infant mortality, FDA News Release. (2019). https://www.fda.gov/news-events/press-announcements/fda-approves-innovative-gene-therapy-treat-pediatric-patients-spinal-muscular-atrophy-rare-disease (accessed March 2, 2020).

[34] A. Fischer, FDA approves novel gene therapy to treat patients with a rare form of inherited vision loss, FDA News Release. (2017). https://www.fda.gov/news-events/press-announcements/fda-approves-novel-gene-therapy-treat-patients-rare-form-inherited-vision-loss (accessed March 2, 2020).

[35] F. Mingozzi, K.A. High, Therapeutic in vivo gene transfer for genetic disease using AAV: Progress and challenges, Nat. Rev. Genet. 12 (2011) 341–355. https://doi.org/10.1038/nrg2988.

[36] N.C. Souders, T. Verch, Y. Paterson, In Vivo Bactofection: Listeria Can Function as a DNA-Cancer Vaccine, DNA Cell Biol. 25 (2006) 142–151. https://doi.org/10.1089/dna.2006.25.142.

[37] J.H. Zheng, J.-J. Min, Targeted Cancer Therapy Using Engineered Salmonella typhimurium , Chonnam Med. J. 52 (2016) 173. https://doi.org/10.4068/cmj.2016.52.3.173.

[38] B. Hu, L. Kou, C. Li, L.P. Zhu, Y.R. Fan, Z.W. Wu, J.J. Wang, G.X. Xu, Bifidobacterium longum as a delivery system of TRAIL and endostatin cooperates with chemotherapeutic drugs to inhibit hypoxic tumor growth, Cancer Gene Ther. 16 (2009) 655–663. https://doi.org/10.1038/cgt.2009.7.

[39] R.J. Critchley, S. Jezzard, K.J. Radford, S. Goussard, N.R. Lemoine, C. Grillot-Courvalin, G. Vassaux, Potential therapeutic applications of recombinant, invasive E. coli, Gene Ther. 11 (2004) 1224–1233. https://doi.org/10.1038/sj.gt.3302281.

[40] T. Danino, A. Prindle, G.A. Kwong, M. Skalak, H. Li, K. Allen, J. Hasty, S.N. Bhatia, Programmable probiotics for detection of cancer in urine, Sci. Transl. Med. 7 (2015). https://doi.org/10.1126/scitranslmed.aaa3519.

[41] D.M. Heimann, Steven A. Rosenberg, Continuous intravenous administration of live genetically modified salmonella typhimurium in patients with metastatic melanoma., J Immunother. 29 (2012) 997–1003. https://doi.org/10.1016/j.biotechadv.2011.08.021.Secreted.

[42] J. Nemunaitis, C. Cunningham, N. Senzer, J. Kuhn, J. Cramm, C. Litz, R. Cavagnolo, A. Cahill, C. Clairmont, M. Sznol, Pilot trial of genetically modified, attenuated Salmonella expressing the E. coli cytosine deaminase gene in refractory cancer patients, Cancer Gene Ther. 10 (2003) 737–744. https://doi.org/10.1038/sj.cgt.7700634.

[43] J.F. Toso, V.J. Gill, P. Hwu, F.M. Marincola, N.P. Restifo, D.J. Schwartzentruber, R.M. Sherry, S.L. Topalian, J.C. Yang, F. Stock, L.J. Freezer, K.E. Morton, C. Seipp, L. Haworth, S. Mavroukakis, D. White, S. MacDonald, J. Mao, M. Sznol, S.A. Rosenberg, Phase I study of the intravenous administration of attenuated Salmonella typhimurium to patients with metastatic melanoma, J. Clin. Oncol. 20 (2002) 142–152. https://doi.org/10.1200/JCO.20.1.142.

[44] Y. Hamaji, M. Fujimori, T. Sasaki, H. Matsuhashi, K. Matsui-Seki, Y. Shimatani-Shibata, Y. Kano, J. Amano, S. Taniguchi, Strong enhancement of recombinant cytosine deaminase activity in Bifidobacterium longum for tumor-targeting enzyme/prodrug therapy, Biosci. Biotechnol. Biochem. 71 (2007) 874–883. https://doi.org/10.1271/bbb.60502.

[45] M.D.B. Larsen, U. Griesenbach, S. Goussard, D.C. Gruenert, D.M. Geddes, R.K. Scheule, S.H. Cheng, P. Courvalin, C. Grillot-Courvalin, E.W.F.W. Alton, Bactofection of lung epithelial cells in vitro and in vivo using a genetically modified Escherichia coli, Gene Ther. 15 (2008) 434–442. https://doi.org/10.1038/sj.gt.3303090.

[46] Y. Seow, M.J. Wood, Biological gene delivery vehicles: Beyond viral vectors, Mol. Ther. 17 (2009) 767–777. https://doi.org/10.1038/mt.2009.41.

[47] H. Yin, R.L. Kanasty, A.A. Eltoukhy, A.J. Vegas, J.R. Dorkin, D.G. Anderson, Non-viral vectors for gene-based therapy, Nat. Rev. Genet. 15 (2014) 541–555. https://doi.org/10.1038/nrg3763.

[48] J. Zhou, K.T. Shum, J.C. Burnett, J.J. Rossi, Nanoparticle-based delivery of RNAi therapeutics: Progress and challenges, Pharmaceuticals. 6 (2013) 85–107. https://doi.org/10.3390/ph6010085.

[49] L. Zhang, S; Zhi, D; Huang, Lipid-based vectors for siRNA delivery, J. Drug Target. 20 (2012) 724–739. https://doi.org/10.1016/j.physbeh.2017.03.040.

[50] D.M. Xu, S. De Yao, Y.B. Liu, K.L. Sheng, J. Hong, P.J. Gong, L. Dong, Size-dependent properties of M-PEIs nanogels for gene delivery in cancer cells, Int. J. Pharm. 338 (2007) 291–296. https://doi.org/10.1016/j.ijpharm.2007.01.050.

[51] J.R. Hobbs SK, Monsky WL, Yuan F, Roberts WG, Griffith L, Torchilin VP, Regulation of transport pathways in tumor vessels: Role of tumor type and microenvironment, Proc. Natl. Acad. Sci. 95 (1998) 4607–4612. https://doi.org/10.1073/PNAS.95.8.4607.

[52] X. Huang, X. Teng, D. Chen, F. Tang, J. He, The effect of the shape of mesoporous silica nanoparticles on cellular uptake and cell function, Biomaterials. 31 (2010) 438–448. https://doi.org/10.1016/j.biomaterials.2009.09.060.

[53] J.O. You, D.T. Auguste, Nanocarrier cross-linking density and pH sensitivity regulate intracellular gene transfer, Nano Lett. 9 (2009) 4467–4473. https://doi.org/10.1021/nl902789s.

[54] T.H. Chung, S.H. Wu, M. Yao, C.W. Lu, Y.S. Lin, Y. Hung, C.Y. Mou, Y.C. Chen, D.M. Huang, The effect of surface charge on the uptake and biological function of mesoporous silica nanoparticles in 3T3-L1 cells and human mesenchymal stem

cells, Biomaterials. 28 (2007) 2959–2966. https://doi.org/10.1016/j.biomaterials.2007.03.006.

[55] M.S. Ehrenberg, A.E. Friedman, J.N. Finkelstein, G. Oberdörster, J.L. McGrath, The influence of protein adsorption on nanoparticle association with cultured endothelial cells, Biomaterials. 30 (2009) 603–610. https://doi.org/10.1016/j.biomaterials.2008.09.050.

[56] J.M. Morachis, E.A. Mahmoud, A. Almutairi, Physical and chemical strategies for therapeutic delivery by using polymeric nanoparticles, Pharmacol. Rev. 64 (2012) 505–519. https://doi.org/10.1124/pr.111.005363.

[57] M.A. Mintzer, E.E. Simanek, Nonviral vectors for gene delivery, Chem. Rev. 109 (2009) 259–302. https://doi.org/10.1021/cr800409e.

[58] C.M. Wiethoff, C.R. Middaugh, Barriers to Nonviral Gene Delivery, J. Pharm. Sci. 92 (2003) 203–217. https://doi.org/https://doi.org/10.1002/jps.10286.

[59] U. Zimmermann, G. Pilwat, F. Riemann, Dielectric Breakdown of Cell Membranes, Biophys. J. 14 (1974) 881–899. https://doi.org/10.1016/S0006-3495(74)85956-4.

[60] M.R. Prausnitz, B.S. Lau, C.D. Milano, S. Conner, R. Langer, J.C. Weaver, A quantitative study of electroporation showing a plateau in net molecular transport, Biophys. J. 65 (1993) 414–422. https://doi.org/10.1016/S0006-3495(93)81081-6.

[61] J. Gehl, Electroporation: theory and methods, perspectives for drug delivery, gene therapy and research, Acta Physiol. Scand. (2003) 437–447.

[62] M.B. Fox, D.C. Esveld, A. Valero, R. Luttge, H.C. Mastwijk, P. V Bartels, A. van den Berg, R.M. Boom, Electroporation of cells in microfluidic devices: a review, Anal. Bioanal. Chem. 385 (2006) 474. https://doi.org/10.1007/s00216-006-0327-3.

[63] S.H. Bloch, P.A. Dayton, K.W. Ferrara, Targeted imaging using ultrasound contrast agents, IEEE Eng. Med. Biol. Mag. 23 (2004) 18–27. https://doi.org/10.1109/MEMB.2004.1360405.

[64] M. Schneider, Molecular imaging and ultrasound-assisted drug delivery.PDF, J. Endourol. 22 (2008) 795–801. https://go.gale.com/ps/i.do?p=AONE&u=gainstoftech&id=GALE%7CA18292350

8&v=2.1&it=r.

[65] A.L. Klibanov, Microbubble Contrast Agents: Targeted Ultrasound Imaging and Ultrasound-Assisted Drug-Delivery Applications, Invest. Radiol. 41 (2006). https://journals.lww.com/investigativeradiology/Fulltext/2006/03000/Microbubble_Contrast_Agents__Targeted_Ultrasound.20.aspx.

[66] R.K. Schlicher, J.D. Hutcheson, H. Radhakrishna, R.P. Apkarian, M.R. Prausnitz, Changes in Cell Morphology Due to Plasma Membrane Wounding by Acoustic Cavitation, Ultrasound Med. Biol. 36 (2010) 677–692. https://doi.org/10.1016/j.ultrasmedbio.2010.01.010.

[67] V.G. Zarnitsyn, M.R. Prausnitz, Physical parameters influencing optimization of ultrasound-mediated DNA transfection, Ultrasound Med. Biol. 30 (2004) 527–538. https://doi.org/10.1016/j.ultrasmedbio.2004.01.008.

[68] D.L. Miller, J. Song, Tumor growth reduction and DNA transfer by cavitation-enhanced high-intensity focused ultrasound in vivo, Ultrasound Med. Biol. 29 (2003) 887–893. https://doi.org/10.1016/S0301-5629(03)00031-0.

[69] Y.-I. Yamashita, M. Shimada, K. Tachibana, N. Harimoto, E. Tsujita, K. Shirabe, J.-I. Miyazaki, K. Sugimachi, In Vivo Gene Transfer into Muscle via Electro-Sonoporation, Hum. Gene Ther. 13 (2002) 2079–2084. https://doi.org/10.1089/10430340260395929.

[70] M. Graessmann, A. Graessmann, Microinjection of tissue culture cells, Methods Enzymol. 101 (1983) 482–492. https://doi.org/10.1016/0076-6879(83)01033-2.

[71] R.J. Griesbach, Chromosome-mediated transformation via microinjection, Plant Sci. 50 (1987) 69–77. https://doi.org/https://doi.org/10.1016/0168-9452(87)90032-X.

[72] R. Pepperkok, M. Zanetti, R. King, D. Delia, W. Ansorge, L. Philipson, C. Schneider, Automatic microinjection system facilitates detection of growth inhibitory mRNA, Proc. Natl. Acad. Sci. U. S. A. 85 (1988) 6748–6752. https://doi.org/10.1073/pnas.85.18.6748.

[73] R. Pepperkok, R. Saffrich, W. Ansorge, Computer-Automated Capillary Microinjection of Macromolecules into Living Cells, ACADEMIC PRESS, INC., 1994. https://doi.org/10.1016/b978-0-12-164717-9.50007-6.

[74] S. Chenuet, M. Derouazi, D. Hacker, F. Wurm, DNA Delivery by Microinjection for the Generation of Recombinant Mammalian Cell Lines BT - Microinjection: Methods and Applications, in: D.J. Carroll (Ed.), Microinjection, Humana Press, Totowa, NJ, 2009: pp. 99–112. https://doi.org/10.1007/978-1-59745-202-1_8.

[75] Y. Kagawa, Y. Inoki, H. Endo, Gene therapy by mitochondrial transfer, Adv. Drug Deliv. Rev. 49 (2001) 107–119. https://doi.org/10.1016/S0169-409X(01)00129-6.

[76] A.A.S. Bhagat, H. Bow, H.W. Hou, S.J. Tan, J. Han, C.T. Lim, Microfluidics for cell separation, Med. Biol. Eng. Comput. 48 (2010) 999–1014. https://doi.org/10.1007/s11517-010-0611-4.

[77] M.E. Kizer, Y. Deng, G. Kang, P.E. Mikael, X. Wang, A.J. Chung, Hydroporator: A hydrodynamic cell membrane perforator for high-throughput vector-free nanomaterial intracellular delivery and DNA origami biostability evaluation, Lab Chip. 19 (2019) 1747–1754. https://doi.org/10.1039/c9lc00041k.

[78] A. Sharei, R. Poceviciute, E.L. Jackson, N. Cho, S. Mao, G.C. Hartoularos, D.Y. Jang, S. Jhunjhunwala, A. Eyerman, T. Schoettle, R. Langer, K.F. Jensen, Plasma membrane recovery kinetics of a microfluidic intracellular delivery platform, Integr. Biol. (United Kingdom). 6 (2014) 470–475. https://doi.org/10.1039/c3ib40215k.

[79] A. Liu, M. Islam, N. Stone, V. Varadarajan, J. Jeong, S. Bowie, P. Qiu, E.K. Waller, A. Alexeev, T. Sulchek, Microfluidic generation of transient cell volume exchange for convectively driven intracellular delivery of large macromolecules, Mater. Today. 21 (2018) 703–712. https://doi.org/10.1016/j.mattod.2018.03.002.

[80] A. Sharei, J. Zoldan, A. Adamo, W. Young, N. Cho, E. Jackson, S. Mao, A vector-free micro fluidic platform for intracellular delivery, Proc. Natl. Acad. Sci. 110 (2013) 2082–2087. https://doi.org/10.1073/pnas.1218705110.

[81] C.P. F Scherer, M Anton, U Schillinger, J Henke, C Bergemann, A Krüger, B Gänsbacher, Magnetofection: enhancing and targeting gene delivery by magnetic force in vitro and in vivo, Gene Ther. 9 (2002) 102–109. https://doi.org/10.1038/sj/gt/3301624.

[82] S.C. Goodwin, C.A. Bittner, C.L. Peterson, G. Wong, Single-dose toxicity study of hepatic intra-arterial infusion of doxorubicin coupled to a novel magnetically targeted drug carrier, Toxicol. Sci. 60 (2001) 177–183. https://doi.org/10.1093/toxsci/60.1.177.

[83] L. Prosen, S. Prijic, B. Music, J. Lavrencak, M. Cemazar, G. Sersa, Magnetofection: A reproducible method for gene delivery to melanoma cells, Biomed Res. Int. 2013 (2013) 6–8. https://doi.org/10.1155/2013/209452.

[84] T.M. Klein, E.D. Wolf, R. Wu, J.C. Sanford, High-velocity microprojectiles for delivering nucleic acids into living cells, Nature. 327 (1987) 70–73. https://doi.org/10.1038/327070a0.

[85] N.S. Yang, J. Burkholder, B. Roberts, B. Martinell, D. Mccabe, In vivo and in vitro gene transfer to mammalian somatic cells by particle bombardment, Proc. Natl. Acad. Sci. U. S. A. 87 (1990) 9568–9572. https://doi.org/10.1073/pnas.87.24.9568.

[86] J.C. Sanford, F.D. Smith, J.A. Russell, Optimizing The Biolistic Process for Different Biological Applications, Methods Enzymol. 217 (1993) 483–509. https://doi.org/10.1016/0076-6879(93)17086-K.

[87] M.D. EISENBRAUN, D.H. FULLER, J.R. HAYNES, Examination of Parameters Affecting the Elicitation of Humoral Immune Responses by Particle Bombardment-Mediated Genetic Immunization, DNA Cell Biol. 12 (1993) 791–797. https://doi.org/10.1089/dna.1993.12.791.

[88] R.J. Drape, M.D. Macklin, L.J. Barr, S. Jones, J.R. Haynes, H.J. Dean, Epidermal DNA vaccine for influenza is immunogenic in humans, Vaccine. 24 (2006) 4475–4481. https://doi.org/10.1016/j.vaccine.2005.08.012.

[89] D.H. Fuller, P. Loudon, C. Schmaljohn, Preclinical and clinical progress of particle-mediated DNA vaccines for infectious diseases, Methods. 40 (2006) 86–97. https://doi.org/10.1016/j.ymeth.2006.05.022.

[90] D.L. Lodmell, M.J. Parnell, J.R. Bailey, L.C. Ewalt, C.A. Hanlon, One-time gene gun or intramuscular rabies DNA vaccination of non-human primates: Comparison of neutralizing antibody responses and protection against rabies virus 1 year after vaccination, Vaccine. 20 (2001) 838–844. https://doi.org/10.1016/S0264-410X(01)00392-9.

[91] M. Alsaggar, D. Liu, Physical Methods for Gene Transfer, Elsevier Ltd, 2015. https://doi.org/10.1016/bs.adgen.2014.10.001.

[92] A. V. Melechko, R. Desikan, T.E. McKnight, K.L. Klein, P.D. Rack, Synthesis of vertically aligned carbon nanofibres for interfacing with live systems, J. Phys. D.

Appl. Phys. 42 (2009). https://doi.org/10.1088/0022-3727/42/19/193001.

[93] D.G.J. Mann, T.E. Mcknight, J.T. Mcpherson, P.R. Hoyt, A. V Melechko, M.L. Simpson, G.S. Sayler, Inducible RNA Interference-Mediated Gene Silencing Using Nanostructured Gene Delivery Arrays, ACS Nano. 2 (2008) 69–76.

[94] D.B. Peckys, A. V. Melechko, M.L. Simpson, T.E. McKnight, Immobilization and release strategies for DNA delivery using carbon nanofiber arrays and self-assembled monolayers, Nanotechnology. 20 (2009). https://doi.org/10.1088/0957-4484/20/14/145304.

[95] R.C. Pearce, J.G. Railsback, B.D. Anderson, M.F. Sarac, T.E. McKnight, J.B. Tracy, A. V. Melechko, Transfer of vertically aligned carbon nanofibers to polydimethylsiloxane (PDMS) while maintaining their alignment and impalefection functionality, ACS Appl. Mater. Interfaces. 5 (2013) 878–882. https://doi.org/10.1021/am302501z.

[96] J.M. Wörle-Knirsch, K. Pulskamp, H.F. Krug, Oops they did it again! Carbon nanotubes hoax scientists in viability assays, Nano Lett. 6 (2006) 1261–1268. https://doi.org/10.1021/nl060177c.

[97] K.L. Chen, G.D. Bothun, Nanoparticles meet cell membranes: Probing nonspecific interactions using model membranes, Environ. Sci. Technol. 48 (2014) 873–880. https://doi.org/10.1021/es403864v.

[98] K. Kostarelos, L. Lacerda, G. Pastorin, W. Wu, S. Wieckowski, J. Luangsivilay, S. Godefroy, D. Pantarotto, J.P. Briand, S. Muller, M. Prato, A. Bianco, Cellular uptake of functionalized carbon nanotubes is independent of functional group and cell type, Nat. Nanotechnol. 2 (2007) 108–113. https://doi.org/10.1038/nnano.2006.209.

[99] G.S. Demirer, H. Zhang, N.S. Goh, E. González-Grandío, M.P. Landry, Carbon nanotube–mediated DNA delivery without transgene integration in intact plants, Nat. Protoc. 14 (2019) 2954–2971. https://doi.org/10.1038/s41596-019-0208-9.

[100] S. Arayachukiat, J. Seemork, P. Pan-In, K. Amornwachirabodee, N. Sangphech, T. Sansureerungsikul, K. Sathornsantikun, C. Vilaivan, K. Shigyou, P. Pienpinijtham, T. Vilaivan, T. Palaga, W. Banlunara, T. Hamada, S. Wanichwecharungruang, Bringing macromolecules into cells and evading endosomes by oxidized carbon nanoparticles, Nano Lett. 15 (2015) 3370–3376. https://doi.org/10.1021/acs.nanolett.5b00696.

[101] K. Amornwachirabodee, N. Tantimekin, P. Pan-in, T. Palaga, Oxidized Carbon Black : Preparation , Characterization and Application in Antibody Delivery across Cell Membrane, Sci. Rep. (2018) 1–11. https://doi.org/10.1038/s41598-018-20650-4.

[102] R. Xiong, S.K. Samal, J. Demeester, A.G. Skirtach, S.C. De Smedt, K. Braeckmans, Laser-assisted photoporation: fundamentals, technological advances and applications, Adv. Phys. X. 1 (2016) 596–620. https://doi.org/10.1080/23746149.2016.1228476.

[103] P.A. Quinto-Su, V. Venugopalan, Mechanisms of Laser Cellular Microsurgery, Methods Cell Biol. 82 (2007). https://doi.org/10.1016/S0091-679X(06)82004-2.

[104] D. Heinemann, S. Kalies, M. Schomaker, W. Ertmer, H. Murua Escobar, H. Meyer, T. Ripken, Delivery of proteins to mammalian cells via gold nanoparticle mediated laser transfection, Nanotechnology. 25 (2014). https://doi.org/10.1088/0957-4484/25/24/245101.

[105] C.M. Pitsillides, E.K. Joe, X. Wei, R.R. Anderson, C.P. Lin, Selective cell targeting with light-absorbing microparticles and nanoparticles, Biophys. J. 84 (2003) 4023–4032. https://doi.org/10.1016/S0006-3495(03)75128-5.

[106] Q. Peng, A. Juzeniene, J. Chen, L.O. Svaasand, T. Warloe, K.E. Giercksky, J. Moan, Lasers in medicine, Reports Prog. Phys. 71 (2008). https://doi.org/10.1088/0034-4885/71/5/056701.

[107] W. Eisenberg, Method utilizing a laser for eye surgery, United States Pat. (1981). https://patents.google.com/patent/US4559942A/en.

[108] K.M. Bhatta, Lasers in urology, Lasers Surg. Med. 16 (1995) 312–330. https://doi.org/10.1002/lsm.1900160403.

[109] K.F. Chan, T. Joshua Pfefer, J.M.H. Teichman, A.J. Welch, A Perspective on Laser Lithotripsy: The Fragmentation Processes, J. Endourol. 15 (2001) 257–273. https://doi.org/10.1089/089277901750161737.

[110] W. CHAFE, K. FERGUSON, E.J. WILKINSON, Vulvar Intraepithelial Neoplasia (VIN): Principles of Surgical Therapy, J. Gynecol. Surg. 4 (1988) 125–132. https://doi.org/10.1089/gyn.1988.4.125.

[111] N.S. Nishioka, Applications of lasers in gastroenterology, Lasers Surg. Med. 16 (1995) 205–214. https://doi.org/10.1002/lsm.1900160302.

[112] M. Remacle, E. Bodart, G. Lawson, M. Minet, A. Mayné, Use of the CO2-laser micropoint micromanipulator for the treatment of laryngomalacia, Eur. Arch. Oto-Rhino-Laryngology. 253 (1996) 401–404. https://doi.org/10.1007/BF00168491.

[113] M. Wilson, J. Dobson, W. Harvey, Sensitization of oral bacteria to killing by low-power laser radiation, Curr. Microbiol. 25 (1992) 77–81. https://doi.org/10.1007/BF01570963.

[114] R.G. Wheeland, Clinical uses of lasers in dermatology, Lasers Surg. Med. 16 (1995) 2–23. https://doi.org/10.1002/lsm.1900160103.

[115] J.S. McCaughan, Photodynamic Therapy: A review, Drugs Aging. 15 (1999) 49–68. https://doi.org/10.2165/00002512-199915010-00005.

[116] V. Shanmugam, S. Selvakumar, C.S. Yeh, Near-infrared light-responsive nanomaterials in cancer therapeutics, Chem. Soc. Rev. 43 (2014) 6254–6287. https://doi.org/10.1039/c4cs00011k.

[117] A.M. Gobin, M.H. Lee, N.J. Halas, W.D. James, R.A. Drezek, J.L. West, Near-infrared resonant nanoshells for combined optical imaging and photothermal cancer therapy, Nano Lett. 7 (2007) 1929–1934. https://doi.org/10.1021/nl070610y.

[118] X. Huang, I.H. El-Sayed, W. Qian, M.A. El-Sayed, Cancer cell imaging and photothermal therapy in the near-infrared region by using gold nanorods, J. Am. Chem. Soc. 128 (2006) 2115–2120. https://doi.org/10.1021/ja057254a.

[119] H.H. Kampinga, Cell biological effects of hyperthermia alone or combined with radiation or drugs: A short introduction to newcomers in the field, Int. J. Hyperth. 22 (2006) 191–196. https://doi.org/10.1080/02656730500532028.

[120] A.G. Bell, Upon the production and reproduction of sound by light, J. Soc. Telegr. Eng. 9 (1880) 404–426.

[121] Y.S. Chen, D. Yeager, S.Y. Emelianov, Photoacoustic Imaging for Cancer Diagnosis and Therapy Guidance, Elsevier Inc., 2014. https://doi.org/10.1016/B978-0-12-407722-5.00009-8.

[122] L. V. Wang, S. Hu, Photoacoustic tomography: In vivo imaging from organelles to organs, Science (80-.). 335 (2012) 1458–1462. https://doi.org/10.1126/science.1216210.

[123] S. Hu, L. V. Wang, Optical-resolution photoacoustic microscopy: Auscultation of biological systems at the cellular level, Biophys. J. 105 (2013) 841–847. https://doi.org/10.1016/j.bpj.2013.07.017.

[124] H. Chen, G. Diebold, Chemical Generation of Acoustic Waves: A Giant Photoacoustic Effect, Science (80-.). 270 (1995) 963 LP – 966. http://science.sciencemag.org/content/270/5238/963.abstract.

[125] T.E. McGrath, G.J. Diebold, D.M. Bartels, R.A. Crowell, Laser-initiated chemical reactions in carbon suspensions, J. Phys. Chem. A. 106 (2002) 10072–10078. https://doi.org/10.1021/jp0208135.

[126] P. Chakravarty, Photoacoustic Drug Delivery Using Carbon Nanoparticles Activated By Femtosecond and Nanosecond Laser Pulses, 2009.

[127] P. Chakravarty, C.D. Lane, T.M. Orlando, M.R. Prausnitz, Parameters affecting intracellular delivery of molecules using laser-activated carbon nanoparticles, Nanomedicine Nanotechnology, Biol. Med. 12 (2016) 1003–1011. https://doi.org/10.1016/j.nano.2015.12.380.

[128] H.P. Nizam R, Siddiqi N, Landas SK, Kaplan DS, Colonic tattooing with India ink: benefits, risks, and alternatives., Am. J. Gastroenterol. 91 (1996) 1804–1808. https://www.ncbi.nlm.nih.gov/pubmed/8792702.

[129] O.T. Fujita H, Ueda A, Nishida T, Uptake of india ink particles and latex beads by corneal fibroblasts, Cell Tissue Res. 250 (1987) 251–5. https://www.ncbi.nlm.nih.gov/pubmed/2448032.

[130] P.I. Haigh, A. Lucci, R.R. Turner, P.J. Bostick, D.L. Krasne, S.L. Stern, D.L. Morton, Carbon dye histologically confirms the identity of sentinel lymph nodes in cutaneous melanoma, Cancer. 92 (2001) 535–541. https://doi.org/10.1002/1097-0142(20010801)92:3<535::AID-CNCR1352>3.0.CO;2-3.

[131] A. Brandwood, K.R. Noble, K. Schindhelm, Phagocytosis of carbon particles by macrophages In vitro, Biomaterials. 13 (1992) 646–648. https://doi.org/10.1016/0142-9612(92)90035-M.

[132] A. Sengupta, N. Dwivedi, S.C. Kelly, L. Tucci, N.N. Thadhani, M.R. Prausnitz, Poloxamer surfactant preserves cell viability during photoacoustic delivery of molecules into cells, Biotechnol. Bioeng. 112 (2015) 405–415. https://doi.org/10.1002/bit.25363.

[133] C.E. Thomas, A. Ehrhardt, M.A. Kay, Progress and problems with the use of viral vectors for gene therapy, Nat. Rev. Genet. 4 (2003) 346–358. https://doi.org/10.1038/nrg1066.

[134] O. Boussif, F. LezoualC'H, M.A. Zanta, M.D. Mergny, D. Scherman, B. Demeneix, J.P. Behr, A versatile vector for gene and oligonucleotide transfer into cells in culture and in vivo: Polyethylenimine, Proc. Natl. Acad. Sci. U. S. A. 92 (1995) 7297–7301. https://doi.org/10.1073/pnas.92.16.7297.

[135] S.E. Park, M.I. Sajid, K. Parang, R.K. Tiwari, Cyclic cell-penetrating peptides as efficient intracellular drug delivery tools, Mol. Pharm. 16 (2019) 3727–3743. https://doi.org/10.1021/acs.molpharmaceut.9b00633.

[136] P.L. Felgner, T.R. Gadek, M. Holm, R. Roman, H.W. Chan, M. Wenz, J.P. Northrop, G.M. Ringold, M. Danielsen, Lipofection : A highly efficient , lipid-mediated DNA-transfection procedure, Proc. Natl. Acad. Sci. 84 (1987) 7413–7417.

[137] M.X. Tang, C.T. Redemann, F.C. Szoka, In vitro gene delivery by degraded polyamidoamine dendrimers, Bioconjug. Chem. 7 (1996) 703–714. https://doi.org/10.1021/bc9600630.

[138] M.P. Stewart, R. Langer, K.F. Jensen, Intracellular delivery by membrane disruption: Mechanisms, strategies, and concepts, Chem. Rev. 118 (2018) 7409–7531. https://doi.org/10.1021/acs.chemrev.7b00678.

[139] L. Kou, J. Sun, Y. Zhai, Z. He, The endocytosis and intracellular fate of nanomedicines: Implication for rational design, Asian J. Pharm. Sci. 8 (2013) 1–10. https://doi.org/10.1016/j.ajps.2013.07.001.

[140] A.M. Bodles-Brakhop, R. Heller, R. Draghia-Akli, Electroporation for the Delivery of DNA-based Vaccines and Immunotherapeutics: Current Clinical Developments, Mol. Ther. 17 (2009) 585–592. https://doi.org/10.1038/mt.2009.5.

[141] H.R. Guzmán, D.X. Nguyen, S. Khan, M.R. Prausnitz, Ultrasound-mediated disruption of cell membranes. I. Quantification of molecular uptake and cell

viability, J. Acoust. Soc. Am. 110 (2001) 588–596. https://doi.org/10.1121/1.1376131.

[142] and A.G.F. J. Mark Meacham, Kiranmai Durvasula, F. Levent Degertekin, Physical Methods for Intracellular Delivery: Practical Aspects from Laboratory Use to Industrial-Scale Processing, J. Lab. Autom. 19 (2014) 1–18. https://doi.org/10.1177/2211068213494388.

[143] C. Jumelle, C. Mauclair, J. Houzet, A. Bernard, Z. He, F. Forest, C. Perrache, P. Gain, G. Thuret, Delivery of macromolecules into the endothelium of whole ex vivo human cornea by femtosecond laser-activated carbon nanoparticles, Br. J. Ophthalmol. 100 (2016) 1151–1156. https://doi.org/10.1136/bjophthalmol-2015-307610.

[144] H.R. Guzmán, A.J. McNamara, D.X. Nguyen, M.R. Prausnitz, Bioeffects caused by changes in acoustic cavitation bubble density and cell concentration: A unified explanation based on cell-to-bubble ratio and blast radius, Ultrasound Med. Biol. 29 (2003) 1211–1222. https://doi.org/10.1016/S0301-5629(03)00899-8.

[145] P. Qin, L. Jin, L. Fan, H. Tao, L. Du, A.C.H. Yu, The relationship between microbubble size and heterogeneous sonoporation at the single-cell level, IEEE Int. Ultrason. Symp. IUS. 2016-Novem (2016) 2–5. https://doi.org/10.1109/ULTSYM.2016.7728424.

[146] R. Xiong, K. Raemdonck, K. Peynshaert, I. Lentacker, I. De Cock, J. Demeester, S.C. De Smedt, A.G. Skirtach, K. Braeckmans, Laser-induced vapor nanobubbles for efficient delivery of macromolecules in live cells, Colloid. Nanoparticles Biomed. Appl. X. 9338 (2015) 93381J. https://doi.org/10.1117/12.2078895.

[147] A.H. Liao, H.C. Ho, Y.C. Lin, H.K. Chen, C.H. Wang, Effects of microbubble size on ultrasound-induced transdermal delivery of high-molecular-weight drugs, PLoS One. 10 (2015) 1–14. https://doi.org/10.1371/journal.pone.0138500.

[148] L.R. Hirsch, R.J. Stafford, J.A. Bankson, S.R. Sershen, B. Rivera, R.E. Price, J.D. Hazle, N.J. Halas, J.L. West, Nanoshell-mediated near-infrared thermal therapy of tumors under magnetic resonance guidance, Proc. Natl. Acad. Sci. U. S. A. 100 (2003) 13549–13554. https://doi.org/10.1073/pnas.2232479100.

[149] V.P. Torchilin, Recent Approaches To Intracellular Delivery of Drugs and Dna and Organelle Targeting, Annu. Rev. Biomed. Eng. 8 (2006) 343–375. https://doi.org/10.1146/annurev.bioeng.8.061505.095735.

[150] R. Xiong, S.K. Samal, J. Demeester, A.G. Skirtach, S.C. De Smedt, K. Braeckmans, R. Xiong, S.K. Samal, J. Demeester, G. Andre, Laser-assisted photoporation : fundamentals , technological advances and applications, Adv. Phys. X. 6149 (2016) 596–620. https://doi.org/10.1080/23746149.2016.1228476.

[151] W.T. Godbey, Cellular Transport, in: An Introd. to Biotechnol. Sci. Technol. Med. Appl., Woodhead publishing, 2014: pp. 35–64. http://www.sciencedirect.com/science/article/pii/B9781907568282000034.

[152] M.L. Casem, Chapter 9 - Endocytosis, in: M.L. Casem (Ed.), Case Stud. Cell Biol., Academic Press, Boston, 2016: pp. 217–240. https://doi.org/https://doi.org/10.1016/B978-0-12-801394-6.00009-9.

[153] L.M. Bareford, P.W. Swaan, Endocytotic mechanisms for Targeted Drug Delivery, Adv. Drug Deliv. Rev. 59 (2007) 748–758. https://doi.org/10.1017/CBO9781107415324.004.

[154] A. Akinc, G. Battaglia, Exploiting Endocytosis for Nanomedicines, Cold Spring Harb. Perspect. Biol. 5 (2017).

[155] X. Feng, Y. Tang, X. Duan, L. Liu, S. Wang, Lipid-modified conjugated polymernanoparticles for cell imaging and transfection, J. Mater. Chem. 20 (2010) 1312–1316. https://doi.org/10.1039/B915112E.

[156] A. Sengupta, S.C. Kelly, N. Dwivedi, N. Thadhani, M.R. Prausnitz, ARTICLE Efficient Intracellular Delivery of Molecules with High Cell Viability Activated Carbon Nanoparticles, ACS Nano. 8 (2014) 2889–2899. https://doi.org/10.1021/nn500100x.

[157] Y. Liu, J. Yan, M.R. Prausnitz, Can Ultrasound Enable Efficient Intracellular Uptake of Molecules? A Retrospective Literature Review and Analysis, Ultrasound Med. Biol. 38 (2012) 876–888. https://doi.org/10.1016/j.ultrasmedbio.2012.01.006.

[158] P.J. Canatella, J.F. Karr, J.A. Petros, M.R. Prausnitz, Quantitative study of electroporation-mediated molecular uptake and cell viability, Biophys. J. 80 (2001) 755–764. https://doi.org/10.1016/S0006-3495(01)76055-9.

[159] L. Miller, J. Leor, B. Rubinsky, Cancer cells ablation with irreversible electroporation, Technol. Cancer Res. Treat. 4 (2005) 699–705. https://doi.org/10.1177/153303460500400615.

[160] J.J. Chalmers, Mixing, aeration and cell damage, 30+ years later: What we learned, how it affected the cell culture industry and what we would like to know more about, Curr. Opin. Chem. Eng. 10 (2015) 94–102. https://doi.org/10.1016/j.coche.2015.09.005.

[161] K.T. Kunas, E.T. Papoutsakis, The protective effect of serum against hydrodynamic damage of hybridoma cells in agitated and surface-aerated bioreactors, J. Biotechnol. 15 (1990) 57–69. https://doi.org/10.1016/0168-1656(90)90051-C.

[162] S.-E. Han, H. Kang, G.Y. Shim, M.S. Suh, S.J. Kim, J.-S. Kim, Y.-K. Oh, Novel cationic cholesterol derivative-based liposomes for serum-enhanced delivery of siRNA, Int. J. Pharm. 353 (2008) 260–269. https://doi.org/10.1016/J.IJPHARM.2007.11.026.

[163] S. Shahabi, S. Döscher, T. Bollhorst, L. Treccani, M. Maas, R. Dringen, K. Rezwan, Enhancing Cellular Uptake and Doxorubicin Delivery of Mesoporous Silica Nanoparticles via Surface Functionalization: Effects of Serum, ACS Appl. Mater. Interfaces. 7 (2015) 26880–26891. https://doi.org/10.1021/acsami.5b09483.

[164] J.H. Park, J.A. Jackman, A.R. Ferhan, G.J. Ma, B.K. Yoon, N. Cho, Temperature-Induced Denaturation of BSA Protein Molecules for Improved Surface Passivation Coatings, ACS Appl. Mater. Interfaces. 10 (2018) 32047–32057. https://doi.org/10.1021/acsami.8b13749.

[165] M.E. Stathopulos PB, Scholz GA, Hwang YM, Rumfeldt JA, Lepock JR, Sonication of proteins causes formation of aggregates that resemble amyloid.pdf, Protein Sci. 13 (2004) 3017–3027. http://www.proteinscience.org/cgi/doi/10.1110/ps.0483180.

[166] G.L. Francis, Albumin and mammalian cell culture: Implications for biotechnology applications, Cytotechnology. 62 (2010) 1–16. https://doi.org/10.1007/s10616-010-9263-3.

[167] E.T. Papoutsakis, Media additives for protecting freely suspended animal cells against agRation and aeration damage, Trends Biotechnol. 9 (1991) 316–324.

[168] E. Boucher, C.A. Mandato, Plasma membrane and cytoskeleton dynamics during single-cell wound healing, Biochim. Biophys. Acta - Mol. Cell Res. 1853 (2015) 2649–2661. https://doi.org/10.1016/j.bbamcr.2015.07.012.

[169] T. Bewersdorff, A. Gruber, M. Eravci, M. Dumbani, D. Klinger, A. Haase,

Amphiphilic nanogels: Influence of surface hydrophobicity on protein corona, biocompatibility and cellular uptake, Int. J. Nanomedicine. 14 (2019) 7861–7878. https://doi.org/10.2147/IJN.S215935.

[170] J.D. Michaels, J.F. Petersebt, L. V Mclntire, E.T. Papoutsakis, Protection Mechanisms of Freely Suspended Animal Cells (CRL 8018) from Fluid-Mechanical Injury . Viscomet ric and Bioreactor Studies Using Serum , Pluronic F68 and Polyethylene Glycol, Biotechnol. Bioeng. 38 (1990) 169–180.

[171] L.A. Van Der Po, I. Beeksma, J. Tramper, Polyethylene glycol as protectant against damage caused by sparging for hybridoma suspension cells in a bubble column, Enzyme Microb. Technol. 17 (1995) 401–407.

[172] Y. Shintani, K. Iwamoto, K. Kitano, Polyethylene glycols for promoting the growth of mammalian cells, Appl. Microbiol. Biotechnol. 27 (1988) 533–537. https://doi.org/10.1007/BF00451627.

[173] M.J. Poellmann, R.C. Lee, R.C. Lee, Repair and Regeneration of the Wounded Cell Membrane, Regen. Eng. Soc. 641 (2017) 111–132. https://doi.org/10.1007/s40883-017-0031-1.

[174] T. Lindl, Zell- und Gewebekultur, 5th ed., Spektrum Akademischer Verlag, Heidelberg, 2002.

[175] A.O. Elzoghby, W.M. Samy, N.A. Elgindy, Albumin-based nanoparticles as potential controlled release drug delivery systems, J. Control. Release. 157 (2012) 168–182. https://doi.org/10.1016/j.jconrel.2011.07.031.

[176] J.D. Michaels, J.E. Nowak, A.K. Mallik, K. Koczo, D.T. Wasan, E.T. Papoutsakis, Interfacial properties of cell culture media with cell-protecting additives, Biotechnol. Bioeng. 47 (1995) 420–430.

[177] P. Raffa, D.A.Z. Wever, F. Picchioni, A.A. Broekhuis, Polymeric surfactants: Synthesis, properties, and links to applications, Chem. Rev. 115 (2015) 8504–8563. https://doi.org/10.1021/cr500129h.

[178] H. Lee, R.M. Venable, A.D. MacKerell, R.W. Pastor, Molecular dynamics studies of polyethylene oxide and polyethylene glycol: Hydrodynamic radius and shape anisotropy, Biophys. J. 95 (2008) 1590–1599. https://doi.org/10.1529/biophysj.108.133025.

[179] S. Bharadwaj, R. Vishnubhotla, S. Shan, C. Chauhan, M. Cho, S.C. Glover, Higher molecular weight polyethylene glycol increases cell proliferation while improving barrier function in an in vitro colon cancer model, J. Biomed. Biotechnol. 2011 (2011). https://doi.org/10.1155/2011/587470.

[180] R.C. Lee, Cytoprotection by stabilization of cell membranes, Ann. N. Y. Acad. Sci. 961 (2002) 271–275. https://doi.org/10.1111/j.1749-6632.2002.tb03100.x.

[181] J. Wu, A.J. Daugulis, P. Faulkner, M.F.A. Goosen, Protective Effects of Polymer Additives on Animal Cells Exposed to Rapidly Falling Liquid Films, Biotechnol. Prog. 11 (1995) 127–132. https://doi.org/10.1021/bp00032a002.

[182] J.D. Michaels, J.E. Nowak, A.K. Mallik, K. Koczo, D.T. Wasan, E.T. Papoutsakis, Analysis of cell-to-bubble attachment in sparged bioreactors in the presence of cell-protecting additives, Biotechnol. Bioeng. 47 (1995) 407–419. https://doi.org/10.1002/bit.260470402.

[183] F.A. Merchant, W.H. Holmes, M. Capelli-Schellpfeffer, R.C. Lee, M. Toner, Poloxamer 188 enhances functional recovery of lethally heat-shocked fibroblasts, J. Surg. Res. 74 (1998) 131–140. https://doi.org/10.1006/jsre.1997.5252.

[184] T. Pastinen, T.J. Hudson, Cis-Acting Regulatory Variation in the Human Genome, Science (80-.). 306 (2004) 647–650. https://doi.org/10.1126/science.1101659.

[185] R.J. Lefkowitz, S.K. Shenoy, Transduction of Receptor Signals by ß-Arrestins, Science (80-.). 308 (2005) 512 LP – 517. https://doi.org/10.1126/science.1109237.

[186] I.B. Clark, E.G. Hanania, J. Stevens, M. Gallina, A. Fieck, R. Brandes, B.O. Palsson, M.R. Koller, Optoinjection for efficient targeted delivery of a broad range of compounds and macromolecules into diverse cell types, J. Biomed. Opt. 11 (2006) 014034. https://doi.org/10.1117/1.2168148.

[187] R.M.. Paiva, G.A.R. Goncalves, Gene therapy : advances, challenges and perspectives, Einstein (Sao Paulo). 15 (2017) 369–375. https://doi.org/10.1590/S1679-45082017RB4024.

[188] A. Erazo-Oliveras, K. Najjar, L. Dayani, T.Y. Wang, G.A. Johnson, J.P. Pellois, Protein delivery into live cells by incubation with an endosomolytic agent, Nat. Methods. 11 (2014) 861–867. https://doi.org/10.1038/nMeth.2998.

[189] Z. Zhu, D. Tian, P. Gao, K. Wang, Y. Li, X. Shu, J. Zhu, Q. Zhao, Cell-Penetrating Peptides Transport Noncovalently Linked Thermally Activated Delayed Fluorescence Nanoparticles for Time- Resolved Luminescence Imaging, J. Am. Chem. Soc. 140 (2018) 17484–17491. https://doi.org/10.1021/jacs.8b08438.

[190] A. Joliot, C. Pernelle, H. Deagostini-Bazin, A. Prochantz, Antennapedia homeobox peptide regulates neural morphogenesis, Proc. Natl. Acad. Sci. 88 (1991) 1864–1868.

[191] T.Y. Gu Z, Biswas A, Zhao M, Tailoring nanocarriers for intracellular protein delivery, Chem. Soc. Rev. 40 (2011) 3638–3655. https://doi.org/10.1039/c0cs00227e.

[192] M.H. Amer, Gene therapy for cancer : present status and future perspective, Mol. Cell. Ther. 2 (2014) 1–19. https://www.ncbi.nlm.nih.gov/pmc/articles/PMC4452068/.

[193] M. Sanchez-Navarro, M. Teixido, E. Giralt, Jumping Hurdles: Peptides Able To Overcome Biological Barriers, Acc. Chem. Res. 50 (2017) 1847–1854. https://doi.org/10.1021/acs.accounts.7b00204.

[194] T. Vermonden, R. Censi, W.E. Hennink, Hydrogels for Protein Delivery, Chem. Rev. 112 (2012) 2853–2888. https://doi.org/10.1021/cr200157d.

[195] B. Chatin, M. Mével, J. Devallière, L. Dallet, T. Haudebourg, P. Peuziat, T. Colombani, M. Berchel, O. Lambert, A. Edelman, B. Pitard, Liposome-based Formulation for Intracellular Delivery of Functional Proteins, Mol. Ther. - Nucleic Acids. 4 (2015). https://doi.org/10.1038/mtna.2015.17.

[196] M. Ray, Y.-W. Lee, F. Scaletti, R. Yu, V.M. Rotello, Intracellular delivery of proteins by nanocarriers, Nanomedicine (Lond). 12 (2017) 941–952. https://www.ncbi.nlm.nih.gov/pmc/articles/PMC5829369/.

[197] C. Le Roy, J.L. Wrana, Clathrin- and Non-Clathrin- Mediated Endocytic Regulation of Cell Signalling, Nat. Rev. Mol. Cell Biol. 6 (2005) 112–126. https://doi.org/10.2217/nnm-2016-0393.

[198] I.M. Verma, N. Somia, Gene therapy - promise, problems and prospects, Nature. 389 (1997) 239–242. https://doi.org/10.1038/38410.

[199] N. Kudo, K. Yamamoto, Sonoporation: Mechanisms of cell membrane perforation and rapid resealing, J. Acoust. Soc. Am. 120 (2006) 3229. https://doi.org/10.1121/1.4788218.

[200] R. Xiong, F. Joris, I. De Cock, J. Demeester, S.C. De Smedt, A.G. Skirtach, K. Braeckmans, Efficient delivery of quantum dots in live cells by gold nanoparticle mediated photoporation, Colloid. Nanoparticles Biomed. Appl. X. 9338 (2015) 93380X. https://doi.org/10.1117/12.2075659.

[201] J. Fraire, G. Houthaeve, J. Liu, L. Raes, S. Stremersch, T. Brans, G. García-Díaz Barriga, K. Raemdonck, W.H. De Vos, S. De Smedt, K. Braeckmans, VNB-mediated endosomal escape triggers robust gene silencing in human cell lines, Colloid. Nanoparticles Biomed. Appl. XV. 11255 (2020) 3. https://doi.org/10.1117/12.2542160.

[202] J.K. Armstrong, R.B. Wenby, H.J. Meiselman, T.C. Fisher, The hydrodynamic radii of macromolecules and their effect on red blood cell aggregation, Biophys. J. 87 (2004) 4259–4270. https://doi.org/10.1529/biophysj.104.047746.

[203] V. Zarnitsyn, C.A. Rostad, M.R. Prausnitz, Modeling Transmembrane Transport through Cell Membrane Wounds Created by Acoustic Cavitation, Biophys. J. 95 (2008) 4124–4138. https://doi.org/10.1529/biophysj.108.131664.

[204] M. Arrio-Dupont, S. Cribier, G. Foucault, P.F. Devaux, A. D’Albis, Diffusion of fluorescently labeled macromolecules in cultured muscle cells, Biophys. J. 70 (1996) 2327–2332. https://doi.org/10.1016/S0006-3495(96)79798-9.

[205] F. Galisteo-González, B.G. Monasterio, D. Gil, M. Valle, F.M. Goñi, Photoacoustic effect applied on model membranes and living cells: direct observation with multiphoton excitation microscopy and long-term viability analysis, Sci. Rep. 10 (2020) 1–9. https://doi.org/10.1038/s41598-019-56799-9.

[206] M.E. Young, P.A. Carroad, R.L. Bell, Estimation of diffusion coefficients of proteins, Biotechnol. Bioeng. 22 (1980) 947–955. https://doi.org/10.1002/bit.260220504.

[207] D.W. Pack, A.S. Hoffman, S. Pun, P.S. Stayton, Design and development of polymers for gene delivery, Nat. Rev. Drug Discov. 4 (2005) 581–593. https://doi.org/10.1038/nrd1775.

[208] A.R. Rastinehad, H. Anastos, E. Wajswol, J.S. Winoker, J.P. Sfakianos, S.K. Doppalapudi, M.R. Carrick, C.J. Knauer, B. Taouli, S.C. Lewis, A.K. Tewari, J.A. Schwartz, S.E. Canfield, A.K. George, J.L. West, N.J. Halas, Gold nanoshell-localized photothermal ablation of prostate tumors in a clinical pilot device study, Proc. Natl. Acad. Sci. U. S. A. 116 (2019) 18590–18596. https://doi.org/10.1073/pnas.1906929116.

[209] T. Li, L. Wu, J. Zhang, G. Xi, Y. Pang, X. Wang, T. Chen, Hydrothermal Reduction of Polyethylenimine and Polyethylene Glycol Dual-Functionalized Nanographene Oxide for High-Efficiency Gene Delivery, ACS Appl. Mater. Interfaces. 8 (2016) 31311–31320. https://doi.org/10.1021/acsami.6b09915.

[210] A.M. Kelly, S.A. Plautz, J. Zempleni, A.K. Pannier, Glucocorticoid cell priming enhances transfection outcomes in adult human mesenchymal stem cells, Mol. Ther. 24 (2016) 331–341. https://doi.org/10.1038/mt.2015.195.

[211] A. Hamann, K. Broad, A. Nguyen, A.K. Pannier, Mechanisms of unprimed and dexamethasone-primed nonviral gene delivery to human mesenchymal stem cells, Biotechnol. Bioeng. 116 (2019) 427–443. https://doi.org/10.1002/bit.26870.

[212] R.C. Lee, L.P. River, F.S. Pan, L. Ji, R.L. Wollmann, Surfactant-induced sealing of electropermeabilized skeletal muscle membranes in vivo, Proc. Natl. Acad. Sci. U. S. A. 89 (1992) 4524–4528. https://doi.org/10.1073/pnas.89.10.4524.

[213] A.S. Hannah, D. VanderLaan, Y.-S. Chen, S.Y. Emelianov, Photoacoustic and ultrasound imaging using dual contrast perfluorocarbon nanodroplets triggered by laser pulses at 1064 nm, Biomed. Opt. Express. 5 (2014) 3042. https://doi.org/10.1364/boe.5.003042.

[214] S.Y. Holguin, Physical Mechanisms of Laser-Activated Nanoparticles for Intracellular Drug Delivery, 2017.

[215] Y. Zhou, Application of acoustic droplet vaporization in ultrasound therapy, J. Ther. Ultrasound. 3 (2015) 1–18. https://doi.org/10.1186/s40349-015-0041-8.

[216] A. Grigonis, Z. Rutkuniene, V. Vinciunaite, Different wavelength laser irradiation of amorphous carbon, Acta Phys. Pol. A. 120 (2011) 26–29. https://doi.org/10.12693/APhysPolA.120.26.

[217] S. Prahl, Mie Scattering Calculator, Oregon Med. Laser Cent. (2018).

https://omlc.org/calc/mie_calc.html.

[218] I. Pastoriza-santos, D. Gomez, J. Perez-Juste, L.M. Liz-Marzan, P. Mulvaney, Optical properties of metal nanoparticle coated silica spheres: a simple Effective Medium Approach, Phys Chem Chem Phys. 6 (2004) 5056–5060.

[219] T. Ung, L.M. Liz-Marzán, P. Mulvaney, Optical properties of thin films of AuO/SiO2 particles, J. Phys. Chem. B. 105 (2001) 3441–3452. https://doi.org/10.1021/jp003500n.